

**FROM CARBON TO COPPER: STUDIES OF NOVEL NANOMATERIALS**

---

A Dissertation

Presented to

the Faculty of the Graduate School

University of Missouri-Columbia

---

In Partial Fulfillment

of the Requirements for the Degree

Doctor of Philosophy

---

by

KAREN A. KIRBY

Dr. Steven Keller and Dr. Jerry Atwood, Dissertation Supervisors

DECEMBER 2007

© Copyright by Karen A. Kirby 2007  
All Rights Reserved

The undersigned, appointed by the Dean of the Graduate School,  
have examined the dissertation entitled

**FROM CARBON TO COPPER: STUDIES OF NOVEL NANOMATERIALS**

presented by Karen A. Kirby

a candidate for the degree of Doctor of Philosophy

and hereby certify that in their opinion it is worthy of acceptance.

---

Professor Steven Keller

---

Professor Jerry Atwood

---

Professor Paul Duval

---

Professor Susan Lever

---

Professor Stephen Lombardo

## ACKNOWLEDGEMENTS

First and foremost, I would like to thank my advisors, Dr. Steven Keller and Dr. Jerry Atwood, for their continual support and guidance throughout my graduate career. I am also grateful to my committee members, Dr. Paul Duval, Dr. Susan Lever, and Dr. Stephen Lombardo, for their guidance and helpful discussions.

I must give many, many thanks to Dr. Charles Barnes, who spent countless time teaching me how to collect X-ray diffraction data and how to solve structures. Without his direction and great expertise, I would not have been able to complete much of this dissertation work.

I would also like to thank the MU Electron Microscopy Core, especially Randy Tindall and Lou Ross, for their help in learning TEM and SEM techniques and imaging.

Thanks to John Walters at Brookfield Engineering Laboratories, Inc. for taking viscosity measurements and for helpful discussion about viscosity. Special thanks to Dr. Stephen Lombardo for many helpful discussions about viscosity.

I am very thankful to present and past members of the Atwood and Keller groups for their support and friendship, especially Jackie Knaust, Brian Huesgen and Steven Bockhold. Special thanks to the undergraduate students in the Keller lab who did experiments to help me finish this work, specifically Lindsay Simpson, Amber Bolin, and Doug Haden.

Many thanks to Jackie Knaust and Lib Morgan for their support and friendship. I didn't realize how much I depended on those girls' nights out until they were gone.

Thanks to the Happy Hour gang: Steve Bockhold, Eric Weis, and Demetrius Taylor. Our weekly outings helped make the last year or so more bearable.

I can't thank Steve Bockhold enough for putting up with me for our entire graduate career, especially the last two years. Your insights and assistance were very valuable and much appreciated.

Thanks to Kathy for being patient with me and for supporting me throughout this entire process. Our friendship means so much to me.

To Harriet, thank you for being my main source of comfort over the past year and for putting up with my crazy hours. I don't know how I would have survived without you. You've brought so much joy to my life.

And last but certainly not least, thanks to my family, Mom, Dad, Jen, Maggie, and Molly for all your love and support. The words "thank you" cannot accurately express my gratitude for all you have done for me. I love you all.

## TABLE OF CONTENTS

|  |     |
|--|-----|
| Acknowledgements .....   | ii  |
| List of Figures .....  | vi  |
| List of Tables .....   | xii |
| List of Nomenclature .....   | xiv |
| Abstract .....   | xv  |
| Chapter  |     |
| 1. Introduction to Nanomaterials .....   | 1   |
| 1.1 Introduction .....   | 1   |
| 1.2 Applications .....   | 5   |
| 1.3 Goal of Research .....   | 6   |
| 1.4 References .....   | 6   |
| 2. Single-Walled Carbon Nanotube Gels and Foam .....   | 9   |
| 2.1 Introduction .....   | 9   |
| 2.2 Experimental .....   | 12  |
| 2.3 Results and Discussion .....   | 15  |
| 2.4 Conclusion .....   | 34  |
| 2.5 References .....   | 35  |
| 3. Effects of Anion and Solvent Choice on the Structures of Cu(I) Coordination Polymers..... | 39  |
| 3.1 Introduction .....   | 39  |
| 3.2 Experimental .....   | 41  |
| 3.3 Results and Discussion .....   | 51  |
| 3.4 Conclusion .....   | 71  |

|   |     |
|---|-----|
| 3.5 References .....  | 72  |
| 4. Novel Mixed Valent Copper(I)/Copper(II) and Copper(II) Coordination Polymers ..... | 74  |
| 4.1 Introduction .....  | 74  |
| 4.2 Experimental .....  | 70  |
| 4.3 Results and Discussion .....  | 82  |
| 4.4 Conclusion .....  | 109 |
| 4.5 References .....  | 110 |
| 5. Conclusion .....   | 112 |
| Vita .....  | 113 |

## LIST OF FIGURES

|   |    |
|---|----|
| <b>Figure 1.1.</b> Electronic band structures of metals, semiconductors, and insulators.....  | 2  |
| <b>Figure 1.2.</b> Schematic of the propagation of a slip plane across a grain boundary<br>in a crystal.....  | 4  |
| <b>Figure 2.1.</b> Three-dimensional representation of the end-on view of a section of a<br>SWCNT (a) vs. a section of a three-layer MWCNT (b).....   | 10 |
| <b>Figure 2.2.</b> Schematic of the sol-gel transition.....   | 16 |
| <b>Figure 2.3.</b> Observed swelling of SWCNT-benzene gels upon increased addition of<br>solvent. From left: 2, 4, 6, 8, and 10 mL SWCNT-benzene gels.....  | 17 |
| <b>Figure 2.4.</b> SEM micrographs of as-received SWCNTs (a) and a 1.0 wt % SWCNT-<br>benzene gel (b).....  | 18 |
| <b>Figure 2.5.</b> SEM micrographs of as-received SWCNTs (a) and a 1.0 wt %<br>SWCNT-benzene gel (b) both at 1.80k magnification.....   | 19 |
| <b>Figure 2.6.</b> FTIR spectra of SWCNTs before and after 1 hour of sonication.....  | 20 |
| <b>Figure 2.7.</b> Increased boiling point of benzene in 1.0 wt % SWCNT-benzene gel as<br>compared to the boiling point of pure benzene.....  | 22 |
| <b>Figure 2.8.</b> Breakdown of the different types of non-Newtonian fluids.....  | 24 |
| <b>Figure 2.9.</b> Graph of shear stress, $\tau$ , vs. shear rate, D, for Newtonian and time-<br>independent non-Newtonian fluids. The symbol $\tau_0$ represents the yield stress<br>of the Bingham plastic fluid..... | 25 |

|  |    |
|--|----|
| <b>Figure 2.10.</b> Shear stress as a function of shear rate for a 1.0 wt % SWCNT-benzene gel.....   | 26 |
| <b>Figure 2.11.</b> Viscosity as a function of shear rate for a 1.0 wt % SWCNT-benzene gel.....  | 27 |
| <b>Figure 2.12.</b> Calculated shear stress values using the Herschel-Bulkly model and measured shear stress as functions of shear rate for a 1.0 wt % SWCNT-benzene gel.....        | 29 |
| <b>Figure 2.13.</b> SEM micrograph taken at room temperature of a bulk piece of SWCNT foam.....  | 30 |
| <b>Figure 2.14.</b> Structures of <i>p</i> - <i>tert</i> -butylcalix[4]arene (a) and metal-organic framework (b).....  | 32 |
| <b>Figure 2.15.</b> Methane sorption isotherms of SWCNT foam, <i>p</i> - <i>tert</i> -butylcalix[4]arene, and MOF at room temperature (a) and at – 70 °C (b).....                    | 33 |
| <b>Figure 3.1.</b> Common ligands used by the Keller group to form Cu(I) coordination polymers.....  | 40 |
| <b>Figure 3.2.</b> Coordination environment of the unique Cu(I) center in <b>9</b> .....   | 51 |
| <b>Figure 3.3.</b> Comparison of the <i>trans</i> chains of the previously reported [Cu(phen)(MeCN) <sub>2</sub> ]PF <sub>6</sub> (a) and the <i>cis</i> chains of <b>9</b> (b)..... | 53 |
| <b>Figure 3.4.</b> Space-fill view of the π – π stacking between phens of neighboring chains in <b>9</b> .....   | 53 |
| <b>Figure 3.5.</b> Packing diagram of neighboring <i>cis</i> chains of <b>9</b> viewed down the <i>b</i> -axis.....  | 54 |
| <b>Figure 3.6.</b> TGA of <b>9</b> .....   | 56 |

|   |    |
|---|----|
| <b>Figure 3.7.</b> Powder X-ray diffraction pattern of the TGA residue of <b>9</b> .....  | 56 |
| <b>Figure 3.8.</b> Coordination environment of the unique Cu(I) center in <b>10</b> .....   | 57 |
| <b>Figure 3.9.</b> Chains formed in <b>10</b> .....   | 58 |
| <b>Figure 3.10.</b> Space-fill view of the $\pi - \pi$ stacking between neighboring phens in <b>10</b> .....  | 59 |
| <b>Figure 3.11.</b> Packing diagram of the chains in <b>10</b> viewed down the <i>a</i> -axis.....  | 59 |
| <b>Figure 3.12.</b> TGA of <b>10</b> .....  | 60 |
| <b>Figure 3.13.</b> Coordination environment of the two unique Cu(I) centers in <b>11</b> ...   | 61 |
| <b>Figure 3.14.</b> Chains formed in <b>11</b> .....  | 63 |
| <b>Figure 3.15.</b> Stick view of the disordered nitrobenzene in the phen cavity and nitrobenzenes outside the cavity (a) vs. space-fill view of the same picture showing the $\pi - \pi$ interactions between the nitrobenzenes and phens (b)... | 63 |
| <b>Figure 3.16.</b> Space-fill view of the $\pi - \pi$ stacking of phens on neighboring chains in <b>11</b> .....   | 64 |
| <b>Figure 3.17.</b> Packing diagram of the chains in <b>11</b> viewed down the <i>a</i> -axis.....  | 64 |
| <b>Figure 3.18.</b> TGA of <b>11</b> .....  | 65 |
| <b>Figure 3.19.</b> Coordination environment of the unique Cu(I) center in <b>12</b> .....  | 67 |
| <b>Figure 3.20.</b> Chains formed in <b>12</b> .....  | 68 |

|   |    |
|---|----|
| <b>Figure 3.21.</b> Space-fill view of the $\pi - \pi$ stacking between the nitrobenzenes and phens in <b>12</b> .....  | 68 |
| <b>Figure 3.22.</b> Packing diagram of the chains in <b>12</b> viewed down the <i>b</i> -axis.....  | 69 |
| <b>Figure 3.23.</b> TGA of <b>12</b> .....  | 70 |
| <b>Figure 4.1.</b> Doug's mixed valent complex,<br>[Cu <sub>9</sub> (pyrimidine) <sub>10</sub> (MeCN) <sub>12</sub> (OH)](BF <sub>4</sub> ) <sub>9</sub> . The Cu(I) centers that make<br>up the squares are connected by two Cu(II) centers..... | 75 |
| <b>Figure 4.2.</b> Structure of [Cu <sub>4</sub> (pyrimidine) <sub>4</sub> (MeCN) <sub>8</sub> ](BF <sub>4</sub> ) <sub>4</sub> .....   | 82 |
| <b>Figure 4.3.</b> Observed color changes in the [Cu(MeCN) <sub>4</sub> ]BF <sub>4</sub> –pyrimidine solution<br>upon increased addition of O <sub>2</sub> .....  | 83 |
| <b>Figure 4.4.</b> UV-Vis spectra of solutions of [Cu(MeCN) <sub>4</sub> ]BF <sub>4</sub> –pyrimidine with<br>increasing amounts of oxygen added to different solutions.....  | 84 |
| <b>Figure 4.5.</b> TGA of <b>13</b> .....   | 85 |
| <b>Figure 4.6.</b> Coordination environment of the three unique Cu(II) centers in <b>14</b> ....  | 87 |
| <b>Figure 4.7.</b> Ladders formed in <b>14</b> .....  | 89 |
| <b>Figure 4.8.</b> Unique hydrogen bonds in <b>14</b> .....   | 89 |
| <b>Figure 4.9.</b> Hydrogen-bonded network in <b>14</b> .....   | 91 |
| <b>Figure 4.10.</b> Alternate view of the hydrogen-bonded network in <b>14</b> .....  | 91 |
| <b>Figure 4.11.</b> Packing diagram of the ladders in <b>14</b> viewed down the <i>b</i> -axis.....   | 92 |

|  |     |
|--|-----|
| <b>Figure 4.12.</b> TGA of <b>14</b> .....   | 93  |
| <b>Figure 4.13.</b> Coordination environment of the three unique Cu(I) centers in <b>15</b> .....  | 94  |
| <b>Figure 4.14.</b> Rectangular cage formed by the bridging pyrimidines in <b>15</b> . A $\text{PF}_6^-$ anion (in spacefill) resides in the middle of the cage.....   | 96  |
| <b>Figure 4.15.</b> Alternate view of <b>15</b> down the body diagonal of the cube.....  | 96  |
| <b>Figure 4.16.</b> Doug's Cu(I)-pyrimidine cage containing an enclosed perchlorate anion (spacefill).....   | 97  |
| <b>Figure 4.17.</b> Packing diagram of <b>15</b> within the unit cell viewed down the (111) plane.....   | 98  |
| <b>Figure 4.18.</b> Packing diagram of previously reported $[\text{Cu}_{1.3}(\text{pyrimidine})_{2.5}(\text{OH})_{0.167}(\text{H}_2\text{O})_{0.167}](\text{PF}_6)_{1.167}$ within the unit cell viewed down the <i>c</i> -axis. Anions and disordered solvent molecules are included..... | 99  |
| <b>Figure 4.19.</b> TGA of <b>15</b> .....   | 100 |
| <b>Figure 4.20.</b> Coordination environment around the unique Cu(II) center in <b>16</b> .....  | 101 |
| <b>Figure 4.21.</b> Diagram of the Jahn-Teller distortion that occurs in <b>16</b> .....   | 102 |
| <b>Figure 4.22.</b> Ribbons formed by bridging pyrimidines in <b>16</b> .....  | 103 |
| <b>Figure 4.23.</b> Hydrogen-bonded network connecting the ribbons in <b>16</b> .....  | 104 |
| <b>Figure 4.24.</b> Alternate view of the hydrogen-bonded network in <b>16</b> .....   | 104 |
| <b>Figure 4.25.</b> Packing diagram of <b>16</b> within the unit cell viewed down the <i>a</i> -axis....   | 105 |

**Figure 4.26.** TGA of **16**..... 107

## LIST OF TABLES

|  |     |
|--|-----|
| <b>Table 2.1.</b> Amounts of SWCNTs necessary to form 0.5 wt % and 1.0 wt % gels in 2 mL of selected solvents..... | 14  |
| <b>Table 2.2.</b> DSC data for samples of benzene, 0.5 wt % SWCNT-benzene gel, and 1.0 wt % SWCNT-benzene gel..... | 22  |
| <b>Table 3.1.</b> Selected crystallographic details for <b>9 – 12</b> .....  | 50  |
| <b>Table 3.2.</b> Selected bond lengths and angles in <b>9</b> .....   | 52  |
| <b>Table 3.3.</b> Selected bond lengths and angles in <b>10</b> .....  | 58  |
| <b>Table 3.4.</b> Selected bond lengths and angles in <b>11</b> .....  | 62  |
| <b>Table 3.5.</b> Selected bond lengths and angles in <b>12</b> (from <b>8</b> ).....                              | 67  |
| <b>Table 4.1.</b> Selected crystallographic details for <b>14 – 16</b> .....                                       | 81  |
| <b>Table 4.2.</b> Selected bond lengths and angles in <b>14</b> .....  | 88  |
| <b>Table 4.3.</b> Hydrogen bond distances in <b>14</b> .....   | 90  |
| <b>Table 4.4.</b> Selected bond lengths and angles in <b>15</b> .....  | 95  |
| <b>Table 4.5.</b> Selected bond lengths and angles in <b>16</b> .....  | 101 |
| <b>Table 4.6.</b> Hydrogen bond distances in <b>16</b> .....   | 106 |

|  |     |
|--|-----|
| <b>Table 4.7.</b> Summary of the conditions required for the oxidation of Cu(I) in the presence of pyrimidine, bipy, and phen..... | 108 |
|--|-----|

## LIST OF NOMENCLATURE

SWCNT = Single-Walled Carbon Nanotube

MWCNT = Multi-Walled Carbon Nanotube

ODCB = *ortho*-Dichlorobenzene

SEM = Scanning Electron Microscopy

FTIR = Fourier-Transform Infrared Spectroscopy

DSC = Differential Scanning Calorimetry

PXRD = Powder X-ray Diffraction

TGA = Thermal Gravimetric Analysis

MOF = Metal-Organic Framework

MeCN = Acetonitrile

PhCN = Benzonitrile

THF = Tetrahydrofuran

Et<sub>2</sub>O = Diethyl Ether

PhNO<sub>2</sub> = Nitrobenzene

PPh<sub>3</sub> = Triphenylphosphine

Phen = 4,7-Phenanthroline

Bipy = 4,4'-Bipyridine

ASU = Asymmetric Unit

# FROM CARBON TO COPPER: STUDIES OF NOVEL NANOMATERIALS

Karen A. Kirby

Dr. Steven Keller and Dr. Jerry Atwood, Dissertation Supervisors

## ABSTRACT

Nanomaterials are materials on the order of  $10^{-9}$  m that are currently being investigated for use in a wide range of applications in the growing field of nanotechnology. This dissertation documents the synthesis, characterization, and applications of two particular types of nanomaterials: single-walled carbon nanotubes and copper-based coordination polymers. The synthesis of single-walled carbon nanotube gels and foam is detailed, and a series of techniques including scanning electron microscopy, infrared spectroscopy, differential scanning calorimetry, and viscometry were employed to learn more about the properties of the gels and foam. Methane sorption studies were performed using the gel, and there is a potential use for the foam in composite materials as well. Single crystal X-ray diffraction was used to determine the structures of various Cu(I) and Cu(II) coordination polymers. The thermal stability of the coordination polymers was studied by thermal gravimetric analysis. The seven different structures reported are compared, and their potential applications are also discussed.

# **Chapter 1**

## **Introduction to Nanomaterials**

### **1.1 Introduction**

Research in the field of nanotechnology has garnered much attention within the past 10 years. President Bill Clinton was the first U.S. President to advocate nanotechnology, but it was President George W. Bush who in 2003 signed the 21<sup>st</sup> Century Nanotechnology Research and Development Act. This law authorized a budget of over \$3.63 billion over four years for the study of nanotechnology. This act has helped ensure that the U.S. will be on the cutting edge of nanotechnology research over the next few years.<sup>1,2</sup>

The materials being studied with applications in nanotechnology are often referred to as nanomaterials. When most people think of nano-, they think “small.” In fact, the prefix nano- refers to objects that are on the order of  $10^{-9}$  m in size, although nanomaterials are typically defined as particles, whether they are crystals, rods, or spheres that are between 1 and 100 nm in size (usually defined by diameter). Why the big push in the scientific community toward nanotechnology in recent years? There are several reasons, but the primary motivation is because nanomaterials typically exhibit different electronic, optical, and mechanical properties than their bulk material and even

molecular complements. Examples of these phenomena will be discussed in the following paragraphs.

The changing of a material's electronic properties as it decreases in size is referred to the quantum size effect. The quantum size effect in metallic nanoparticles is well documented in the literature. In bulk metals, the valence and conduction bands overlap, while in metal nanoparticles there is a gap between these bands. The gap observed in metal nanoparticles can be similar in size to that seen in semiconductors ( $< 2$  eV) or even insulators ( $> 2$  eV).<sup>3</sup> A diagram of the electronic bands in bulk metals, semiconductors, and insulator can be seen in Figure 1.

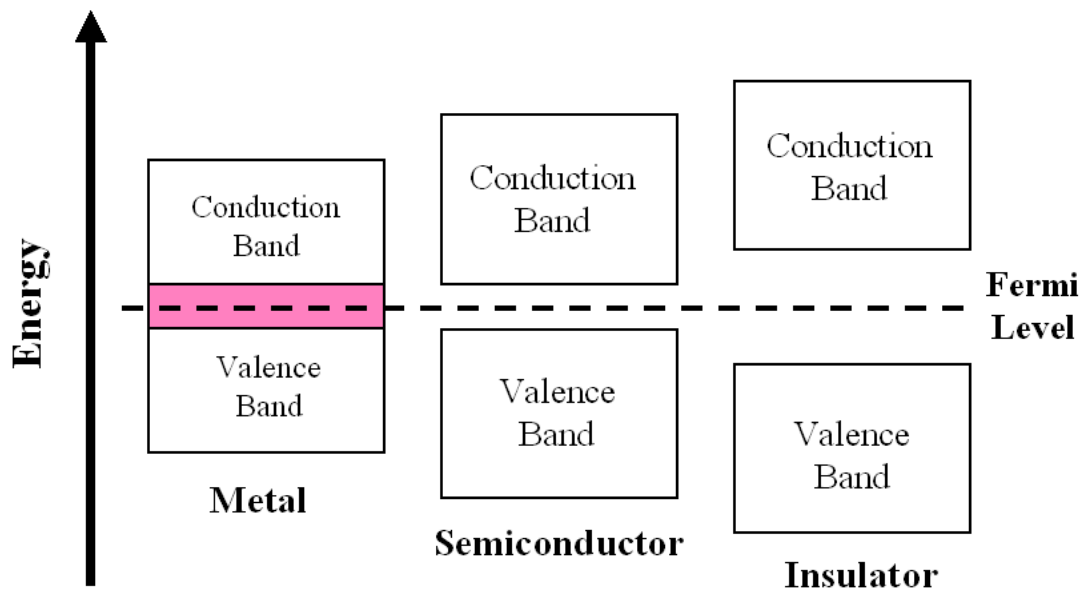


**Figure 1.** Electronic band structures of metals, semiconductors, and insulators.

The pink region represents the overlap of the valence and conduction bands in the metal. Metal nanoparticles typically exhibit band structures similar to semiconductors or insulators rather than bulk metals.

## Chapter 1

Electronic conduction occurs when one or more electrons are excited from the filled valence band into the empty conduction band.

The quantum size effect also results in an observable blue shift (smaller wavelength, higher energy) in the optical band gap or excitation energy of nanoparticles. For example, CdS particles 50-60 Å in size appear white as opposed to orange bulk CdS and PbS particles around 180 Å in size appear yellow-brown as opposed to black bulk PbS.<sup>4,5</sup> Experiments have shown that the band gap increases as the particle size decreases and approaches the transition energy of the first allowed excited state of the PbS molecule.

The tailoring of materials on the near-atomic level has proven to be a valuable tool in the obtainment of desired properties of bulk materials. For instance, small changes at the atomic level in bulk metals are known to change mechanical properties, and in particular such changes are often performed to strengthen materials. In single-phase metals, strengthening can be achieved by grain size reduction and solid-solution strengthening or alloying. Grain size reduction works to strengthen materials by making it difficult for defects in crystals such as slip planes or dislocations to continue propagation, because the slip plane or dislocation will have to change direction once crossing the grain boundary, as shown in Figure 2. This becomes more difficult if the crystal increases in misorientation. The presence of smaller grains results in a large grain boundary area to hinder dislocation motion.

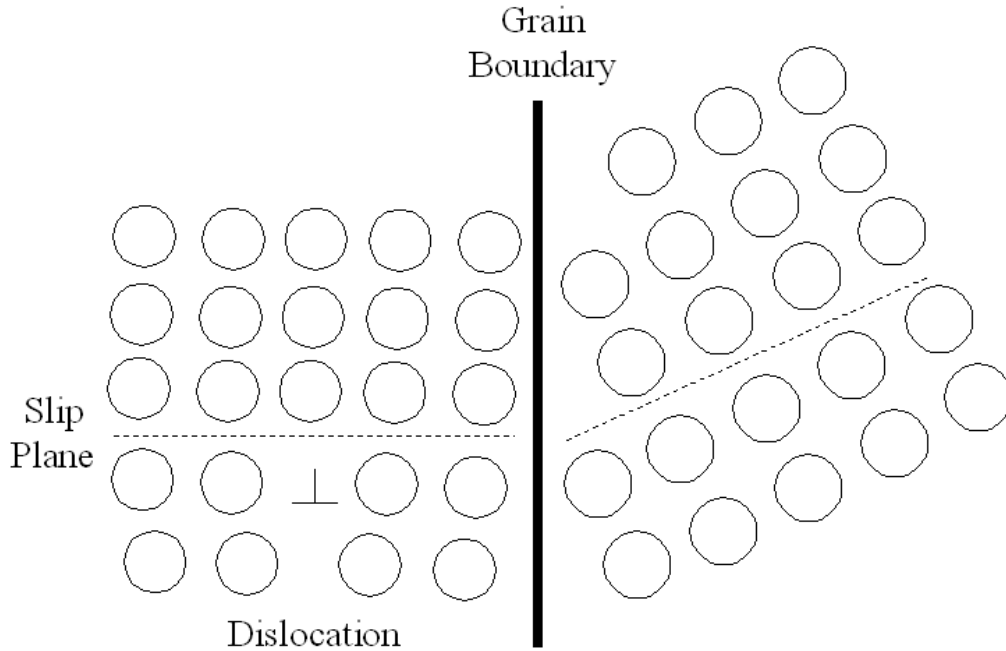


**Figure 2.** Schematic of the propagation of a slip plane across a grain boundary in a crystal.

Solid-solution strengthening involves adding impurity atoms to either substitutional or interstitial sites in a solid solution. This technique is also known as alloying. Alloys are stronger than pure metals because the impurities impose lattice strains on the surrounding host atoms. These lattice strains restrict dislocation propagation. Increasing the concentration of impurity atoms results in an increase in the tensile and yield strengths of the solid solution. Examples of alloys include rose gold (gold-copper alloys), brass (copper-zinc alloys), bronze (copper-tin alloys), steel (iron-carbon alloys), stainless steel (iron-chromium-nickel alloys), and pewter (tin-copper alloys).<sup>6</sup>

## 1.2 Applications

It is likely that these small materials will be at the forefront of some of the most influential technological breakthroughs of the century. For instance, in today's computing and information society, the demand for increased storage or disk space on increasingly smaller machines is growing. Researchers are already making progress in the field of molecular computers, computers built at the cellular level with atomic precision, complete with nanocircuitry.<sup>7-10</sup>

Another common use for nanoparticles is in the area of catalysis. Small particles have a large surface area to react with and are therefore ideal for many catalytic reactions. Some of these reactions include the synthesis of ammonia, photocatalysis, waste removal, and environmental protection (such as the absorption of toxic materials).<sup>1</sup>

Nanomaterials are also being investigated for many uses in biological and medical applications, such as drug delivery. Microchip sensors to monitor drug release and new prosthetics are two of many exciting applications to come in the medical field.<sup>11-13</sup>

Perhaps the hottest topic in the scientific community that has gained much public interest in the past 5 years is the search for alternative fuels. Hydrogen is one of the front-runners in alternative fuels, especially because it is readily available and environmentally friendly. The biggest obstacle to overcome is the storage of hydrogen gas in cars, as it is highly combustible and dangerous. Countless efforts are underway to find an economical, safe way to store hydrogen. Most of the current best options for storing hydrogen include carbon nanotubes<sup>14-17</sup> and metal-organic frameworks.<sup>18-21</sup>

### 1.3 Goal of Research

The goal of my graduate research has centered around the synthesis of novel nanomaterials, and I have focused my research specifically on materials derived from carbon nanotubes and copper-based coordination polymers. The synthesis, characterization, and potential applications of these materials are discussed in the following chapters.

### 1.4 References

1. Gai, P. L.; Roper, R.; White, M. G., Recent Advances in Nanocatalysis Research. *Current Opinion in Solid State and Materials Science* **2002**, 6, 401-406.
2. www.nano.gov.
3. Daniel, M. C.; Astruc, D., Gold nanoparticles: Assembly, supramolecular chemistry, quantum-size-related properties, and applications toward biology, catalysis, and nanotechnology. *Chem. Rev.* **2004**, 104, (1), 293-346.
4. Wang, Y.; Herron, N., Quantum Size Effects on the Exciton Energy of Cds Clusters. *Phys. Rev. B* **1990**, 42, (11), 7253-7255.
5. Wang, Y.; Suna, A.; Mahler, W.; Kasowski, R., PbS in polymers. From molecules to bulk solids. *J. Chem. Phys.* **1987**, 87, (12), 7315-7322.
6. Callister, W. D., *Materials science and engineering : an introduction*. 5th ed.; Wiley: New York, 2000; 871 p.
7. Kulic, I. M., Evaluating polynomials on the molecular level - a novel approach to molecular computers. *Biosystems* **1998**, 45, (1), 45-57.

## Chapter 1

8. Ji, S., The cell as the smallest DNA-based molecular computer. *Biosystems* **1999**, 52, (1-3), 123-133.
9. Fahy, G. M., Molecular Nanotechnology. *Clinical Chemistry* **1993**, 39, (9), 2011-2016.
10. Joachim, C., Bonding more atoms together for a single molecule computer. *Nanotechnology* **2002**, 13, (2), R1-R7.
11. Rao, C. N. R.; Cheetham, A. K., Science and technology of nanomaterials: current status and future prospects. *J. Mat. Chem.* **2001**, 11, (12), 2887-2894.
12. Santini, J. T.; Cima, M. J.; Langer, R., A controlled-release microchip. *Nature* **1999**, 397, (6717), 335-338.
13. Quake, S. R.; Scherer, A., From micro- to nanofabrication with soft materials. *Science* **2000**, 290, (5496), 1536-1540.
14. Dillon, A. C.; Jones, K. M.; Bekkedahl, T. A.; Kiang, C. H.; Bethune, D. S.; Heben, M. J., Storage of hydrogen in single-walled carbon nanotubes. *Nature* **1997**, 386, (6623), 377-379.
15. Liu, C.; Fan, Y. Y.; Liu, M.; Cong, H. T.; Cheng, H. M.; Dresselhaus, M. S., Hydrogen storage in single-walled carbon nanotubes at room temperature. *Science* **1999**, 286, (5442), 1127-1129.
16. Lee, S. M.; Lee, Y. H., Hydrogen storage in single-walled carbon nanotubes. *App. Phys. Lett.* **2000**, 76, (20), 2877-2879.
17. Ye, Y.; Ahn, C. C.; Witham, C.; Fultz, B.; Liu, J.; Rinzler, A. G.; Colbert, D.; Smith, K. A.; Smalley, R. E., Hydrogen adsorption and cohesive energy of single-walled carbon nanotubes. *App. Phys. Lett.* **1999**, 74, (16), 2307-2309.
18. Rosi, N. L.; Eckert, J.; Eddaoudi, M.; Vodak, D. T.; Kim, J.; O'Keeffe, M.; Yaghi, O. M., Hydrogen storage in microporous metal-organic frameworks. *Science* **2003**, 300, (5622), 1127-1129.

## Chapter 1

19. Li, H.; Eddaoudi, M.; O'Keeffe, M.; Yaghi, O. M., Design and synthesis of an exceptionally stable and highly porous metal-organic framework. *Nature* **1999**, 402, (6759), 276-279.
20. Rowsell, J. L. C.; Yaghi, O. M., Strategies for hydrogen storage in metal-organic frameworks. *Angew. Chem. Inter. Ed.* **2005**, 44, (30), 4670-4679.
21. Pan, L.; Sander, M. B.; Huang, X. Y.; Li, J.; Smith, M.; Bittner, E.; Bockrath, B.; Johnson, J. K., Microporous metal organic materials: Promising candidates as sorbents for hydrogen storage. *J. Am. Chem. Soc.* **2004**, 126, (5), 1308-1309.

## **Chapter 2**

# **Synthesis and Characterization of Single-Walled Carbon Nanotube Gels and Foam**

## **2.1 Introduction**

Carbon nanotubes were discovered by Iijima in 1991 and immediately much interest was generated in the scientific community toward the exploration of the unique properties of this new graphite-based material.<sup>1</sup> Iijima actually observed multi-walled carbon nanotubes (MWCNT) in 1991, but it wasn't until 1993 that his group and also Bethune and coworkers at IBM discovered single-walled carbon nanotubes (SWCNT).<sup>2,3</sup> The observation of SWCNTs has proven to be essential to the study of the properties of carbon nanotubes because of their primary structure compared to that of the many-layered MWCNTs, as seen in Figure 2.1.

Single-walled carbon nanotubes can vary both in diameter and length. The nanotubes used in these studies are approximately 10 – 14 Å in diameter and roughly 300 nm in length.<sup>4</sup> Single-walled carbon nanotubes are one of the stiffest, strongest, and toughest fibers known, with a measured tensile strength of 0.3 – 1.4 TPa, a value which is approximately five times greater than the tensile strength of steel.<sup>5</sup> Not only do they have extraordinary mechanical properties, but SWCNTs have remarkable electronic properties

as well. The electronic properties arise from the  $sp^2$  hybridization of the carbon atoms in the SWCNT structure, leaving an unhybridized  $p$ -orbital containing one electron on each carbon, and it is the delocalization of this electron that allows for electronic conductivity throughout the nanotube.

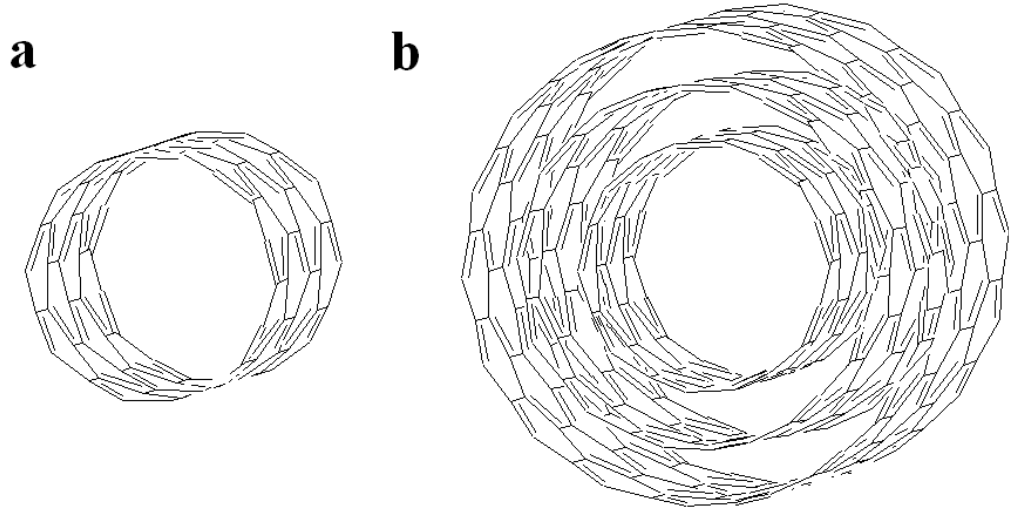


**Figure 2.1.** Three-dimensional representation of the end-on view of a section of a SWCNT (a) vs. a section of a three-layer MWCNT (b).

There are many potential uses for SWCNTs, ranging from space flight applications<sup>6-8</sup> to hydrogen storage.<sup>9-13</sup> While these applications are very exciting, there is one major problem standing in the way for most of them. Currently there is no known way to separate the highly entangled SWCNT bundles into individual tubes, which is necessary for the realization of many of their potential applications.

Because SWCNTs do not dissolve readily in any common organic solvents, much research has focused on methods to achieve solvation of carbon nanotubes in common organic solvents. Many of these methods involve irreversible chemical modification of

## Chapter 2

the carbon nanotube surface via covalent bonds,<sup>6-8</sup> while other methods make use of the noncovalent functionalization of molecules onto the nanotube surface.<sup>9-11</sup>

Many dispersions of SWCNTs in organic solvents have been well-documented in the literature.<sup>14-17</sup> In fact, Aida and co-workers published a report in 2003 of a SWCNT gel made by grinding the nanotubes with ionic liquids, claiming that the gelation was a result of the cation – π interactions between the ions and the SWCNTs.<sup>18</sup> We also tried using ionic liquids to make gels, but found the ionic liquids to be difficult to manipulate because of their high viscosity. We were not able to form SWCNT gels with the ionic liquids via sonication. Because of this we focused our efforts on using ionic solutions, (specifically tetrabutylammonium bromide in benzene) with which we were able to form gels with SWCNTs after sonication. After allowing these SWCNT-ionic solution gels to sit on the benchtop untouched for several weeks, we observed shrinking of the gel due to solvent evaporation. This result caused us to believe that the benzene, not the tetrabutylammonium and bromide ions, was causing the gelation phenomenon. Our theory was confirmed when we successfully formed a SWCNT-benzene gel after sonication in the pure solvent. The characterization and properties of these SWCNT-solvent gels and their use as a precursor to SWCNT foam and its potential applications are herein described.

## 2.2 Experimental

### *Materials and Methods*

Purified HiPco® single-walled carbon nanotubes (<15 wt % ash content, Carbon Nanotechnologies, Inc.), CarboLex AP-grade single-walled carbon nanotubes (50 – 70 vol % purity, Aldrich), activated carbon (Fisher), fullerenes (Acros), tetrabutylammonium bromide (Aldrich), benzene (EMD Chemicals), acetone, acetonitrile, cyclohexane, diethyl ether, methanol, methylene chloride, tetrahydrofuran (THF), toluene (Fisher), decane, *o*-dichlorobenzene (ODCB), hexane, nitrobenzene (NB), octane, and *p*-xylene (Aldrich) were used as received. All gel samples were sonicated in a Fisher Scientific FS30 sonicator (100 W, 120 V).

Scanning electron microscopy (SEM) was performed using a Hitachi S-4700 field emission scanning electron microscope (FESEM) at the MU Electron Microscopy Core with the help of Lou Ross and Randy Tindall. The electron beam was set at 5.0 kV and the In Lens Secondary Electron Detector was used to collect the images. All samples were uncoated. A small sample of 1.0 wt % SWCNT-benzene gel was plunge-frozen in liquid nitrogen and transferred under vacuum to a liquid nitrogen-cooled stage in the FESEM. The temperature of the stage was increased to -80 °C and the benzene was removed by sublimation under vacuum, followed by imaging of the sample under cryo conditions.

Fourier-transform infrared spectroscopy (FTIR) was performed using a ThermoNicolet 670 FTIR ESP spectrometer. For each sample, 1000 scans at a resolution of 1 cm<sup>-1</sup> were collected with the gain set to automatic, the velocity at 0.1581 cm/s, and the aperture at 69. An air sample was used for the background. Samples analyzed

## Chapter 2

include as-received SWCNTs, dried SWCNT-benzene gels, dried SWCNT-octane gels, dried SWCNT-decane gels, dried SWCNT-ODCB gels, and dried SWCNT-NB gels. The dried gel samples were prepared by sonication of 20 mg SWCNT in 2 mL solvent for 1 hour. The gels were then dried under medium heat in a vacuum oven for 1 hour, after which all solvents had been removed. Each of the dried samples was ground with 1 g dried KBr using a mortar and pestle, and then pellets were made of each sample using a hydraulic press.

Differential scanning calorimetry (DSC) was performed using a TA Instruments DSC Q100. Aluminum hermetic sample pans and pinhole lids were washed with deionized water, then xylenes, and allowed to dry before use to clean the pans and remove any oxide layers present. Sample sizes for solvents were one drop using a pipet (2 – 5 mg) and for gels a small amount of the sample was removed with a spatula for DSC analysis (10 – 20 mg). Each sample pan and pinhole lid were cold-welded together to prevent sample leakage. Samples of benzene, 0.5 wt %, and 1.0 wt % SWCNT-benzene gels were heated at a rate of 10 °C/min.

Viscosity measurements of 1.0 wt % SWCNT-benzene gels were performed by Brookfield Engineering Laboratories, Inc. on a R/S CPS+ Rheometer using plate / plate geometry with a 50 mm flat plate (P50) and the gap between the plates set at 0.5 mm. Data was taken under controlled stress conditions at room temperature, with the instrument ramping from 0 to 300 Pa in 60 seconds.

*Synthesis*

The general synthesis of the carbon nanotube gels consists of adding ~20 mg of SWCNTs to 2 mL of solvent or ionic solution, then sonicating the mixture for 1 hour. Solvents tested include water, methanol, acetone, methylene chloride, THF, acetonitrile, diethyl ether, carbon tetrachloride, cyclohexane, hexane, octane, decane, benzene, toluene, *p*-xylene, *o*-dichlorobenzene, and nitrobenzene, while 0.31 M tetrabutylammonium bromide in benzene was the only ionic solution tested. Table 2.1 lists the amounts of SWCNTs added to 2 mL of selected solvents to form 0.5 wt % and 1.0 wt % gels.

| <b>Solvent (2 mL)</b>     | <b>Amount SWCNTs<br/>added to form<br/>0.5 wt% gel (mg)</b> | <b>Amount SWCNTs<br/>added to form<br/>1.0 wt% gel (mg)</b> |
|---------------------------|---|---|
| Benzene                   | 8.8   | 17.8  |
| <i>o</i> -Dichlorobenzene | 13.1  | 26.4  |
| Nitrobenzene              | 12.0  | 24.2  |
| Octane                    | 7.1   | 14.2  |
| Decane                    | 7.3   | 14.7  |

**Table 2.1.** Amounts of SWCNTs necessary to form 0.5 wt % and 1.0 wt % gels in 2 mL of selected solvents.

Additional amounts of solvent may be added to the 2 mL gel, and with 3 – 8 more hours of sonication, depending on the amount of solvent added. Experiments have shown that up to 8 mL of hexane, octane, toluene, or *p*-xylene, and 10 mL (~ 0.2 wt %) of benzene,

*o*-dichlorobenzene, nitrobenzene, or tetrabutylammonium bromide solution can be used to form gels. Experiments have also shown that up to 4 mL of acetone can be used to form gels, although this requires 6 – 10 hours of sonication.

The SWCNT foam was synthesized by freeze-drying a bulk sample of 1.0 wt % SWCNT-benzene gel. This was done by freezing 10 mL of 1.0 wt % SWCNT-benzene gel in liquid nitrogen and then removing the benzene via sublimation under vacuum while the sample remained frozen.

## 2.3 Results and Discussion

We first discovered the gelation phenomenon after sonication of SWCNTs in a solution of tetrabutylammonium bromide in benzene. To determine if the ions were necessary for gelation, SWCNTs were sonicated in benzene for 1 hour. To our surprise, the SWCNTs did form a gel with the benzene. Because of this interesting observation, we stopped testing ionic solutions in favor of testing various solvents to form gels. We found that sonication of SWCNTs in the polar solvents water, methanol, methylene chloride, THF, and diethyl ether did not result in gelation, although acetonitrile and acetone did result in gels. Acetonitrile formed gels more rapidly than acetone, as the acetone required prolonged sonication to form gels with the nanotubes. On the other hand, we found that nonpolar solvents and aromatic solvents were very successful in forming SWCNT gels. It is not surprising that these two types of solvents interact well with the SWCNTs. It is likely that nonpolar solvents are able to easily interact with the nonpolar SWCNTs since nonpolar solutes tend to interact with nonpolar solvents, while the aromatic solvents likely form strong  $\pi - \pi$  interactions with the aromatic SWCNTs.

## Chapter 2

Other allotropes of carbon were also investigated to try to form gels. Activated carbon and fullerenes sonicated in aromatic solvents did not result in gelation. This observation tells us that the gelation phenomenon is unique to carbon nanotubes. Less pure SWCNTs (50 – 70 vol % purity) were also investigated and did result in forming gels in the aromatic solvents and even in acetone, which means the level of purity (amount of ash, graphite, or residual metal catalyst particles remaining from SWCNT synthesis) of the SWCNTs does not affect gel formation.

I believe that the gel formation of the SWCNTs is the result of the entangled nanotubes, which is due to their high aspect ratio. The gel forms because there are enough nanotube junctions, or places where the nanotubes are interacting with each other either chemically or physically, that the connected network spans the entire sample. The more junctions that are present between SWCNTs, the more likely the network is to form a gel because of increased solute-solute interactions compared to solute-solvent interactions. When there are fewer junctions present, then there are more solute-solvent interactions present in the mixture, and this phase is typically referred to as a sol.<sup>19</sup> This sol-gel transition is depicted in Figure 2.2.

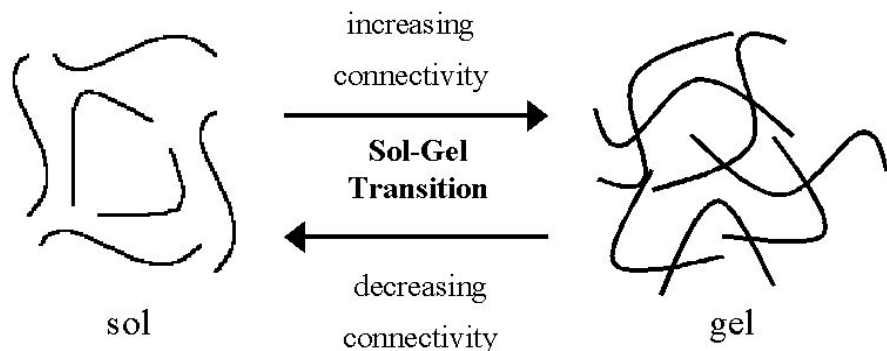


**Figure 2.2.** Schematic of the sol-gel transition.

## Chapter 2

The thick black gels formed by the SWCNTs are stable enough that upon inversion of the test tube they maintain their shape, yet the gels do flow with agitation. Addition of excess solvent causes the gels to swell to the volume of solvent added. Figure 2.3 shows the observed swelling of the gels when 20 mg of SWCNTs are sonicated in 2, 4, 6, 8, and 10 mL of benzene, respectively. These gels correspond to 1.1, 0.6, 0.4, 0.3, and 0.2 wt %, respectively.



**Figure 2.3.** Observed swelling of SWCNT-benzene gels upon increased addition of solvent. From left: 2, 4, 6, 8, and 10 mL SWCNT-benzene gels.

The structure of the SWCNT gels was studied by SEM under cryogenic conditions so that the structure of the gel would be maintained. Figure 2.4 shows an SEM micrograph of as-received SWCNTs under room temperature conditions compared to an SEM micrograph of a 1.0 wt % SWCNT-benzene gel under cryogenic conditions.

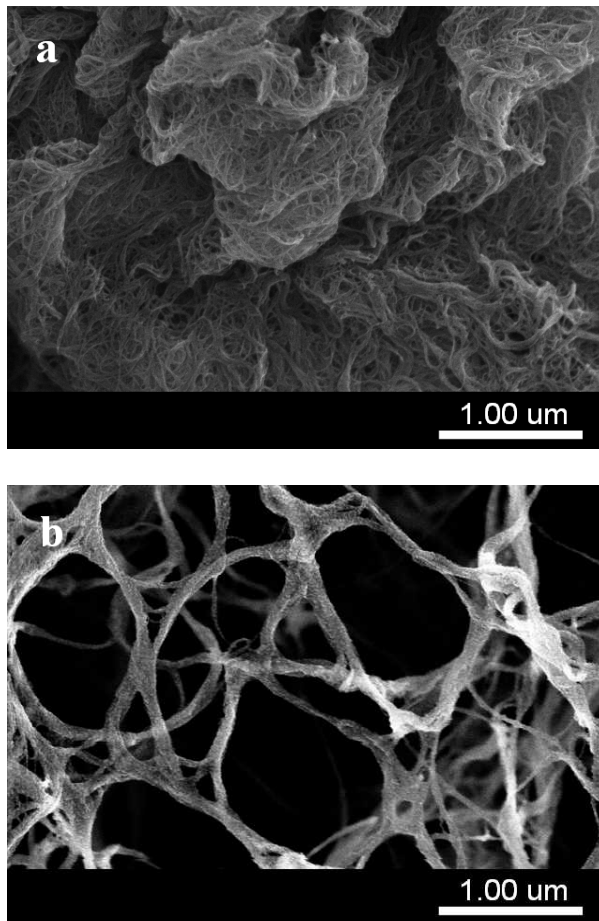


**Figure 2.4.** SEM micrographs of as-received SWCNTs (a) and a 1.0 wt % SWCNT-benzene gel (b) both at 30.0k magnification.

The SWCNT bundles in the as-received micrograph are very tightly tangled together, while the nanotubes in the gel micrograph, although still bundled, are much less entangled, showing large pores in the gel structure. Each bundle in Figure 2.4b measures roughly 150 nm in diameter, and with one SWCNT having a diameter of 10 – 15 Å, that means that each bundle shown contains anywhere from 100 to 150 individual nanotubes.

The large pores are not just visible in small regions of the gel sample, but can be observed throughout the entire structure, as shown in Figure 2.5.

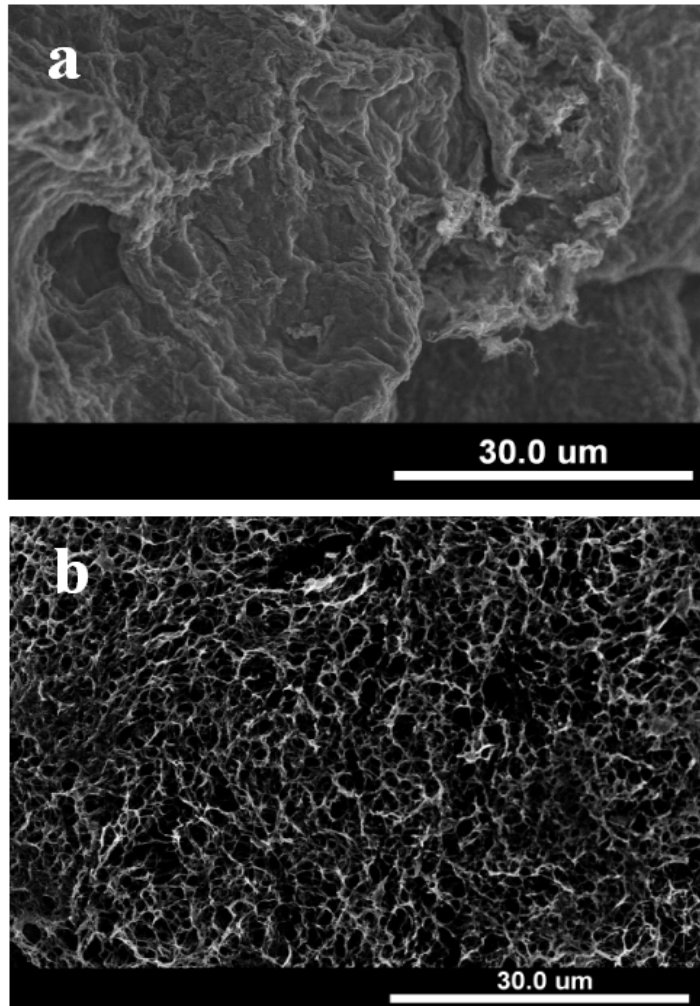


**Figure 2.5.** SEM micrographs of as-received SWCNTs (a) and a 1.0 wt % SWCNT-benzene gel (b) both at 1.80k magnification.

Some researchers have reported that sonication can damage SWCNTs, although their reports involve prolonged sonication of the nanotubes or other additives in the nanotube solution such as acids or polymers.<sup>20, 21</sup> FTIR was performed on our samples to

## Chapter 2

see if any chemical difference of the SWCNTs after 1 hour of sonication could be detected. The thought was that if chemical differences are detected, specifically the presence of strong carbonyl peaks at  $1710\text{ cm}^{-1}$  from carboxylic acid groups on the nanotube surface, then this would serve as an indication that the formation of the gels is due to chemical linkage of these functional groups on the SWCNTs. If no chemical differences are detected, then this would serve as an indication that the formation of the gels is due to the physical interactions between the nanotubes. Figure 2.6 shows the FTIR data collected for as-received SWCNTs, dried SWCNT-benzene gels, dried SWCNT-octane gels, dried SWCNT-decane gels, dried SWCNT-ODCB gels, and dried SWCNT-NB gels.

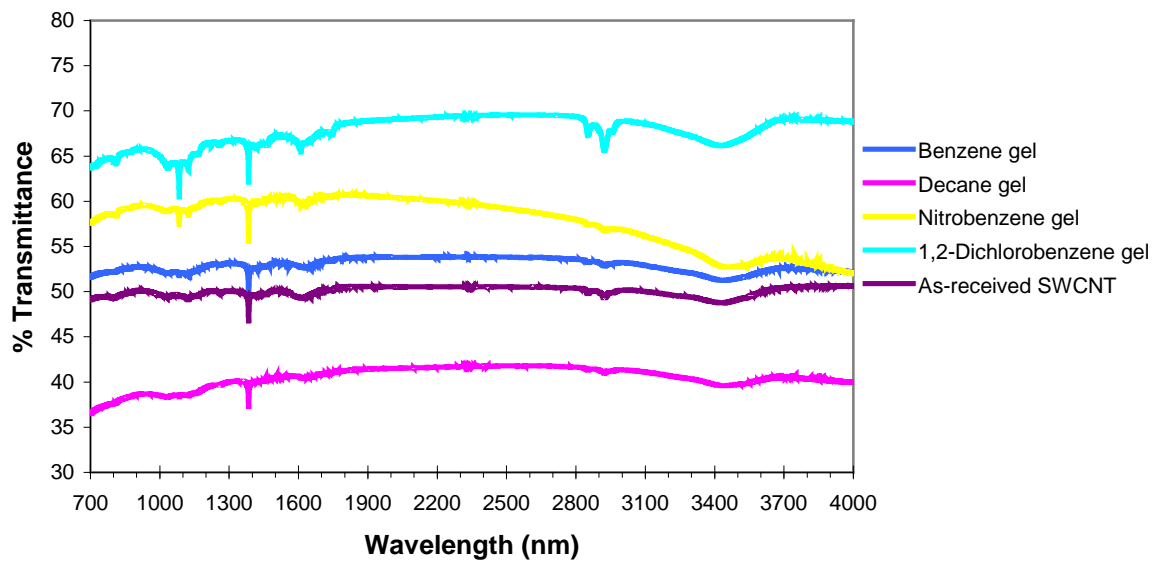


**Figure 2.6.** FTIR spectra of SWCNTs before and after 1 hour of sonication.

## Chapter 2

The FTIR spectra of all the dried SWCNT gels are practically identical to the spectrum of the as-received SWCNTs. Each spectra shows a small, strong peak at approximately  $1400\text{ cm}^{-1}$ , a weak broad set of peaks at  $\sim 3000\text{ cm}^{-1}$  and another small, broad peak at about  $1100\text{ cm}^{-1}$ . All of these peaks correspond to the presence of a carboxylic acid except the strong C = O peak between 1600-1710 is missing. If carboxylic acid groups were present, I would expect to see a very strong peak for the carbonyl group. Another possibility is that the observed peaks correspond to an alkene group, as they can have peaks in areas similar to those observed. One noticeable difference is that a strong peak appears to be coming in for the ODCB and nitrobenzene gel samples at  $1100\text{ cm}^{-1}$ . Only a broad peak in this region is seen for the other samples. One important conclusion that can be made from the FTIR data is that sonication of the SWCNTs at 100 W for 1 hour causes little to no observable chemical modification of the nanotubes. This, the lack of a strong carbonyl peak, the weakness of the observed % transmittance signal, and the fact that the gelation phenomenon is unique to SWCNTs as opposed to other carbon allotropes suggest that the SWCNT gels are formed via physical interactions, most likely strong  $\pi - \pi$  interactions, between the nanotubes instead of chemical linkages.

To observe any phase changes that might occur upon heating the gels, differential scanning calorimetry measurements were performed. Table 2.2 shows the data obtained from samples of benzene, 0.5 wt % SWCNT-benzene gel, and 1.0 wt % SWCNT-benzene gel. The only phase transition observed for all samples was the boiling point of benzene. The boiling point of benzene in the 0.5 wt % and 1.0 wt % SWCNT-benzene gels was increased approximately  $3\text{ }^{\circ}\text{C}$  and  $5\text{ }^{\circ}\text{C}$  from that of pure benzene, respectively.

## Chapter 2

Figure 2.7 shows the change in boiling point of benzene in the 1.0 wt % SWCNT-benzene gel as compared to that of pure benzene.

| Benzene         |       | 0.5 wt % Gel    |       | 1.0 wt % Gel    |       |
|-----------------|-------|-----------------|-------|-----------------|-------|
| Run 1 (°C)      | 79.09 | Run 1 (°C)      | 83.89 | Run 1 (°C)      | 84.50 |
| Run 2 (°C)      | 80.63 | Run 2 (°C)      | 84.18 | Run 2 (°C)      | 85.35 |
| Run 3 (°C)      | 80.15 | Run 3 (°C)      | 83.15 | Run 3 (°C)      | 85.13 |
| Run 4 (°C)      | 80.13 | Run 4 (°C)      | 83.14 | Run 4 (°C)      | 84.44 |
| Run 5 (°C)      | 80.31 | Run 5 (°C)      | 83.77 | Run 5 (°C)      | 85.92 |
| Run 6 (°C)      | 80.53 | Run 6 (°C)      | 83.29 | Run 6 (°C)      | 85.61 |
|                 |       |                 |       |                 |       |
| Avg. Temp (°C): | 80.14 | Avg. Temp (°C): | 83.57 | Avg. Temp (°C): | 85.16 |
| Std. Dev:       | 0.55  | Std. Dev:       | 0.44  | Std. Dev:       | 0.60  |
| Lit. bp (°C):   | 80.1  |                 |       |                 |       |

**Table 2.2.** DSC data for samples of benzene, 0.5 wt % SWCNT-benzene gel, and 1.0 wt % SWCNT-benzene gel.

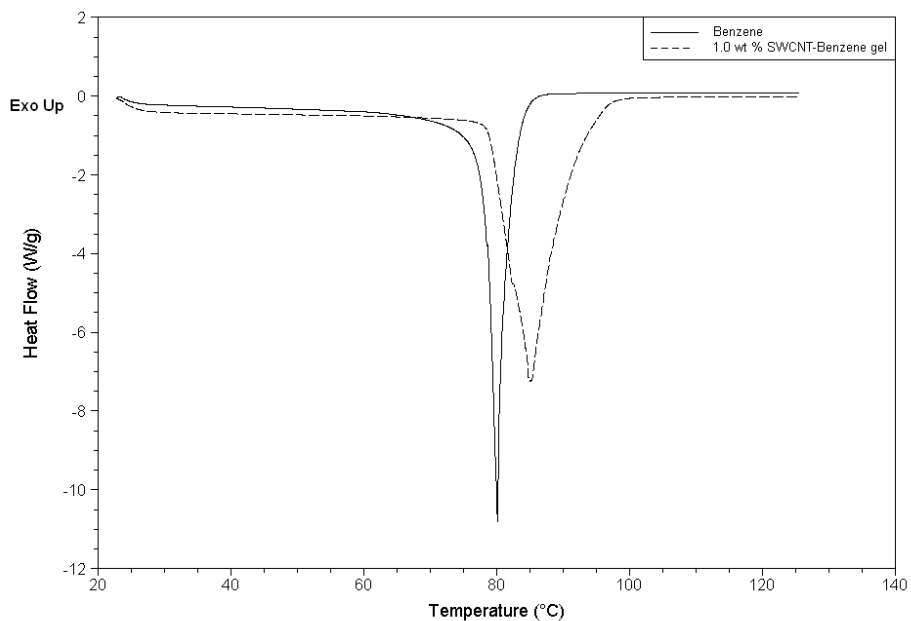


**Figure 2.7.** Increased boiling point of benzene in 1.0 wt % SWCNT-benzene gel as compared to the boiling point of pure benzene.

## Chapter 2

These results are not surprising when one considers the colligative properties of solutions, which are defined as properties of solutions that depend only upon the amount of solute present. The presence of a nonvolatile solute in a solution lowers the vapor pressure and increases the boiling point of the solvent. The more solute particles there are in the solution, the higher the boiling point of the solvent, which explains why the greatest temperature increase in the boiling point of benzene is observed in the 1.0 wt % SWCNT-benzene gel. The difference in peak sharpness in Figure 2.5 can be explained in a similar manner. The molecules in the pure benzene only have to overcome solvent-solvent interactions to vaporize, while the benzene molecules in the 1.0 wt % SWCNT-benzene gel must overcome solvent-solute interactions in addition to solvent-solvent interactions before they can be converted from liquid to vapor. Thus benzene molecules on the surface of the gel can vaporize relatively easily because they mostly have only solvent-solvent interactions to overcome. However, as the gel becomes more concentrated, the benzene molecules become trapped and it takes more energy to break the increased solvent-solute interactions, which results in the broad peak in Figure 2.6. The benzene-SWCNT energy of interaction was calculated to be approximately 3.7 kJ/mol. This value represents 7.5% of the heat of vaporization of benzene, which is 49.1 kJ/mol.<sup>22</sup>

Viscosity measurements of a 1.0 wt % SWCNT-benzene gel were taken to determine its fluid behavior. Fluids can be classified as either Newtonian or non-Newtonian. A Newtonian fluid is a fluid in which there is a linear relationship between shear stress and shear rate, resulting in a constant viscosity that is independent of the shear rate. However, the viscosity of a Newtonian fluid can change with temperature.

Within the non-Newtonian category, classification breaks down into time-independent fluids and time-dependent fluids. Within the category of time-independent non-Newtonian fluids there are three types of fluids: Bingham plastic, pseudoplastic, and dilatant fluids. Within the category of time-dependent non-Newtonian fluids there are two types of fluids, thixotropic and rheopectic fluids. Figure 2.8 shows the breakdown of the different types of non-Newtonian fluids.

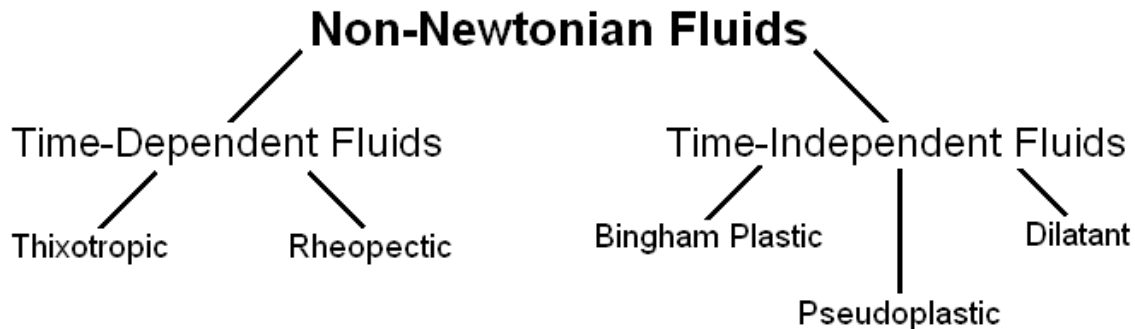


**Figure 2.8.** Breakdown of the different types of non-Newtonian fluids.

Thixotropic fluids show a reversible decrease in shear stress with time at a constant shear rate, while rheopectic show a reversible increase in shear stress with time at a constant shear rate. Examples of thixotropic fluids are somewhat common and include some types of polymer solutions, ketchup, and paint. Examples of rheopectic fluids are, on the other hand, very rare.

Figure 2.9 shows the behavior of the shear stress,  $\tau$ , as a function of shear rate,  $D$ , for Newtonian fluids as compared to the three types of time-independent non-Newtonian fluids. Pseudoplastic and dilatant fluids demonstrate a non-linear flow curve as the shear

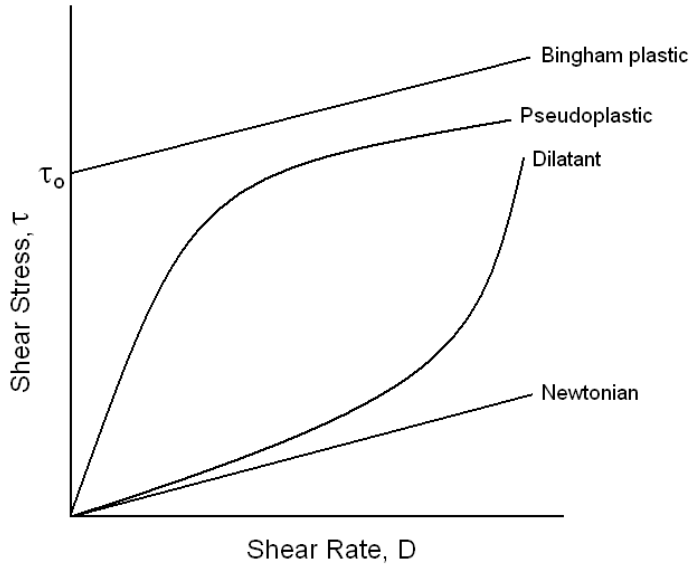


**Figure 2.9.** Graph of shear stress,  $\tau$ , vs. shear rate,  $D$ , for Newtonian and time-independent non-Newtonian fluids. The symbol  $\tau_0$  represents the yield stress of the Bingham plastic fluid.

rate is increased. The apparent viscosity of pseudoplastic fluids decreases as the shear rate increases, while for dilatant fluids the apparent viscosity increases as the shear rate increases. Bingham plastic fluids possess what is called a yield stress, and then exhibit a linear flow curve as the shear rate is increased after the yield stress is overcome. The yield stress is the point at which the viscosity can be measured; below the yield stress the rigidity of the structure is too much for the shear stress to overcome.

The graph of the shear stress data as a function of shear rate, as shown in Figure 2.10, demonstrates that the 1.0 wt % SWCNT-benzene gels exhibit what is called yield-pseudoplastic behavior. This is a combination of pseudoplastic and Bingham plastic fluid behavior. The gel behaves like a Bingham plastic in that it has a measured yield stress of

0.8264 Pa, but then as the shear rate is increased a non-linear flow curve is observed, much like a pseudoplastic fluid. Once the shear stress overcomes the intermolecular forces present in the SWCNT-benzene gel, then the SWCNT network isn't as rigid and the nanotubes are more mobile.

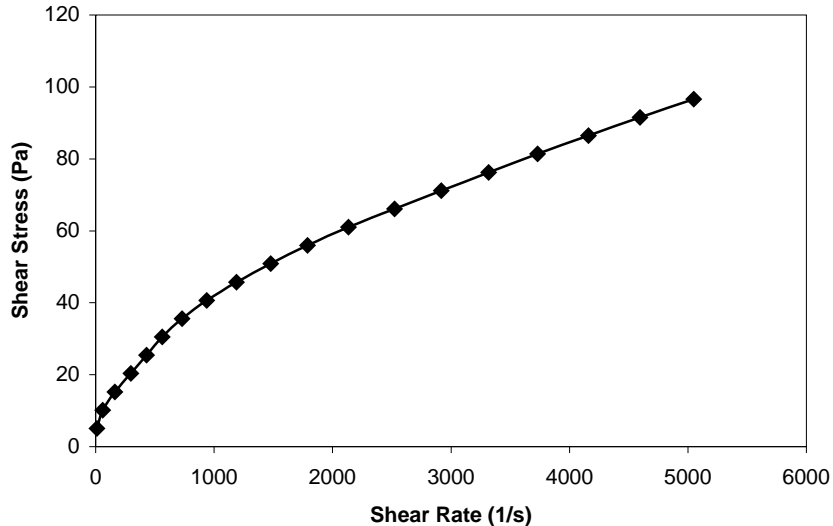


**Figure 2.10.** Shear stress as a function of shear rate for a 1.0 wt % SWCNT-benzene gel.

A typical pseudoplastic material does not possess a yield stress, and the flow curve of such materials passes through the origin. So the gel behaves like a combination of a Bingham plastic fluid until the yield stress is reached and a pseudoplastic fluid as the shear rate is increased after the yield stress is overcome.<sup>23, 24</sup>

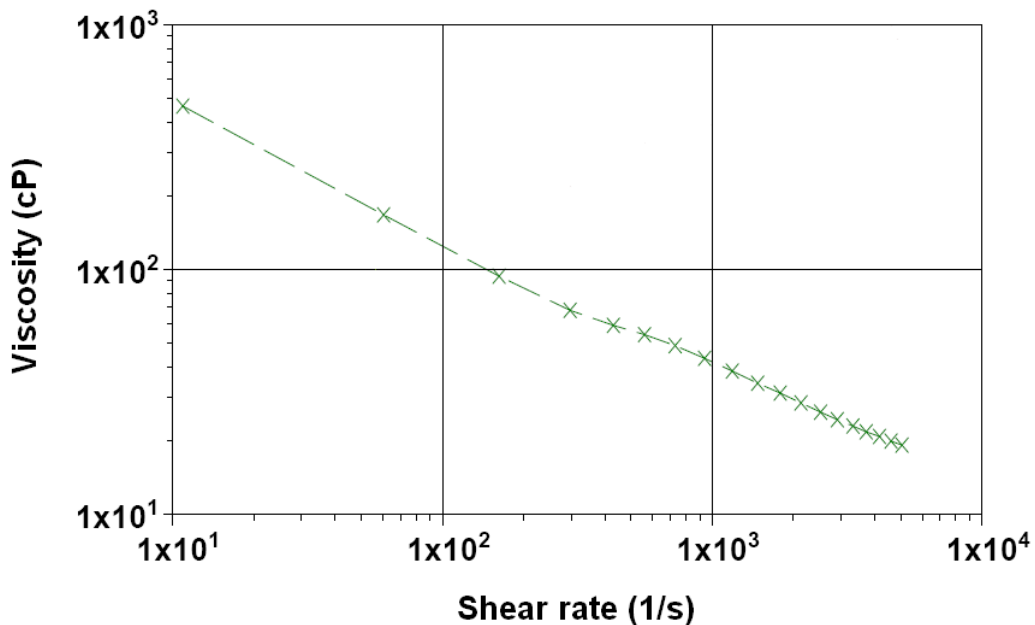


**Figure 2.11.** Viscosity as a function of shear rate for a 1.0 wt % SWCNT-benzene gel.

A graph of the viscosity data as a function of shear rate is shown in Figure 2.11. When viscosity is graphed as a function of shear rate, a Newtonian fluid results in a straight line with no slope. In other words, there is no change in the viscosity as the shear rate is increased. However, a non-Newtonian fluid exhibits a straight line with a negative slope, which means that the viscosity decreases with increasing shear rate. This behavior is also known as shear thinning. The graph of the viscosity data for the 1.0 wt % SWCNT-benzene gel vs. shear rate exhibits the behavior of a typical non-Newtonian fluid. Benzene is a Newtonian fluid, with a viscosity of 0.604 cP at 25 °C.<sup>22</sup>

The Herschel-Bulkley model (also known as the yield-power law model) was used to model the data. The equation serves as good model for yield-pseudoplastic

## Chapter 2

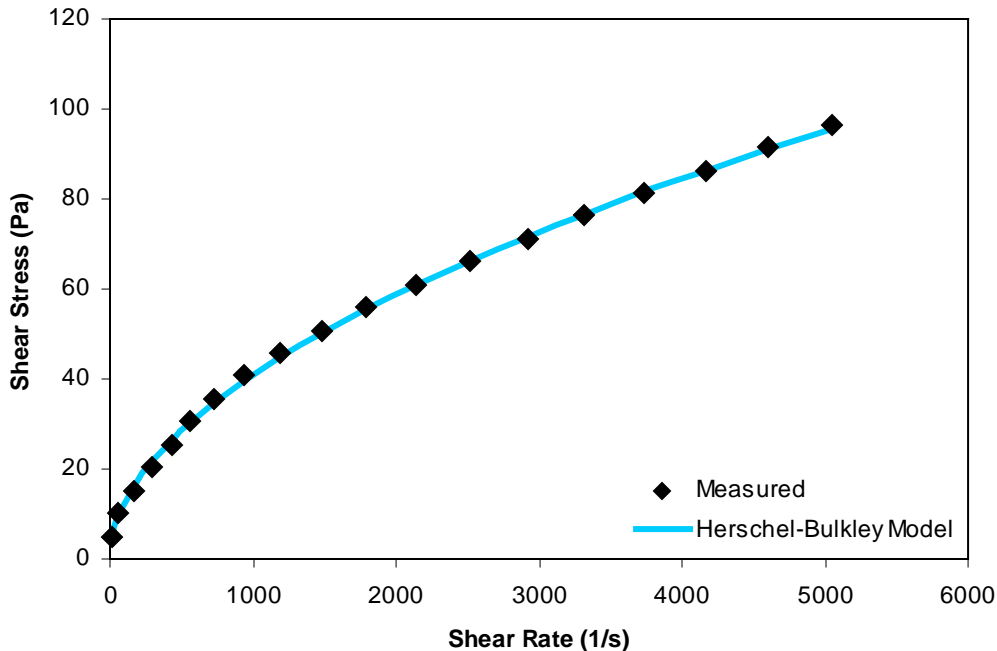
fluids, such as particulate suspensions, concrete, mud, and oil- and water-based drilling fluids. Equation 2.1 gives the Herschel-Bulkley model where  $\tau$  = shear stress,  $\tau_o$  = yield stress,  $k$  = consistency,  $\gamma$  = shear rate, and  $n$  = power law exponent.<sup>24, 25</sup>

$$\tau = \tau_o + k(\gamma)^n \quad \text{2.1}$$

The values of  $\tau_o$ ,  $k$ , and  $n$  were calculated for the 1.0 wt % SWCNT-benzene gel by performing a least squares regression on the shear rate and shear stress data, and are given in Equation 2.2, which was used to calculate the shear stress as a function of the shear rate for the 1.0 wt % SWCNT-benzene gel.

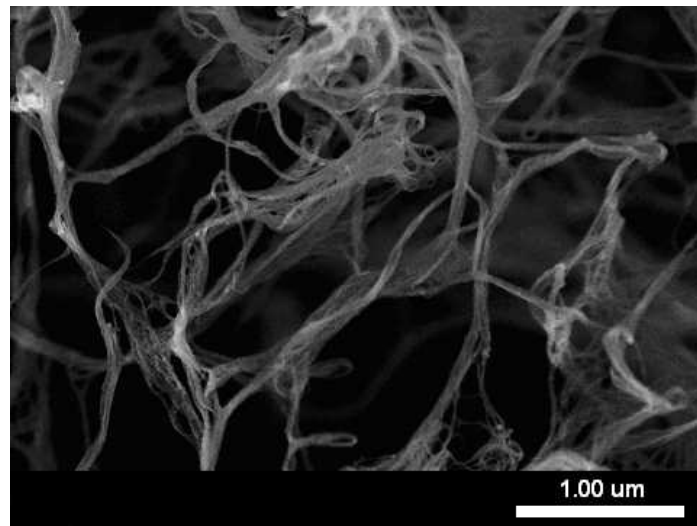
$$\tau = 0.8264 + 1.0111(\gamma)^{0.5326} \quad \text{2.2}$$

Figure 2.12 shows the graph of the measured shear stress data as compared to calculated shear stress values using the Herschel-Bulkley model. The graph shows that the measured data and calculated data are in very good agreement, so the Herschel-Bulkley model serves as a good model for the fluid behavior of the SWCNT gels.



**Figure 2.12.** The measured shear stress values and the calculated shear stress values using the Herschel-Bulkley model as functions of shear rate for a 1.0 wt % SWCNT-benzene gel.

The SWCNT foam was made from a bulk sample of 1.0 wt % SWCNT-benzene gel. Figure 2.13 shows an SEM micrograph taken at room temperature of a sample from a bulk piece of SWCNT foam. Not surprisingly, it looks much like the SEM micrograph taken under cryogenic conditions of a 1.0 wt % SWCNT-benzene gel. A similar foam was reported by Sano, however their SWCNT foam was prepared using a gelatin gel in aqueous solution as a template.<sup>26</sup>



**Figure 2.13.** SEM micrograph taken at room temperature of a bulk piece of SWCNT foam.

The SWCNT foam is considerably less dense than the 1.0 wt % SWCNT-benzene gel. Equations 2.3 and 2.4 show the equations used to calculate the density of the 1.0 wt % SWCNT-benzene gel and the SWCNT foam, respectively.

$$\rho_{\text{calc}} = \frac{\text{mass (g) Benzene} + \text{mass (g) SWCNT}}{2 \text{ mL gel}}$$

2.3

$$\rho_{\text{calc}} = \frac{\text{mass (g) SWCNT}}{2 \text{ mL foam}}$$

2.4

In a 1.0 wt % SWCNT-benzene gel, 0.0178 g of SWCNTs are used as well as 2 mL of benzene, which is equal to 1.757 g of benzene (density of benzene = 0.8786 g/mL). Thus the calculated density of the 1.0 wt % SWCNT-benzene gel is 0.9 g/mL. Because the SWCNT foam is synthesized from a 1.0 wt % SWCNT-benzene gel, the same amount of SWCNTs will be in 2 mL of the gel which, when sublimed, loses the benzene. Thus the calculated density of the SWCNT foam is 0.009 g/mL. It is important to note that these calculations are just estimates, as the volume of the foam may actually shrink from 2 mL during the sublimation process. Regardless, the gel is approximately 100 times more dense than the foam.

Because it has such a low density, yet a presumably high mechanical strength, the SWCNT foam could be a material of interest in many different areas of application. One such application could be for gas sorption. We have done preliminary studies to test the ability of the SWCNT foam versus *p*-*tert*-butylcalix[4]arene and a metal-organic framework (MOF) to adsorb methane both at room temperature and at – 70 °C. Figure 2.14 shows the structures of *p*-*tert*-butylcalix[4]arene and the metal-organic framework used, which is called MOF-5. The structure of MOF-5 is made up of octahedral shaped Zn-O-C clusters that are connected by 1,4-benzenedicarboxylic acid.<sup>27</sup>

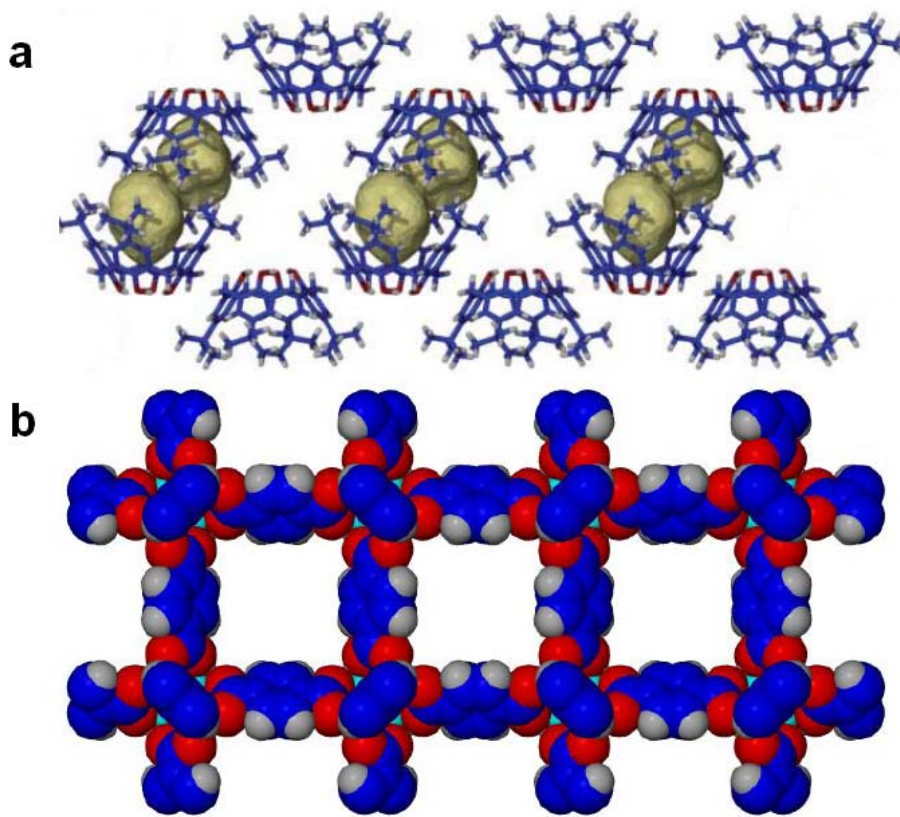


**Figure 2.14.** Structures of *p*-*tert*-butylcalix[4]arene (a) and metal-organic framework MOF-5 (b).

Figure 2.15 shows the methane sorption isotherms for the SWCNT foam, *p*-*tert*-butylcalix[4]arene, and MOF-5 at room temperature and at  $-70^{\circ}\text{C}$ . At room temperature, the calix[4]arene compound adsorbs the most methane after 140 minutes, while the foam and MOF-5 uptake very little methane. However, at  $-70^{\circ}\text{C}$ , the SWCNT foam adsorbs more methane after 25 minutes than even the calix[4]arene compound did at room temperature after 140 minutes, while the calix[4]arene and MOF-5 adsorb very little methane at this low temperature.<sup>28</sup> The amount of methane the SWCNT foam adsorbs was calculated to be 2.7 wt %.

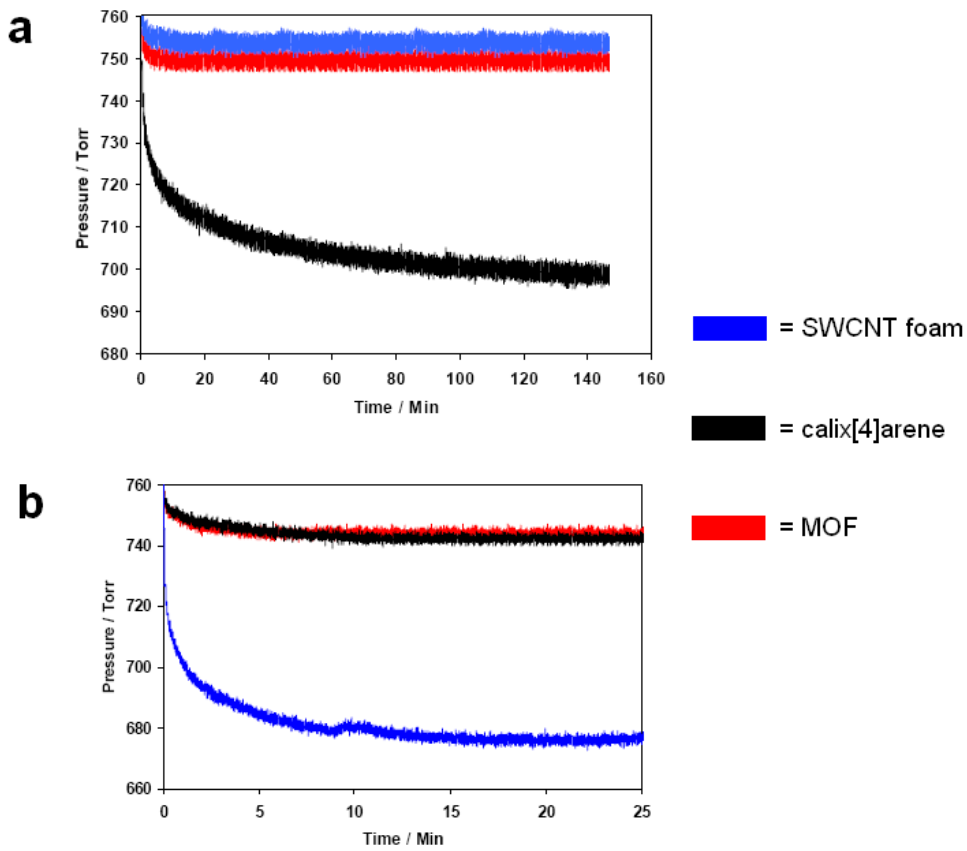


**Figure 2.15.** Methane sorption isotherms of SWCNT foam, *p*-*tert*-butylcalix[4]arene, and MOF-5 at room temperature (a) and at  $-70^{\circ}\text{C}$  (b).

Another potentially interesting application for the SWCNT foam is in the area of polymer composites. Much work has been done in the area of SWCNT-polymer composites,<sup>29-32</sup> although it would be exciting to see what our foam can add to this rapidly expanding field.

## 2.4 Conclusions

A wide variety of organic solvents can be used to make SWCNT gels, namely nonpolar, aromatic, and  $\pi$ -bond (double and triple bond) containing solvents. Polar, hydrogen-bonding solvents will not form SWCNT gels. Scanning electron microscopy shows that the structure of the SWCNT gels contains much less-entangled bundles of nanotubes compared to as-received SWCNTs. FTIR spectra show little to no chemical differences in any of the SWCNT gels after one hour of sonication, leading to the conclusion that sonication does no damage to the nanotubes that would cause them to gel. Therefore, the gelation phenomenon must be due to physical interactions of the SWCNT bundles rather than chemical crosslinking of the nanotubes. Differential scanning calorimetry demonstrates that interactions between the solvents and SWCNTs increase the boiling point of the solvent, as explained by the theory of colligative properties. Viscosity measurements proved that the gels behave as shear thinning time-independent non-Newtonian fluids, meaning the viscosity decreases as the shear rate increases. The Herschel-Bulkley model serves as a good model for describing the fluid behavior of the SWCNT-gels.

The SWCNT-benzene gel serves as a precursor to SWCNT foam. While their structures are very similar, the foam is 100 times less dense than its parent 1.0 wt % SWCNT-benzene gel. Its low density, yet potentially strong mechanical properties make it an appealing material for various applications from gas sorption to polymer composites.

## 2.5 References

1. Iijima, S., Helical Microtubules of Graphitic Carbon. *Nature* **1991**, 354, (6348), 56-58.
2. Iijima, S.; Ichihashi, T., Single-Shell Carbon Nanotubes of 1-Nm Diameter. *Nature* **1993**, 363, (6430), 603-605.
3. Bethune, D. S.; Kiang, C. H.; Devries, M. S.; Gorman, G.; Savoy, R.; Vazquez, J.; Beyers, R., Cobalt-Catalyzed Growth of Carbon Nanotubes with Single-Atomic-Layerwalls. *Nature* **1993**, 363, (6430), 605-607.
4. Information received from Carbon Nanotechnologies, Inc., 16200 Park Row, Houston, TX 77084.
5. Yu, M. F.; Files, B. S.; Arepalli, S.; Ruoff, R. S., Tensile loading of ropes of single wall carbon nanotubes and their mechanical properties. *Phys. Rev. Lett.* **2000**, 84, (24), 5552-5555.
6. Delozier, D. M.; Watson, K. A.; Smith, J. G.; Connell, J. W., Preparation and characterization of space durable polymer nanocomposite films. *Composites Sci. and Tech.* **2005**, 65, (5), 749-755.
7. Arepalli, S.; Fireman, H.; Huffman, C.; Moloney, P.; Nikolaev, P.; Yowell, L.; Higgins, C. D.; Kim, K.; Kohl, P. A.; Turano, S. P.; Ready, W. J., Carbon-nanotube-based electrochemical double-layer capacitor technologies for spaceflight applications. *JOM* **2005**, 57, (12), 26-31.
8. Landi, B. J.; Raffaelle, R. P.; Castro, S. L.; Bailey, S. G., Single-wall carbon nanotube-polymer solar cells. *Progress in Photovoltaics* **2005**, 13, (2), 165-172.
9. Fischer, J. E., Storing energy in carbon nanotubes. *Chemical Innovation* **2000**, 30, (10), 21-27.

## Chapter 2

10. Haas, M. K.; Zielinski, J. M.; Dantsin, G.; Coe, C. G.; Pez, G. P.; Cooper, A. C., Tailoring singlewalled carbon nanotubes for hydrogen storage. *J. Mat. Res.* **2005**, 20, (12), 3214-3223.
11. Lee, S. M.; An, K. H.; Kim, W. S.; Lee, Y. H.; Park, Y. S.; Seifert, G.; Frauenheim, T., Hydrogen storage in carbon nanotubes. *Synthetic Metals* **2001**, 121, (1-3), 1189-1190.
12. Sarkar, A.; Banerjee, R., A quantitative method for characterization of carbon nanotubes for hydrogen storage. *International Journal of Hydrogen Energy* **2004**, 29, (14), 1487-1491.
13. Tibbetts, G. G.; Meisner, G. P.; Olk, C. H., Hydrogen storage capacity of carbon nanotubes, filaments, and vapor-grown fibers. *Carbon* **2001**, 39, (15), 2291-2301.
14. Paredes, J. I.; Burghard, M., Dispersions of individual single-walled carbon nanotubes of high length. *Langmuir* **2004**, 20, (12), 5149-5152.
15. Bahr, J. L.; Mickelson, E. T.; Bronikowski, M. J.; Smalley, R. E.; Tour, J. M., Dissolution of small diameter single-wall carbon nanotubes in organic solvents? *Chem. Commun.* **2001**, (2), 193-194.
16. Landi, B. J.; Ruf, H. J.; Worman, J. J.; Raffaelle, R. P., Effects of alkyl amide solvents on the dispersion of single-wall carbon nanotubes. *J. Phys. Chem. B* **2004**, 108, (44), 17089-17095.
17. Star, A.; Stoddart, J. F., Dispersion and solubilization of single-walled carbon nanotubes with a hyperbranched polymer. *Macromolecules* **2002**, 35, (19), 7516-7520.
18. Fukushima, T.; Kosaka, A.; Ishimura, Y.; Yamamoto, T.; Takigawa, T.; Ishii, N.; Aida, T., Molecular ordering of organic molten salts triggered by single-walled carbon nanotubes. *Science* **2003**, 300, (5628), 2072-2074.
19. Winter, H. H., The Critical Gel: The Universal Material State between Liquid and Solid. In *Structure and dynamics of polymer and colloidal systems*, Borsali, R.; Pecora, R.; North Atlantic Treaty

## Chapter 2

- Organization. Scientific Affairs Division., Eds. Kluwer Academic: Dordrecht ; Boston, 2002; Vol. 568, pp 439-470.
20. Koshio, A.; Yudasaka, M.; Zhang, M.; Iijima, S., A simple way to chemically react single-walled carbon nanotubes with organic materials using ultrasonication. *Nano Letters* **2001**, 1, (7), 361-363.
  21. Koshio, A.; Yudasaka, M.; Iijima, S., Thermal degradation of ragged single-wall carbon nanotubes produced by polymer-assisted ultrasonication. *Chem. Phys. Lett.* **2001**, 341, (5-6), 461-466.
  22. CRC handbook of chemistry and physics. In 87th ed.; CRC Press: Cleveland, Ohio, 2006-2007.
  23. Geankolis, C. J., *Transport processes and unit operations*. 2nd ed.; Allyn and Bacon: Boston, 1983; p xi, 862 p.
  24. Chhabra, R. P.; Richardson, J. F., *Non-Newtonian flow in the process industries : fundamentals and engineering applications*. Butterworth-Heinemann: Oxford; Boston, MA, 1999; p 436.
  25. Hemphill, T.; Campos, W.; Pilehvari, A., Yield-Power Law Model More Accurately Predicts Mud Rheology. *Oil & Gas Journal* **1993**, 91, (34), 45-50.
  26. Nabeta, M.; Sano, M., Nanotube foam prepared by gelatin gel as a template. *Langmuir* **2005**, 21, (5), 1706-1708.
  27. Eddaoudi, M.; Kim, J.; Rosi, N.; Vodak, D.; Wachter, J.; O'Keefe, M.; Yaghi, O. M., Systematic design of pore size and functionality in isoreticular MOFs and their application in methane storage. *Science* **2002**, 295, (5554), 469-472.
  28. Thallapally, P. K.; Kirby, K. A.; Atwood, J. L., Comparison of porous and nonporous materials for methane storage. *New J. Chem.* **2007**, 31, (5), 628-630.

## Chapter 2

29. Li, D.; Zhang, X. F.; Sui, G.; Wu, D. H.; Liang, J.; Yi, X. S., Toughness improvement of epoxy by incorporating carbon nanotubes into the resin. *J. Mat. Sci. Lett.* **2003**, 22, (11), 791-793.
30. Liu, L. Q.; Wagner, H. D., Rubbery and glassy epoxy resins reinforced with carbon nanotubes. *Composites Sci. and Tech.* **2005**, 65, (11-12), 1861-1868.
31. Mahfuz, H.; Adnan, A.; Rangari, V. K.; Jeelani, S., Manufacturing and characterization of carbon nanotube/polyethylene composites. *Inter. J. of Nanosci.* **2005**, 4, (1), 55-72.
32. Ham, H. T.; Koo, C. M.; Kim, S. O.; Choi, Y. S.; Chung, I. J., Chemical modification of carbon nanotubes and preparation of polystyrene/carbon nanotubes composites. *Macro. Res.* **2004**, 12, (4), 384-390.

## Effects of Anion and Solvent Choice on the Structures of Copper(I) Coordination Polymers

### 3.1 Introduction

Much of the previous research in the Keller group has been focused upon creating metal-organic frameworks to replicate the various structures of silicate materials found in nature. Efforts have specifically been concentrated on the coordination of nitrogen-based ligands to Cu(I) centers. The nitrogen-containing ligands used most frequently by the Keller group are shown in Figure 3.1. Pyrimidine, 3,3'-bipyridine, and 4,4'-bipyridine, ligands have resulted in an acentric three-dimensional,<sup>1</sup> two-fold interpenetrating,<sup>2</sup> and two-dimensional pentagonal-cavity-containing<sup>3</sup> networks, respectively. In particular, the structures containing 3,3'-bipyridine and 4,4'-bipyridine as ligands yielded unexpected results due to the twisting of the C–C bond between the two phenyl rings of the ligands. Because of this, a more rigid ligand was sought and found in 4,7-phenanthroline (phen). However, the use of phen as a ligand resulted in unexpected coordination geometry around the Cu(I) center, introducing the rare distorted trigonal geometry to our group's library of structures.<sup>4,5</sup> With these combined results, it became very clear that the prediction of crystal structures is not an easily accomplished task.

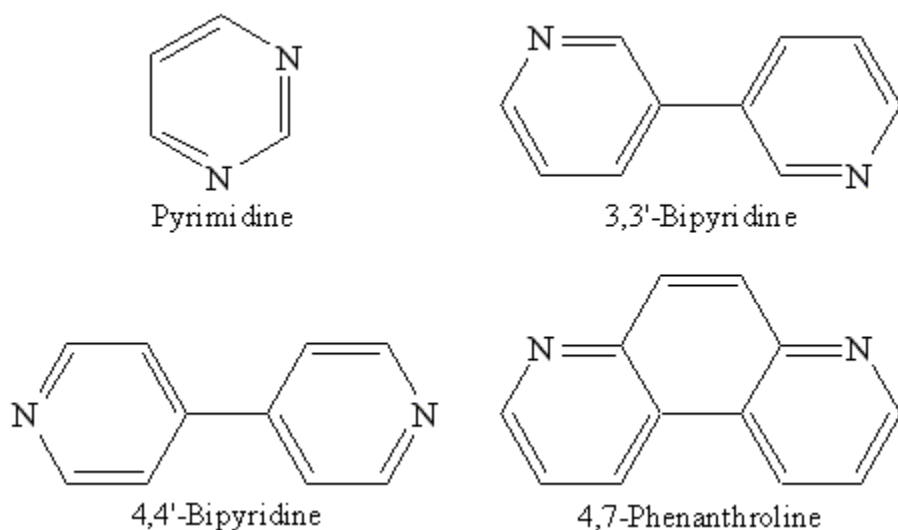


**Figure 3.1.** Common ligands used by the Keller group to form Cu(I) coordination polymers.

Today, many researchers are studying the phenomenon of crystal engineering – the art of combining metal centers and ligands together in an effort to obtain a certain desired structure or network. When attempting to engineer a crystal structure there are a few things one needs to consider. The most important factor to account for is any type of intermolecular interactions that might occur within the desired structure. Supramolecular interactions, such as electrostatic attractions, hydrogen bonding, cation –  $\pi$  interactions, and  $\pi$  –  $\pi$  interactions are among the common noncovalent interactions that can occur between molecules.<sup>6</sup> It is these noncovalent interactions that often determine how the molecules will pack together in three-dimensions. In addition to intermolecular interactions, synthesis conditions, like choice of metal center, ligand, solvent, and temperature must also be considered when attempting to engineer a particular network or structural design.

The area of coordination polymers is still relatively new, but has been growing rapidly in the past 20 years. Major contributors to the field include Omar Yaghi,<sup>7-9</sup> who is probably most well known for his work with porous metal-organic frameworks, and Mike Zaworotko who has concentrated his efforts toward the crystal engineering of coordination polymers.<sup>10-12</sup>

The results reported in this chapter are primarily focused on the structural changes observed when the solvent and counteranion are varied from acetonitrile (MeCN) to benzonitrile (PhCN) and  $\text{BF}_4^-$  to  $\text{PF}_6^-$ , respectively in Cu(I) compounds containing phen. The effects of changing the Cu(I) to phen ratio from 1:1 to 1:10 is also studied. In addition, these same effects will be studied in triphenylphosphine-containing materials. The synthesis of four new compounds is described, and these structures are compared to previously reported structures from our group. It is my hope that the knowledge gained by studying these structural changes will help advance our group's ability to better engineer similar structures and networks in the future.

## 3.2 Experimental

### *Materials and Methods*

Copper(I) oxide (Fisher), tetrafluoroboric acid, hexafluorophosphoric acid, triphenylphosphine (Aldrich), 4,7-phenanthroline (GFS Chemicals and Aldrich), benzonitrile (ACROS), nitrobenzene (Aldrich), acetonitrile, diethyl ether, hexanes, methylene chloride, and tetrahydrofuran (Fisher) were used without further purification unless otherwise noted in the synthesis. Thermogravimetric analyses were performed

## Chapter 3

using a TA Instruments Q500 TGA with an N<sub>2</sub> flow rate of 100 mL/min and a heating rate of 10 °C/min.

Powder X-ray diffraction (PXRD) patterns were collected using a Scintag X2 system at 40kV and 30mA for Cu ( $K_{\alpha} = 1.540562 \text{ \AA}$ ). A continuous scan was taken at 2.5° per min from 20° to 90° 2θ.

### *Synthesis*

#### *Starting Materials*

The syntheses of [Cu(MeCN)<sub>4</sub>]BF<sub>4</sub>, **1**, [Cu(PhCN)<sub>4</sub>]BF<sub>4</sub>, **2**, [Cu(MeCN)<sub>4</sub>]PF<sub>6</sub>, **3**, and [Cu(PhCN)<sub>4</sub>]PF<sub>6</sub>, **4**, are based upon previously reported methods.<sup>13, 14</sup>

#### [Cu(MeCN)<sub>4</sub>]BF<sub>4</sub>, **1**

In a 250 mL Erlenmeyer flask, copper(I) oxide (0.300 g, 2.10 mmol) was added to 80 mL of acetonitrile (MeCN) and stirred to form a slurry. Tetrafluoroboric acid (2 mL) was added in 0.5 mL aliquots with continuous stirring on a warm hotplate. The hotplate temperature was raised slightly to bring the mixture to a light boil until all of the copper(I) oxide (Cu<sub>2</sub>O) had dissolved. The resulting clear, light yellow solution was removed from the hotplate and allowed to cool to room temperature. The solution was then added dropwise into a Schlenk flask containing 300 mL of diethyl ether (Et<sub>2</sub>O), at which time a white precipitate formed. The precipitate was allowed to settle and excess Et<sub>2</sub>O was decanted from the flask. The precipitate was then dried under vacuum and stored in a desiccator.

## Chapter 3

### **[Cu(PhCN)<sub>4</sub>]BF<sub>4</sub>, 2**

In a 250 mL Erlenmeyer flask, Cu<sub>2</sub>O (0.300 g, 2.10 mmol) was added to 80 mL of benzonitrile (PhCN) and stirred to form a slurry. Tetrafluoroboric acid (2 mL) was added in 0.5 mL aliquots with continuous stirring on a warm hotplate. The hotplate temperature was raised slightly to bring the mixture to a light boil until all of the Cu<sub>2</sub>O had dissolved. The resulting clear, light yellow solution was removed from the hotplate and allowed to cool to room temperature. The solution was then added dropwise into a flask containing 300 mL of Et<sub>2</sub>O, at which time a white precipitate formed. The white precipitate was collected via vacuum filtration, dried under vacuum, and stored in a desiccator.

### **[Cu(MeCN)<sub>4</sub>]PF<sub>6</sub>, 3**

In a 250 mL Erlenmeyer flask, Cu<sub>2</sub>O (0.300 g, 2.10 mmol) was added to 80 mL of MeCN and stirred to form a slurry. Hexafluorophosphoric acid (2 mL) was added in 0.5 mL aliquots continuous stirring on a warm hotplate. The hotplate temperature was raised slightly to bring the mixture to a light boil until all of the Cu<sub>2</sub>O had dissolved. The resulting clear, light yellow solution was removed from the hotplate and allowed to cool to room temperature. The solution was then added dropwise into a Schlenk flask containing 300 mL of Et<sub>2</sub>O, at which time a white precipitate formed. The precipitate was allowed to settle and excess Et<sub>2</sub>O was decanted from the flask. The precipitate was then dried under vacuum and stored in a desiccator.

## Chapter 3

### **[Cu(PhCN)<sub>4</sub>]PF<sub>6</sub>, 4**

In a 250 mL Erlenmeyer flask, Cu<sub>2</sub>O (0.300 g, 2.10 mmol) was added to 80 mL of PhCN and stirred to form a slurry. Hexafluorophosphoric acid (2 mL) was added in 0.5 mL aliquots with continuous stirring on a warm hotplate. The hotplate temperature was raised slightly to bring the mixture to a light boil until all of the Cu<sub>2</sub>O had dissolved. The resulting clear, light yellow solution was removed from the hotplate and allowed to cool to room temperature. The solution was then added dropwise into a flask containing 300 mL of Et<sub>2</sub>O, at which time a white precipitate formed. The white precipitate was collected via vacuum filtration, dried under vacuum, and stored in a desiccator.

### **[Cu(MeCN)<sub>2</sub>(PPh<sub>3</sub>)<sub>2</sub>]BF<sub>4</sub>, 5**

In a 250 mL Erlenmeyer flask, **1** (0.300 g, 0.396 mmol) was dissolved in 30 mL of methylene chloride (CH<sub>2</sub>Cl<sub>2</sub>), after which 2.0 mol equivalents (0.208 g) of triphenylphosphine (PPh<sub>3</sub>) was added and also allowed to dissolve with continuous stirring on a warm hotplate. The resulting clear solution was allowed to cool to room temperature. The solution was then added dropwise into a flask containing 300 mL of hexanes, at which time a white precipitate formed. The white precipitate was collected via vacuum filtration, dried under vacuum, and stored in a desiccator.

### **[Cu(PhCN)<sub>2</sub>(PPh<sub>3</sub>)<sub>2</sub>]BF<sub>4</sub>, 6**

In a 250 mL Erlenmeyer flask, **2** (0.300 g, 0.340 mmol) was dissolved in 30 mL of CH<sub>2</sub>Cl<sub>2</sub>, after which 2.0 mol equivalents (0.179 g) of PPh<sub>3</sub> was added and also allowed to dissolve with continuous stirring on a warm hotplate. The resulting clear solution was

## Chapter 3

allowed to cool to room temperature. The solution was then added dropwise into a flask containing 300 mL of hexanes, at which time a white precipitate formed. The white precipitate was collected via vacuum filtration, dried under vacuum, and stored in a desiccator.

### **[Cu(MeCN)<sub>2</sub>(PPh<sub>3</sub>)<sub>2</sub>]PF<sub>6</sub>, 7**

In a 250 mL Erlenmeyer flask, **3** (0.300 g, 0.368 mmol) was dissolved in 30 mL of CH<sub>2</sub>Cl<sub>2</sub>, after which 2.0 mol equivalents (0.193 g) of PPh<sub>3</sub> was added and also allowed to dissolve with continuous stirring on a warm hotplate. The resulting clear solution was allowed to cool to room temperature. The solution was then added dropwise into a flask containing 300 mL of hexanes, at which time a white precipitate formed. The white precipitate was collected via vacuum filtration, dried under vacuum, and stored in a desiccator.

### **[Cu(PhCN)<sub>2</sub>(PPh<sub>3</sub>)<sub>2</sub>]PF<sub>6</sub>, 8**

In a 250 mL Erlenmeyer flask, **4** (0.300 g, 0.319 mmol) was dissolved in 30 mL of CH<sub>2</sub>Cl<sub>2</sub>, after which 2.0 mol equivalents (0.168 g) of PPh<sub>3</sub> was added and also allowed to dissolve with continuous stirring on a warm hotplate. The resulting clear solution was allowed to cool to room temperature. The solution was then added dropwise into a flask containing 300 mL of hexanes, at which time a white precipitate formed. The white precipitate was collected via vacuum filtration, dried under vacuum, and stored in a desiccator.

### *New Compounds*

#### **[Cu(phen)(MeCN)<sub>2</sub>]PF<sub>6</sub>, 9**

In a 1-dram vial, **3** (0.030 g, 0.081 mmol) was dissolved in 0.5 mL acetonitrile and diluted with 1 mL nitrobenzene. Then 4,7-phenanthroline (0.0145 g, 0.0805 mmol) was added to the solution. The 1-dram vial was placed in a 20-dram vial containing 3 mL THF. Yellow, plate-like crystals of **9** were observed after a couple of days.

#### **[Cu(phen)(MeCN)(THF)<sub>0.5</sub>]PF<sub>6</sub>, 10**

In a 1-dram vial, **3** (0.030 g, 0.081 mmol) was dissolved in 0.5 mL acetonitrile and diluted with 3 mL nitrobenzene. Then 4,7-phenanthroline (0.145 g, 0.805 mmol) was added to the solution. The 1-dram vial was placed in a 20-dram vial containing 3 mL THF. A yellow precipitate formed within a couple of days. Yellow, plate-like crystals of **10** were observed after several days.

#### **[Cu<sub>2</sub>(phen)<sub>4</sub>](PF<sub>6</sub>)<sub>2</sub> · 1.5PhNO<sub>2</sub>, 11**

In a 1-dram vial, **4** (0.030 g, 0.048 mmol) was dissolved in 0.5 mL benzonitrile and diluted with 3 mL nitrobenzene. Then 4,7-phenanthroline (0.087 g, 0.48 mmol) was added to the solution. The 1-dram vial was placed in a 20-dram vial containing 3 mL diethyl ether. Yellow, plate-like crystals of **11** were observed after several days.

#### **[Cu(phen)(PPh<sub>3</sub>)]PF<sub>6</sub> · 2PhNO<sub>2</sub>, 12**

This material can be synthesized using **7** or **8**. In a 1-dram vial, **7** (0.030 g, 0.037 mmol) was dissolved in 1 mL nitrobenzene and then 4,7-phenanthroline (0.0066 g, 0.037

## Chapter 3

mmol) was added to the solution. The 1-dram vial was placed in a 20-dram vial containing 5 mL diethyl ether. Colorless, needle-like crystals of **12** were observed after a couple of days.

Alternatively, in a 1-dram vial, **8** (0.030 g, 0.032 mmol) was dissolved in 1 mL nitrobenzene and then 4,7-phenanthroline (0.0058 g, 0.032 mmol) was added to the solution. The 1-dram vial was placed in a 20-dram vial containing 5 mL diethyl ether. Colorless, needle-like crystals of **12** were observed after a couple of days.

### *Crystal Structure Analysis*

Single crystals, as determined by polarized optical microscopy, were placed in an inert oil and then mounted with silicone grease on a thin glass fiber. Full hemispheres of data were collected using a Siemens SMART system equipped with a CCD area detector ( $\text{Mo(K}_\alpha\text{)} = 0.71073 \text{ \AA}$ ), and absorption corrections were applied after integration.<sup>15</sup> All structures were solved using SHELXS Direct Methods,<sup>16</sup> and then refined using a full least squares treatment on  $F^2$ .<sup>16, 17</sup>

All non-hydrogen atoms in each structure were refined with anisotropic thermal parameters unless otherwise noted. All hydrogen atom positions were calculated. Crystallographic details for **9-12** are listed in Table 3.1.

The entire  $\text{PF}_6^-$  anion in **9** was found to be disordered. The thermal ellipsoids show elongated positions of five of the fluorine atoms. However, only the electron density of one fluorine atom showed enough distance that the fluorine could be split and modeled in two positions. This fluorine atom was split into parts F5 and F5A, and both were assigned site occupancies of 0.5. Fractional site occupancies were assigned based

### Chapter 3

on the thermal parameter of each atom,  $U_{\text{iso}}$ . The electron density around the other five fluorine atoms was too closely blended together, so each of those fluorine atoms could only be modeled in one position per atom. Small residual electron density remains around the anion and Cu(I) center.

The weakly coordinated THF molecule in **10** is bent and disordered over a center of symmetry. Atom O1 was assigned a site occupancy of 0.5 and refined with isotropic thermal parameters. Four of the six fluorine atoms of the  $\text{PF}_6^-$  anion were found to be disordered, split into parts F2, F2A, F3, F3A, F4, F4A, F5, and F5A, and assigned site occupancies of 0.7, 0.3, 0.7, 0.3, 0.8, 0.2, 0.6, and 0.4, respectively. Fractional site occupancies were assigned based on the thermal parameter of each atom,  $U_{\text{iso}}$ . Small residual electron density remains around the anion, THF molecule, and Cu(I) center.

One of the nitrobenzene molecules in **11** was found to be disordered to two orientations about a center of symmetry. Atom C59 shares the same position as atom N10, and therefore each was assigned a site occupancy of 0.5 and refined with isotropic thermal parameters. Atoms O3, O4, C57, and C58 were also assigned site occupancies of 0.5 each and all were refined with isotropic thermal parameters. Four of the six fluorine atoms of one of the  $\text{PF}_6^-$  anions were found to be disordered, split into parts F8, F8A, F9, F9A, F10, F10A, F11, and F11A, and assigned site occupancies of 0.7, 0.3, 0.7, 0.3, 0.8, 0.2, 0.7, and 0.3, respectively. Fractional site occupancies were assigned based on the thermal parameter of each atom,  $U_{\text{iso}}$ . Atoms F10A and F11A were refined with isotropic thermal parameters. Small residual electron density remains around the anions, solvent molecules, and Cu(I) centers.

## Chapter 3

Four of the six fluorine atoms of the  $\text{PF}_6^-$  anion in **12** (synthesized from **7**) were found to be disordered, split into parts F2, F2A, F3, F3A, F4, F4A, F5, and F5A, and assigned site occupancies of 0.6, 0.4, 0.6, 0.4, 0.5, 0.5, 0.5, and 0.5, respectively. Fractional site occupancies were assigned based on the thermal parameter of each atom,  $U_{\text{iso}}$ . Small residual electron density remains around the anion, solvent molecules, and Cu(I) center.

Four of the six fluorine atoms of the  $\text{PF}_6^-$  anion in **12** (synthesized from **8**) were found to be disordered, split into parts F2, F2A, F3, F3A, F4, F4A, F5, and F5A, and assigned site occupancies of 0.5, 0.5, 0.5, 0.5, 0.5, 0.5, 0.5, 0.6, and 0.4, respectively. Fractional site occupancies were assigned based on the thermal parameter of each atom,  $U_{\text{iso}}$ . Small residual electron density remains around the anion, solvent molecules, and Cu(I) center.

### Chapter 3

**Table 3.1:** Selected crystallographic details for **9-12**.

|  | <b>9</b>  | <b>10</b>   | <b>11</b>  | <b>12 from 7</b>  | <b>12 from 8</b>  |
|--|---|---|--|---|---|
| Empirical formula                              | CuC <sub>16</sub> H <sub>14</sub> N <sub>4</sub> PF <sub>6</sub>                            | CuC <sub>16</sub> H <sub>11</sub> N <sub>3</sub> O <sub>0.5</sub> PF <sub>6</sub>           | Cu <sub>2</sub> C <sub>57.5</sub> H <sub>37</sub> N <sub>0.5</sub> O <sub>3</sub> P <sub>2</sub> F <sub>12</sub>                             | CuC <sub>42</sub> H <sub>33</sub> N <sub>4</sub> O <sub>4</sub> P <sub>2</sub> F <sub>6</sub> | CuC <sub>42</sub> H <sub>33</sub> N <sub>4</sub> O <sub>4</sub> P <sub>2</sub> F <sub>6</sub> |
| Formula weight (g/mol)                         | 470.82  | 461.79  | 1325.99  | 897.20  | 897.20  |
| Crystal system, space group                    | Monoclinic, P2(1)/c   | Monoclinic, P2(1)/c   | Triclinic, P-1   | Orthorhombic, Pbca  | Orthorhombic, Pbca  |
| Temperature (K)                                | 173(2)  | 173(2)  | 173(2)   | 173(2)  | 173(2)  |
| Unit cell dimensions (Å, deg)                  | <i>a</i> = 10.034(1)<br><i>b</i> = 11.881(2)<br><i>c</i> = 14.902(2)<br>$\beta$ = 93.914(2) | <i>a</i> = 9.0534(7)<br><i>b</i> = 12.887(1)<br><i>c</i> = 14.779(1)<br>$\beta$ = 90.408(1) | <i>a</i> = 12.233(3)<br><i>b</i> = 14.675(4)<br><i>c</i> = 15.479(4)<br>$\alpha$ = 96.937(4)<br>$\beta$ = 103.507(4)<br>$\gamma$ = 92.643(4) | <i>a</i> = 19.323(6)<br><i>b</i> = 15.053(4)<br><i>c</i> = 26.621(8)                          | <i>a</i> = 19.353(1)<br><i>b</i> = 15.104(1)<br><i>c</i> = 26.667(2)                          |
| Volume (Å <sup>3</sup> )                       | 1772.5(3)   | 1724.2(2)   | 2674.1(2)  | 7744(4)   | 7795.1(8)   |
| Z, ρ calc (g/cm <sup>3</sup> )                 | 4, 1.7641   | 4, 1.779  | 2, 1.647   | 8, 1.539  | 8, 1.529  |
| Absorption coefficient (mm <sup>-1</sup> )     | 1.392   | 1.430   | 0.955  | 0.725   | 0.721   |
| F(000)   | 944   | 920   | 1337   | 3664  | 3664  |
| Crystal size (mm)                              | 0.5 × 0.3 × 0.2   | 0.5 × 0.25 × 0.15   | 0.25 × 0.2 × 0.1   | 0.4 × 0.2 × 0.1   | 0.6 × 0.15 × 0.1  |
| Θ Range for data collection (deg)              | 2.19 to 22.39   | 2.75 to 27.15   | 2.35 to 26.13  | 2.61 to 22.89   | 2.50 to 26.94   |
| Reflections collected/unique                   | 11977 / 3904<br>[R <sub>int</sub> =0.0858]  | 12058 / 3794<br>[R <sub>int</sub> =0.0217]  | 18665 / 11523<br>[R <sub>int</sub> =0.0404]  | 50845 / 8492<br>[R <sub>int</sub> =0.1351]  | 51961 / 8618<br>[R <sub>int</sub> =0.0772]  |
| Max. and min. transmission                     | 0.7681 and 0.4922   | 0.8141 and 0.5778   | 0.9106 and 0.6115  | 0.9310 and 0.6641   | 0.9314 and 0.6944   |
| Data / restraints / parameters                 | 3904 / 0 / 264  | 3794 / 0 / 285  | 11523 / 0 / 784  | 8492 / 0 / 568  | 8618 / 0 / 568  |
| Final R indices [I>2σ(I)] <sup>a,b</sup>       | R <sub>1</sub> = 0.0822,<br>wR <sub>2</sub> = 0.1797  | R <sub>1</sub> = 0.0471,<br>wR <sub>2</sub> = 0.1332  | R <sub>1</sub> = 0.0643,<br>wR <sub>2</sub> = 0.1383   | R <sub>1</sub> = 0.0778,<br>wR <sub>2</sub> = 0.2005  | R <sub>1</sub> = 0.0567,<br>wR <sub>2</sub> = 0.1253  |
| R indices (all data)                           | R <sub>1</sub> = 0.1552,<br>wR <sub>2</sub> = 0.2078  | R <sub>1</sub> = 0.0545,<br>wR <sub>2</sub> = 0.1404  | R <sub>1</sub> = 0.1246,<br>wR <sub>2</sub> = 0.1629   | R <sub>1</sub> = 0.1623,<br>wR <sub>2</sub> = 0.2438  | R <sub>1</sub> = 0.1035,<br>wR <sub>2</sub> = 0.1443  |
| Largest diff. peak / hole (e.Å <sup>-3</sup> ) | 0.76 / 0.94   | 0.73 / 0.58   | 0.72 / 0.67  | 1.16 / 1.54   | 0.91 / 0.48   |
| GoF on F <sup>2</sup>                          | 1.051   | 1.061   | 1.014  | 1.092   | 1.051   |

Structures were refined on F<sub>o</sub><sup>2</sup> using all data. <sup>a</sup>R = Σ(|F<sub>o</sub>| - |F<sub>c</sub>|) / Σ|F<sub>o</sub>|; <sup>b</sup>wR<sub>2</sub> = [Σ(|F<sub>o</sub>| - |F<sub>c</sub>|)<sup>2</sup> / Σ|F<sub>o</sub>|<sup>2</sup>]<sup>1/2</sup>

### 3.3 Results and Discussion

Compound **9** results from a 1:1 ratio of **3** to phen, and is a polymorph of the previously reported  $[\text{Cu}(\text{phen})(\text{MeCN})_2]\text{PF}_6$  structure by Lopez and Keller.<sup>4</sup> We see the same 1:1 ratio of Cu(I) to phen in **9** that was used in the synthesis. The coordination environment around the Cu(I) centers of both compounds are identical, with two phen and two MeCN ligands forming a distorted tetrahedral shape, as shown in Figure 3.2. Selected bond lengths and angles in **9** are listed in Table 3.2.

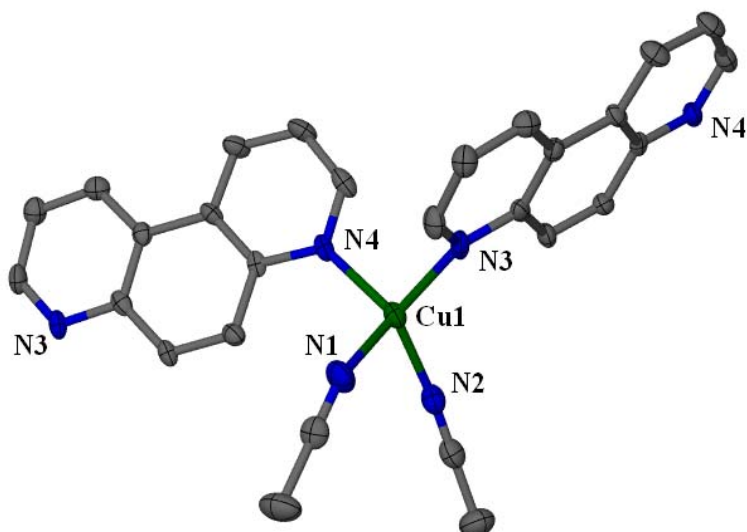


**Figure 3.2.** Coordination environment of the unique Cu(I) center in **9**. All atoms are shown as 50% probability thermal ellipsoids. Hydrogen atoms have been omitted for clarity. Copper is shown in green, nitrogen in blue, and carbon in gray.

| Bond Lengths (Å)       | Bond Angles (deg)             |
|------------------------|-------------------------------|
| Cu(1) – N(1): 1.954(6) | N(1) – Cu(1) – N(2): 93.6(2)  |
| Cu(1) – N(2): 2.172(6) | N(1) – Cu(1) – N(3): 125.6(2) |
| Cu(1) – N(3): 2.050(5) | N(1) – Cu(1) – N(4): 121.8(2) |
| Cu(1) – N(4): 2.075(5) | N(2) – Cu(1) – N(3): 109.4(2) |
|                        | N(2) – Cu(1) – N(4): 99.9(2)  |
|                        | N(3) – Cu(1) – N(4): 102.4(2) |

**Table 3.2.** Selected bond lengths and angles in **9**.

The difference between **9** and the previously reported [Cu(phen)(MeCN)<sub>2</sub>]PF<sub>6</sub> structure, however, is apparent when one looks at the chains that are formed by each structure. In the previously reported structure, the phenyl groups bridge the Cu(I) centers in such a way as one Cu(I) appears *trans* to its neighboring Cu(I) centers, while in **9** the phenyl groups bridge the Cu(I) centers in such a way as one Cu(I) appears *cis* to its neighboring Cu(I) centers. A comparison of the two chains can be seen in Figure 3.3. The angle between the Cu(I) centers in the *trans* structure is ~97°, while in the *cis* structure the same angle is ~145°. The only difference in the synthesis of the two compounds is that the previously reported structure used 3 mL nitrobenzene, while **9** was synthesized using only 1 mL nitrobenzene. It is odd that this small difference in nitrobenzene concentration could cause such a change in structure, especially because there is no nitrobenzene present in either structure.

Because of the difference in the chain structures between **9** and the previously reported [Cu(phen)(MeCN)<sub>2</sub>]PF<sub>6</sub>, their respective extended structures are also unique. However, the packing in both is governed by the π – π stacking occurring between phenyl groups.

on neighboring chain, as can be seen in **9** in Figure 3.4. Figure 3.5 shows the packing of the *cis* chains in **9** within the unit cell looking down the *b*-axis.

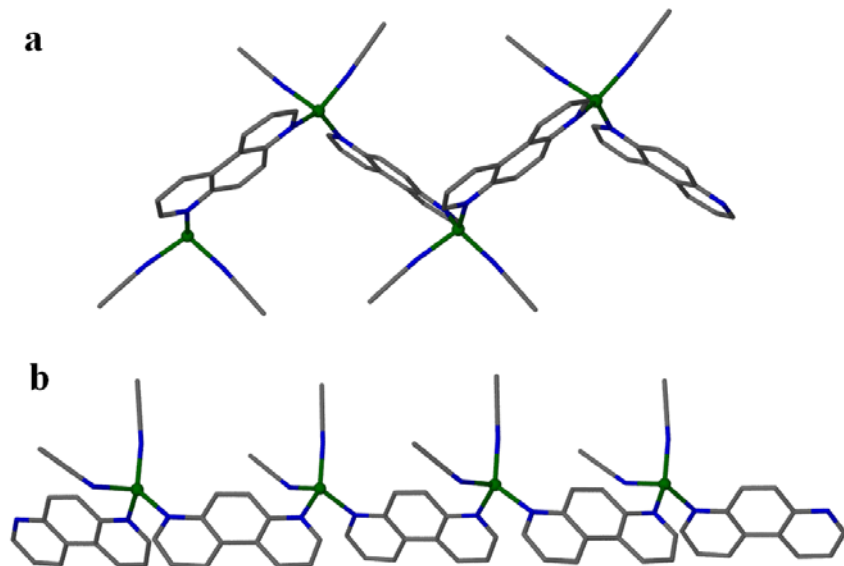


**Figure 3.3.** Comparison of the *trans* chains of the previously reported  $[\text{Cu}(\text{phen})(\text{MeCN})_2]\text{PF}_6$  (a) and the *cis* chains of **9** (b).

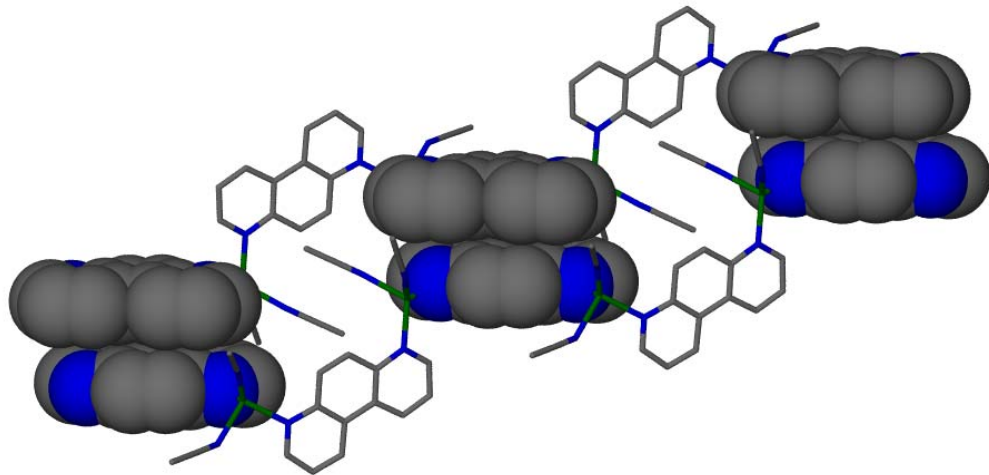


**Figure 3.4.** Space-fill view of the  $\pi - \pi$  stacking between phens of neighboring chains in **9**.

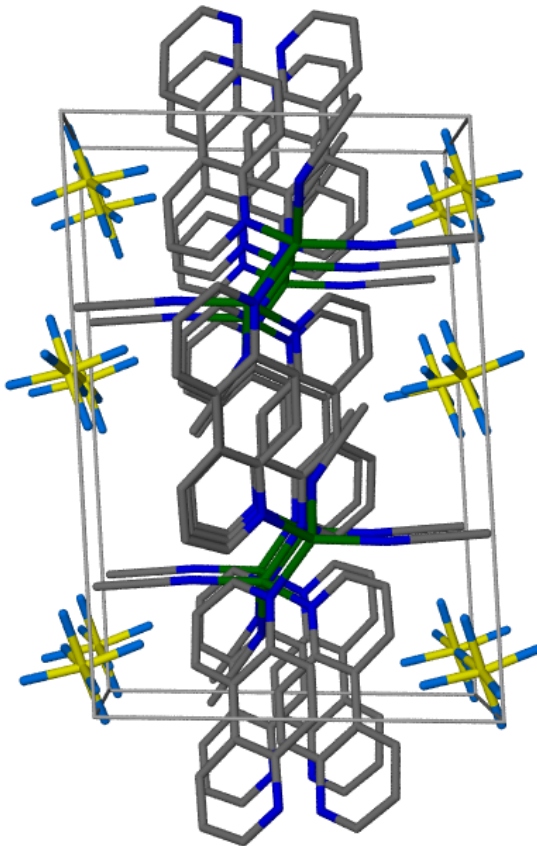


**Figure 3.5.** Packing diagram of neighboring *cis* chains of **9** viewed down the *b*-axis.

The angle between the phen molecules on the unique Cu(I) center in **9** is a bit small ( $\sim 102^\circ$ ). This is likely due to the  $\pi - \pi$  stacking of phens on neighboring chains governing the structure. The phens that do not participate in  $\pi - \pi$  stacking do not have much freedom to rotate away from their adjacent,  $\pi$ -stacking neighbors since they are connected between two Cu(I) centers. This keeps them rigid and forces the angle between the phens on the Cu(I) center to be smaller.

## Chapter 3

One of the acetonitrile ligands in **9** is bent, which is also a bit unusual. In the previously reported  $[\text{Cu}(\text{phen})(\text{MeCN})_2]\text{PF}_6$  structure, neither of the coordinated acetonitrile molecules is bent. Again, it is likely that this bending is another result of the  $\pi - \pi$  stacking occurring in the structure of **9**.

Thermogravimetric analysis of **9** shows two distinct weight losses, which can be seen in Figure 3.6. Powder X-ray diffraction (PXRD) was performed on the TGA residue of **9**. The observed peaks in the PXRD pattern correspond to peaks known for Al (from the sample holder) and Cu metal (Figure 3.7).<sup>18</sup> This is convincing evidence that the TGA residue of **9** is Cu. Unfortunately the observed weight % of the residue does not correspond to that calculated for the Cu residue (19.97 % observed, 13.50 % calculated). Since these values are off, the rest of the weight loss percentages of the material cannot be accurately determined. However, it is likely that the first weight loss corresponds to the loss of the two MeCN molecules (16.01 % observed, 17.44 % calculated) and the second weight loss corresponds to the loss of the phenanthroline ligand and the  $\text{PF}_6^-$  anion (64.01 % observed, 69.07 % calculated). The anion cannot be lost alone, but since the mechanism of reduction to Cu is unknown and all the atoms of the anion must be lost if the residue is indeed only Cu, the calculations will list the loss of the anion as a separate species for now. It is not known at this time why there is such a large difference in the observed and calculated weight % of the residue. There does not appear to be any significant amount of amorphous material in the residue according to the PXRD pattern, but it could still be a possible source of error. Further experiments will need to be performed to determine the cause.

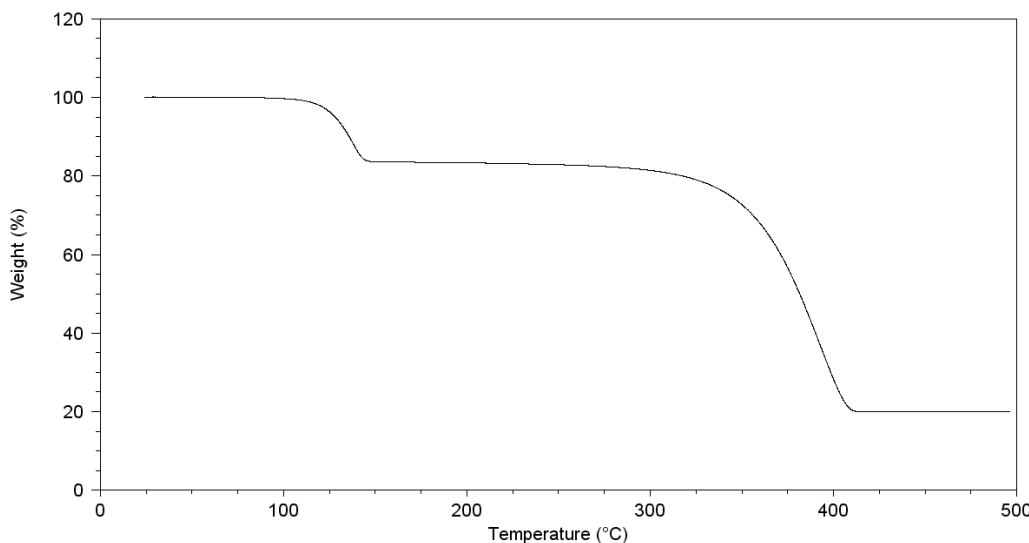


**Figure 3.6.** TGA of **9**.

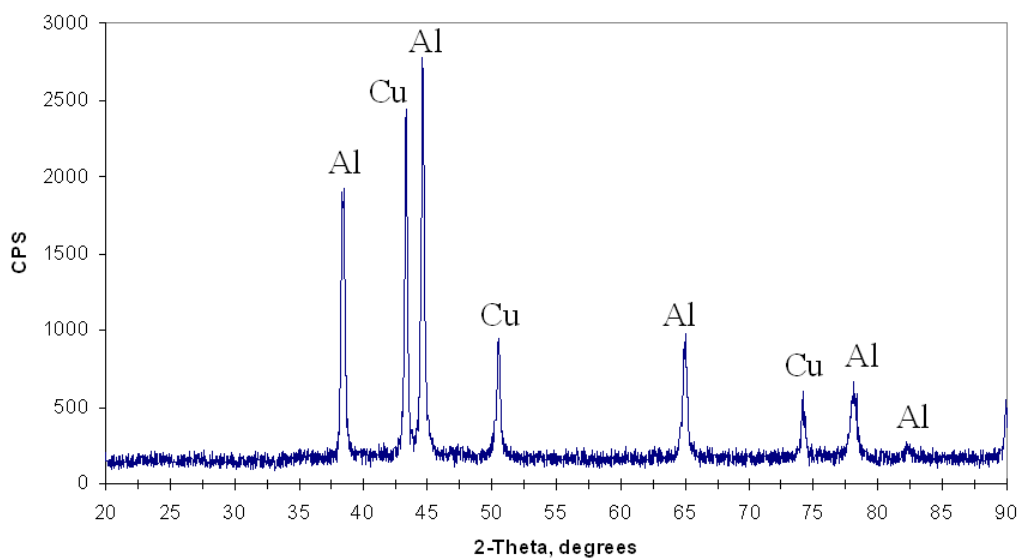


**Figure 3.7.** Powder X-ray diffraction pattern of the TGA residue of **9**.

Using the same starting material as **9**, the phenanthroline concentration was increased. Compound **10** was formed as the result of a 1:10 ratio of Cu(I) to phen. The asymmetric unit of **10** contains one unique Cu(I) center coordinated to two

phenanthroline ligands, one MeCN molecule, and one distorted THF molecule, forming a distorted tetrahedral geometry as shown in Figure 3.8. Selected bond lengths and angles are listed in Table 3.3. The THF is disordered over a center of symmetry, and the carbon-oxygen bonds are bent. The THF is bonded to one Cu(I) half the time, and bonded to a neighboring Cu(I) center the other half of the time.

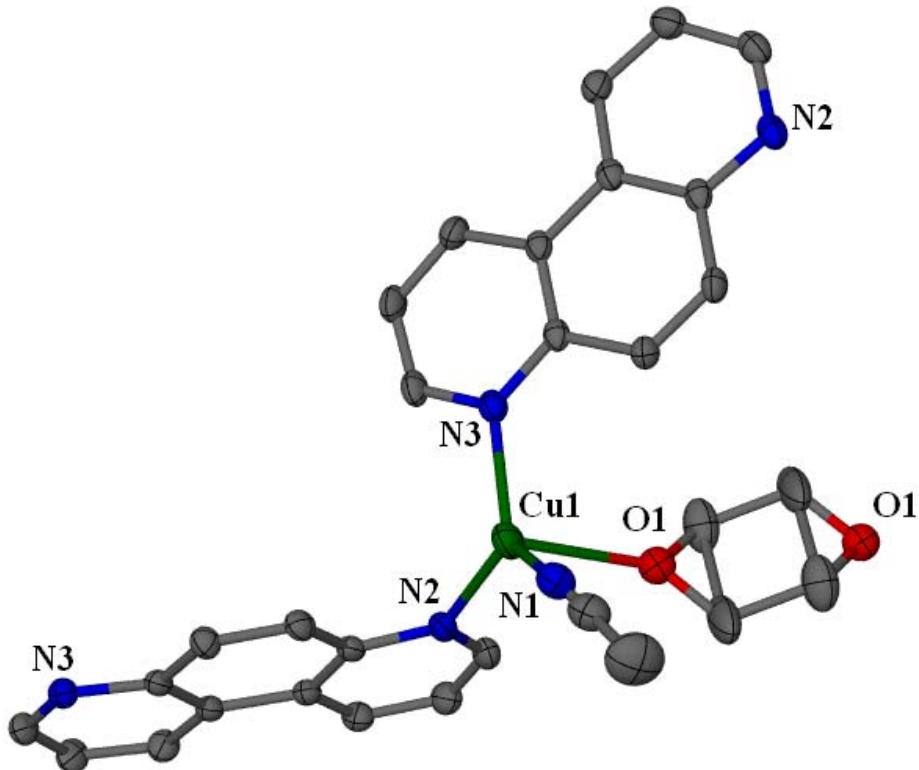


**Figure 3.8.** Coordination environment of the unique Cu(I) center in **10**.

All atoms shown as 50% probability thermal ellipsoids.

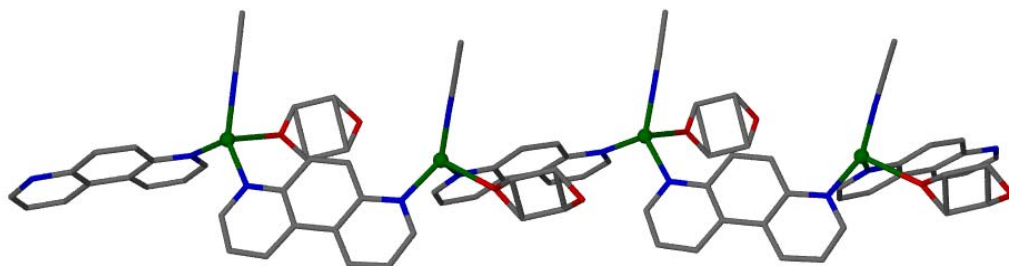
Hydrogen atoms have been omitted for clarity. Colors as

listed previously; oxygen is shown in red.

| Bond Lengths ( $\text{\AA}$ ) | Bond Angles (deg)              |
|-------------------------------|--------------------------------|
| Cu(1) – O(1): 2.416(4)        | O(1) – Cu(1) – N(1): 91.77(2)  |
| Cu(1) – N(1): 1.911(3)        | O(1) – Cu(1) – N(2): 93.40(2)  |
| Cu(1) – N(2): 2.039(2)        | O(1) – Cu(1) – N(3): 96.83(2)  |
| Cu(1) – N(3): 2.022(2)        | N(1) – Cu(1) – N(2): 123.47(1) |
|                               | N(1) – Cu(1) – N(3): 124.05(1) |
|                               | N(2) – Cu(1) – N(3): 111.08(9) |

**Table 3.3.** Selected bond lengths and bond angles in **10**.

The chains that are formed in **10** are reminiscent of the chains seen in **9**, except one of the coordinated MeCNs is replaced by the half-occupied THF molecule (Figure 3.9). The packing of the chains in **10** is also governed by the  $\pi - \pi$  stacking of phenyl groups on neighboring chains, as was also seen in **9**. Figure 3.10 demonstrates the  $\pi - \pi$  interactions between phenyl groups on neighboring chains in **10**. The packing of the chains within the unit cell looking down the  $a$ -axis is shown in Figure 3.11.

**Figure 3.9.** Chains formed in **10**.

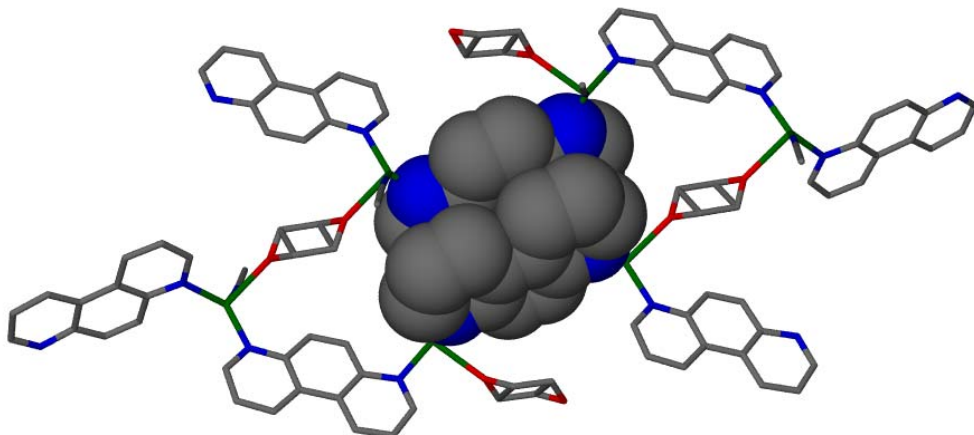


**Figure 3.10.** Space-fill view of the  $\pi - \pi$  stacking between neighboring phenens in **10**.

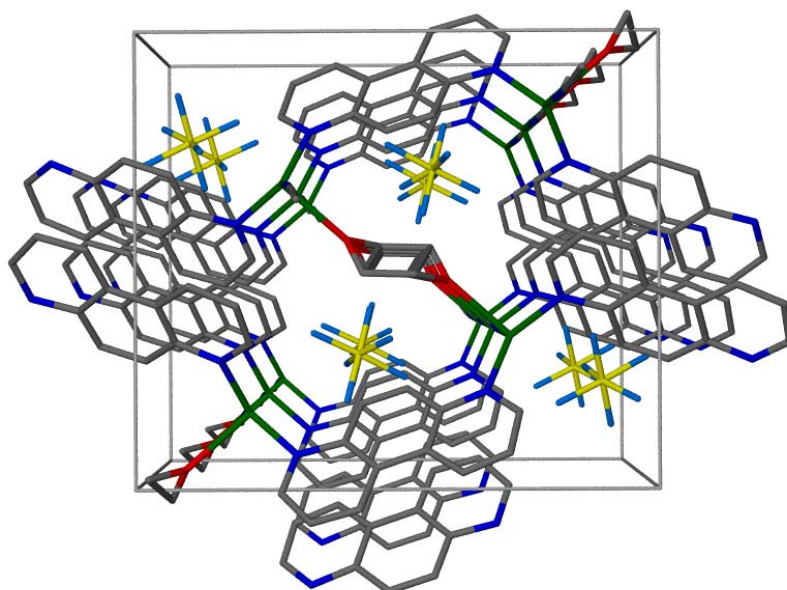


**Figure 3.11.** Packing diagram of the chains in **10** viewed down the *a*-axis.

Thermogravimetric analysis of **10** shows two distinct weight losses, which can be seen in Figure 3.12. Although PXRD was not performed on the residue of **10**, it is

### Chapter 3

assumed to be the same as that of **9**, since both compounds contain Cu(I). However, the calculated weight % of the Cu residue and the observed value do not match (21.72 % observed, 13.64 % calculated). Since the calculated and observed values for the weight % of the residue do not match, the % weight loss values for the rest of the material cannot be calculated accurately. However, it is likely that the first weight loss corresponds to the loss of the MeCN and 0.5 THF molecules (12.62 % observed, 16.55 % calculated) and the second weight loss corresponds to the loss of the phenanthroline ligand and the  $\text{PF}_6^-$  anion (65.15 % observed, 69.81 % calculated). It is not known at this time why the calculated and observed weight % values of the residue do not match. Further experiments need to be performed to solve this problem.

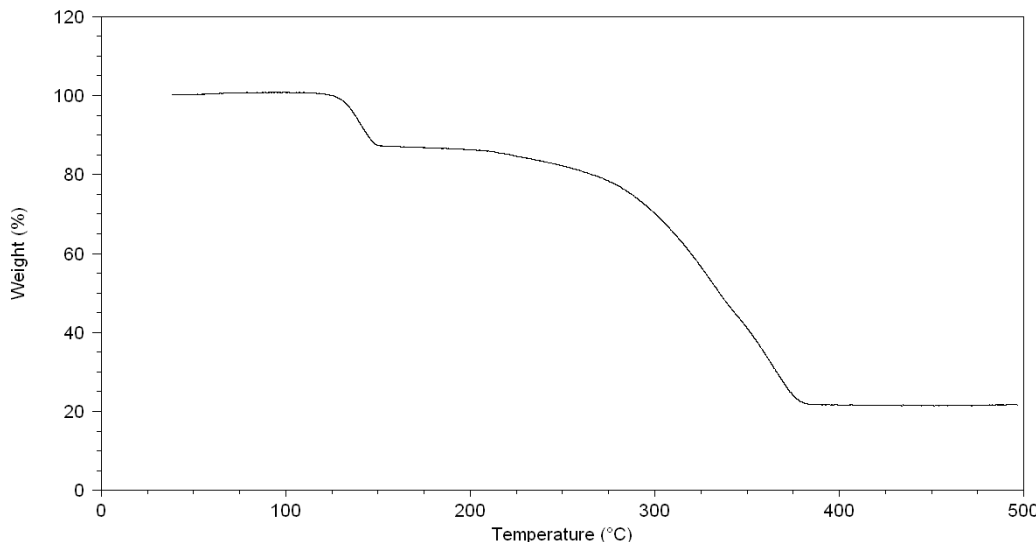


**Figure 3.12.** TGA of **10**.

The next experiments conducted were done under the same conditions used in **9** and **10** except with the benzonitrile- $\text{PF}_6^-$  based starting material. The 1:1 ratio of Cu(I) to

phen was previously reported by Lopez,<sup>4</sup> but a synthesis using a higher concentration of phen had not been done to my knowledge. Compound **11** was formed from the 1:10 ratio of **4** to phen. The asymmetric unit of **11** contains two unique Cu(I) centers, each of which is coordinated to three phens, resulting in a distorted Y-shaped geometry, as shown in Figure 3.13. Selected bond lengths and angles are listed in Table 3.4.

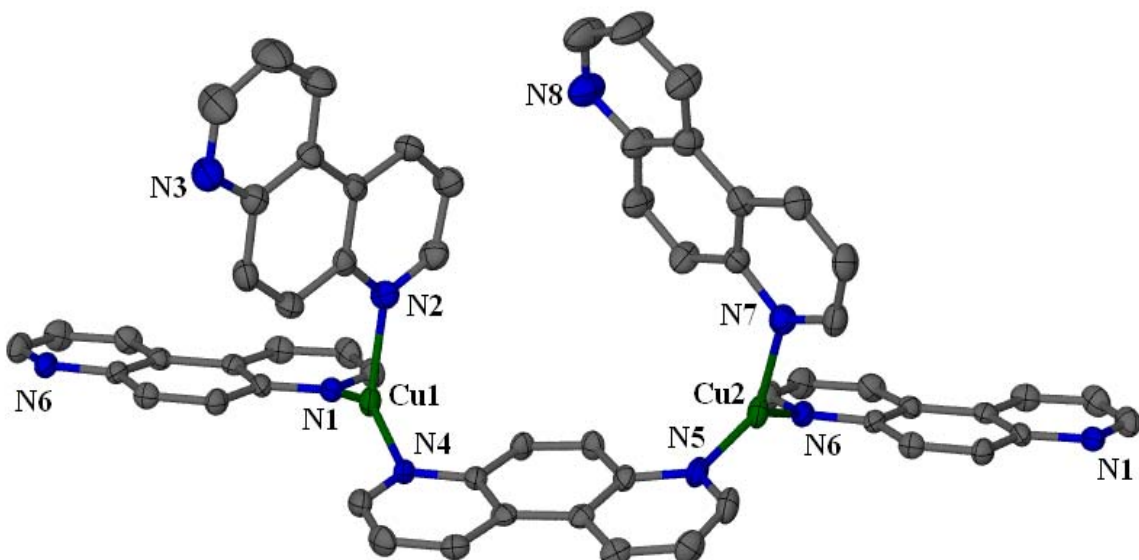


**Figure 3.13.** Coordination environment of the two unique Cu(I) centers in **11**.

All atoms shown as 50% probability thermal ellipsoids. Hydrogen atoms have been omitted for clarity. Colors as listed previously.

| Bond Lengths (Å)       | Bond Angles (deg)              |
|------------------------|--------------------------------|
| Cu(1) – N(1): 1.955(4) | N(1) – Cu(1) – N(2): 104.80(2) |
| Cu(1) – N(2): 2.068(4) | N(2) – Cu(1) – N(4): 109.47(2) |
| Cu(1) – N(4): 1.946(4) | N(1) – Cu(1) – N(4): 145.64(2) |
| Cu(2) – N(5): 1.963(4) | N(5) – Cu(2) – N(6): 141.94(2) |
| Cu(2) – N(6): 1.951(4) | N(5) – Cu(2) – N(7): 103.30(2) |
| Cu(2) – N(7): 2.073(4) | N(6) – Cu(2) – N(7): 114.62(2) |

**Table 3.4.** Selected bond lengths and angles in **11**.

The chains that are formed in **11** are shown in Figure 3.14. Two of the phenyl groups on each Cu(I) center bridge to other Cu(I) centers while one phenyl group does not. Like the previous structures described,  $\pi - \pi$  interactions dominate the packing of the chains in the structure. Also included in the structure are two nitrobenzene molecules, one of which is disordered to two orientations over a center of symmetry. The disordered nitrobenzene resides in a small cavity surrounded by four phenyl groups, while the other nitrobenzene sits in a larger opening in the structure and  $\pi - \pi$  stacks with another nitrobenzene. This is shown in Figure 3.15. The chains also stack on top of one another via  $\pi - \pi$  stacking between the phenyl groups of neighboring chains, as is shown in Figure 3.16. Figure 3.17 shows the packing of the chains within the unit cell looking down the *a*-axis.

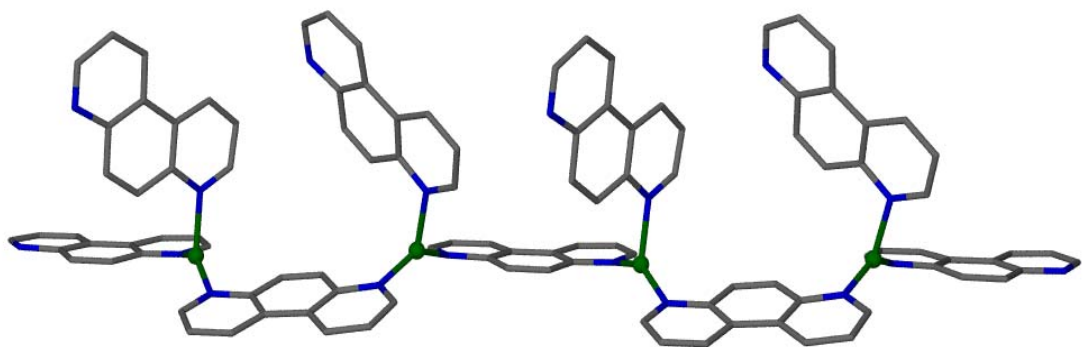


**Figure 3.14.** Chains formed in **11**.

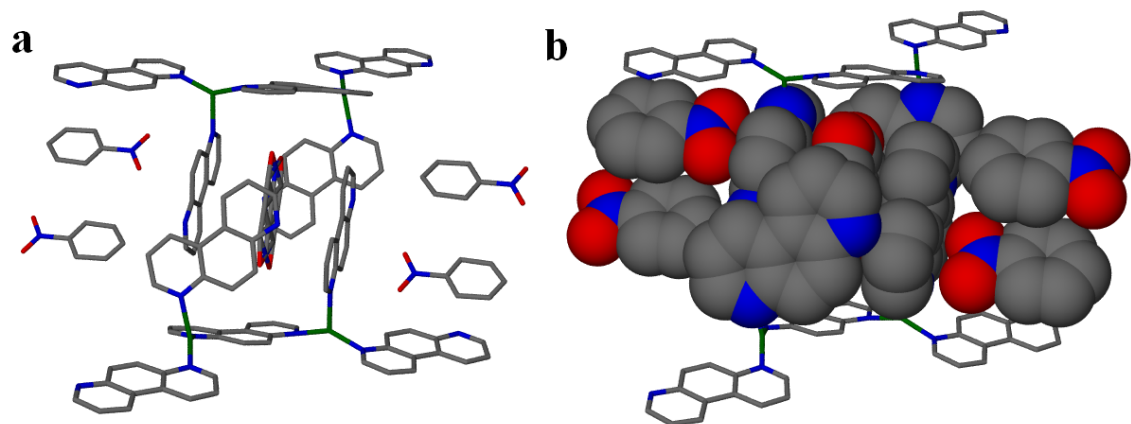


**Figure 3.15.** Stick view of the disordered nitrobenzene in the phen cavity and nitrobenzenes outside the cavity (a) vs. space-fill view of the same picture showing the  $\pi - \pi$  interactions between the nitrobenzenes and phen (b).

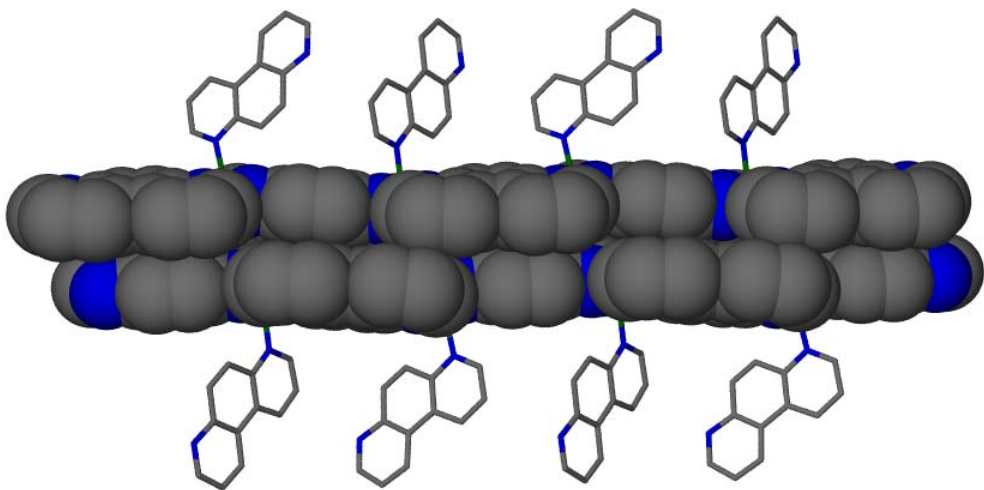


**Figure 3.16.** Space-fill view of the  $\pi - \pi$  stacking of phens on neighboring chains in **11**.

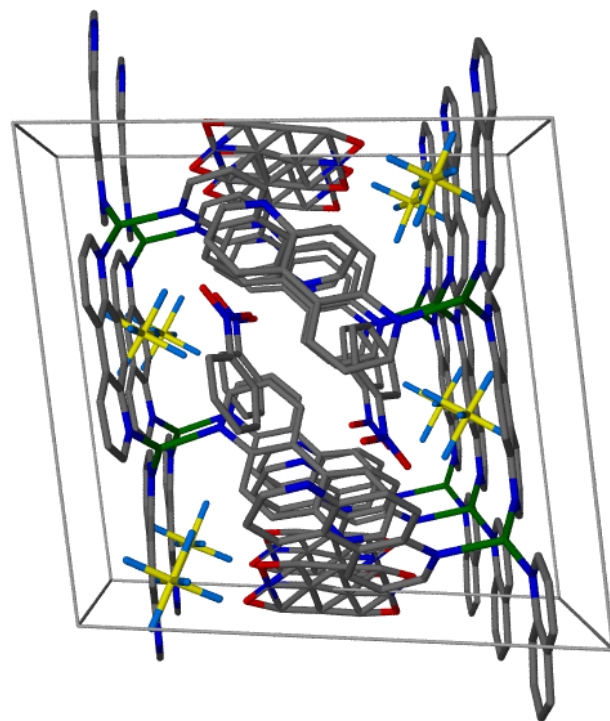


**Figure 3.17.** Packing diagram of the chains in **11** viewed down the *a*-axis.

### Chapter 3

Thermogravimetric analysis of **11** shows three distinct weight losses, which can be seen in Figure 3.18. Although PXRD was not performed on the residue of **11**, it is assumed to be the same as that of **9**, since both compounds contain Cu(I). However, the calculated weight % of the Cu residue and the observed value do not match (14.52 % observed, 9.61 % calculated). Since the calculated and observed values for the weight % of the residue do not match, the % weight loss values for the rest of the material cannot be calculated accurately. However, it is likely that the first weight loss corresponds to the loss of the 1.5 PhNO<sub>2</sub> molecules (12.90 % observed, 13.96 % calculated), the second weight loss corresponds to the loss of the two PF<sub>6</sub><sup>-</sup> anions (22.52 % observed, 21.92 % calculated), and the third weight loss corresponds to the loss of the four phenanthroline ligands (51.19 % observed, 54.50 % calculated). It is not known at this time why the calculated and observed weight % values of the residue do not match. Further experiments need to be performed to solve this problem.

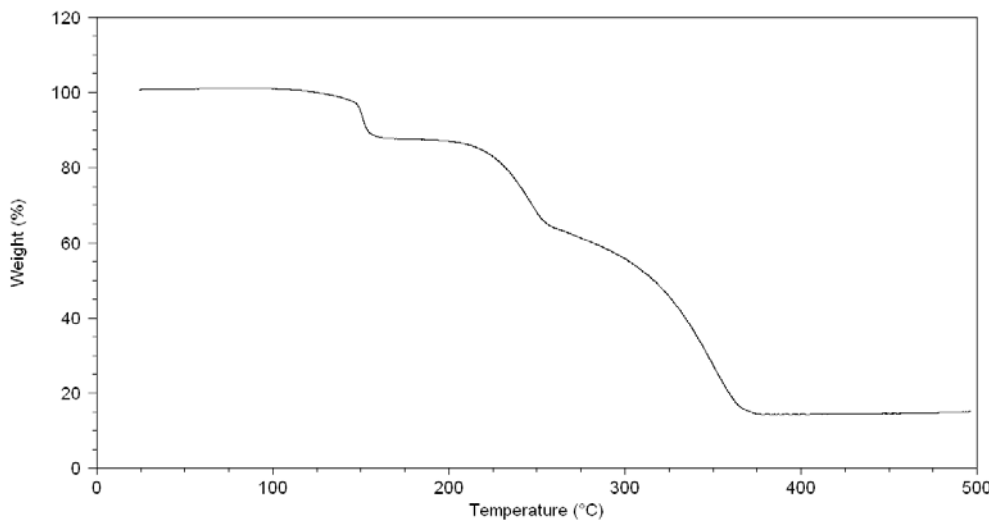


**Figure 3.18.** TGA of **11**.

### Chapter 3

To summarize **9 – 11**, compound **9** is different from its MeCN analog in that it contains one extra MeCN coordinated to the Cu(I) center, yet both structures form one-dimensional chains as was reported by Lopez.<sup>4</sup> So in this case of a 1:1 ratio of **1** or **3** to phen, we see the more common four-coordinate geometry with  $\text{PF}_6^-$  as the counteranion, and the less common three-coordinate geometry with  $\text{BF}_4^-$  as the counteranion. When we increase the ratio to 1:10 of **3** to phen, we see one of the MeCN ligands replaced by a THF. This result is a little surprising, as I would expect that in the presence of excess phen all the MeCN ligands would be replaced by phen, resulting in a three-coordinate Cu(I) center. We do see this phenomenon, however, when **4** is reacted with phen in a 1:10 ratio to form **10**. The compound that results from a 1:1 ratio of **4** to phen,  $[\text{Cu}_2(\text{phen})_4(\text{PhCN})_2][\text{PF}_6]_2$ , was also reported by Lopez, and contains two unique Cu(I) centers, one of which is coordinated to two phen and two PhCN molecules, resulting in a distorted tetrahedral geometry, and the other coordinated to only two phen, resulting in a linear geometry. But in the presence of excess phen, phen replaces the PhCN solvent molecules, and the result is **11**. Perhaps it is the bulkiness of the PhCN solvent molecules that keep them from coordinating with the Cu(I) once the phen ligands have coordinated to form the distorted trigonal geometry. The MeCN solvent molecules are smaller, and therefore it might be easier for them to travel through the network to get to the Cu(I) center and coordinate.

Compound **12** is formed from the 1:1 ratio of **7** or **8** to phen. The asymmetric unit of **12** contains one unique Cu(I) center coordinated to one  $\text{PPh}_3$  and two phen, resulting in a distorted trigonal geometry, as shown in Figure 3.19. Selected bond lengths and angles for **12** (from the **12** from **8** structure) are listed in Table 3.5.

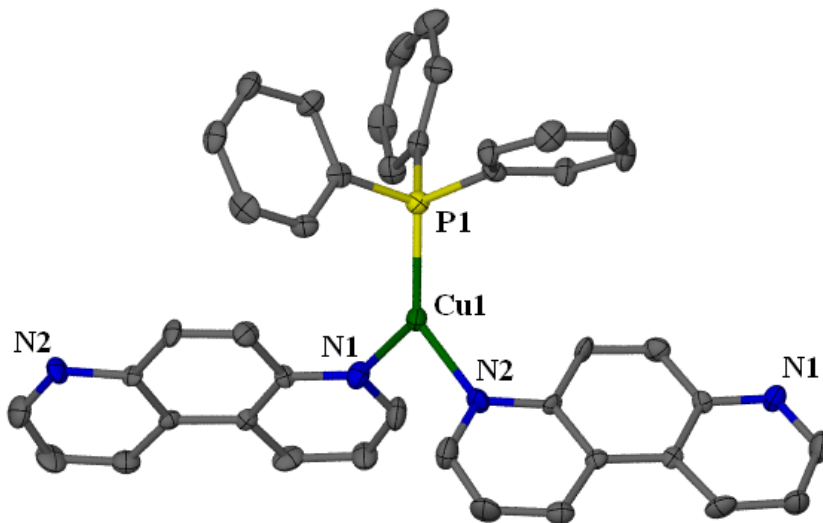


**Figure 3.19.** Coordination environment of the unique Cu(I) center in **12**. All atoms shown as 50% probability thermal ellipsoids. Hydrogen atoms omitted for clarity. Colors as listed previously; phosphorous is shown in yellow.

| Bond Lengths (Å)       | Bond Angles (deg)              |
|------------------------|--------------------------------|
| Cu(1) – P(1): 2.205(1) | P(1) – Cu(1) – N(1): 128.92(9) |
| Cu(1) – N(1): 2.038(3) | P(1) – Cu(1) – N(2): 130.72(8) |
| Cu(1) – N(2): 2.036(3) | N(1) – Cu(1) – N(2): 100.28(2) |

**Table 3.5.** Selected bond lengths and angles in **12** (from **8**).

The phens bridge the Cu(I) centers together to form one-dimensional chains, as shown in Figure 3.20. The both phens on each Cu(I) center are sandwiched by nitrobenzene molecules. Figure 3.21 shows the  $\pi - \pi$  interactions between the phens and

nitrobenzene molecules. The packing of the chains within the unit cell is shown in Figure 3.22.

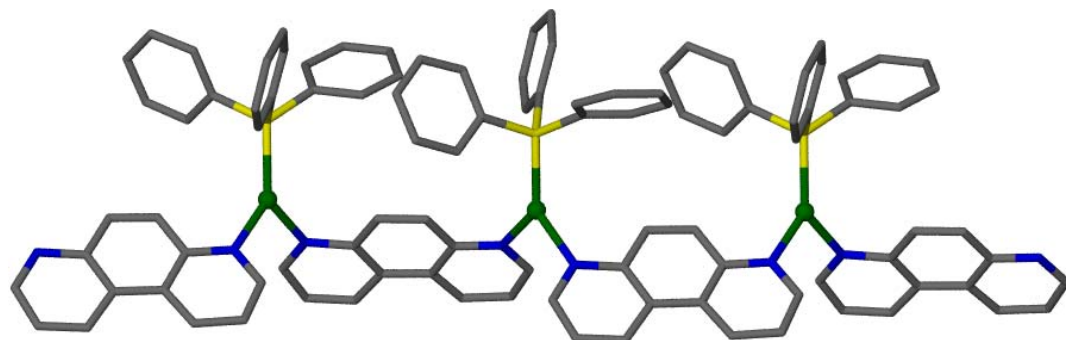


**Figure 3.20.** Chains formed in **12**.

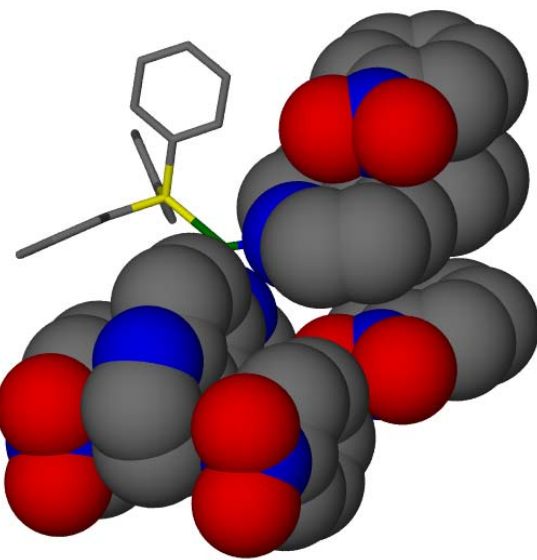


**Figure 3.21.** Space-fill view of the  $\pi - \pi$  stacking between the nitrobenzenes and phens in **12**.

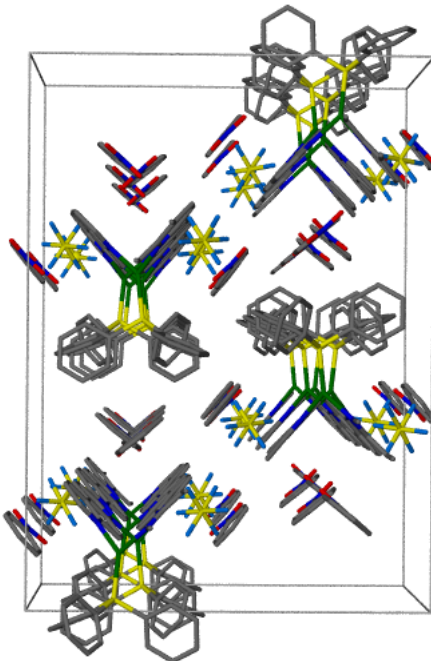


**Figure 3.22.** Packing diagram of the chains in **12** viewed down the *b*-axis.

Thermogravimetric analysis of **12** shows two distinct weight losses (Figure 3.23).

Although PXRD was not performed on the residue of **12**, it is assumed to be the same as that of **9**, since both compounds contain Cu(I). However, the calculated weight % of the Cu residue and the observed value do not match (13.38 % observed, 7.08 % calculated).

Since the calculated and observed values for the weight % of the residue do not match, the % weight loss values for the rest of the material cannot be calculated accurately.

However, it is likely that the first weight loss corresponds to the loss of the two PhNO<sub>2</sub> molecules (24.44 % observed, 27.44 % calculated), and the second weight loss corresponds to the loss of the PPh<sub>3</sub> and phenanthroline ligands and the PF<sub>6</sub><sup>-</sup> anion (62.13 % observed, 65.48 % calculated). It is not known at this time why the calculated

and observed weight % values of the residue do not match. Further experiments need to be performed to solve this problem.

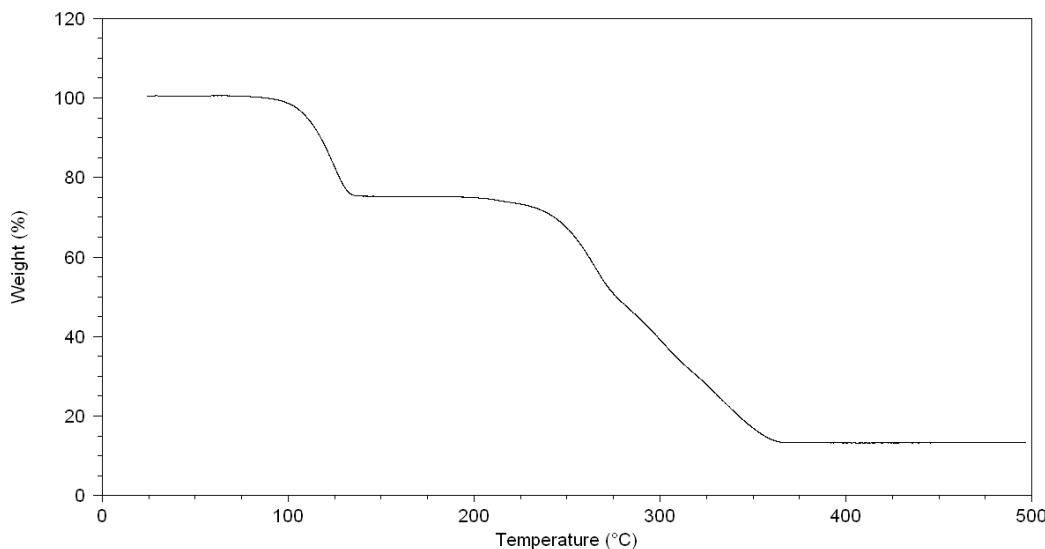


**Figure 3.23.** TGA of **12**.

The main difference in the synthesis of **12** and the previously reported  $[\text{Cu}_3(\text{phen})_4(\text{PPh}_3)][\text{BF}_4]_3$  structure<sup>19</sup> is the use of the different counteranions  $\text{PF}_6^-$  and  $\text{BF}_4^-$ , respectively. It is worth noting that  $[\text{Cu}_3(\text{phen})_4(\text{PPh}_3)][\text{BF}_4]_3$  has been synthesized using both diethyl ether and THF, and the reported syntheses use 1 mL nitrobenzene with 3 mL THF, and 3 mL nitrobenzene with 3 mL ether.<sup>19</sup> Compound **12** was synthesized using 1 mL nitrobenzene with 3 mL ether. Because this change in volume of nitrobenzene between the THF and ether for the previously reported  $[\text{Cu}_3(\text{phen})_4(\text{PPh}_3)][\text{BF}_4]_3$  still resulted in analogous structures, it is unlikely that this difference in **12** and the previously reported  $[\text{Cu}_3(\text{phen})_4(\text{PPh}_3)][\text{BF}_4]_3 \cdot \text{Et}_2\text{O}$  has any

effect on the structural changes observed. Interestingly, no ether is incorporated into the structure of **12**.

It is intriguing that changing the anion would have such a profound effect on the structure. In the previously reported  $[\text{Cu}_3(\text{phen})_4(\text{PPh}_3)][\text{BF}_4]_3$  structure we see three unique Cu(I) centers, one coordinated to two phen and one PPh<sub>3</sub>, and the other two Cu(I) centers coordinated to three phen each, while in **12** we only see one unique Cu(I) center, coordinated to two phen and one PPh<sub>3</sub>. The previously reported  $[\text{Cu}_3(\text{phen})_4(\text{PPh}_3)][\text{BF}_4]_3$ , because it has three unique Cu(I) centers, forms triangular units that are bridged together by phen, while **12** is unable to form triangular units with its one unique Cu(I) center. It is not surprising that changing the starting material from **5** to **6** in the case of BF<sub>4</sub><sup>-</sup> or from **7** to **8** in the case of PF<sub>6</sub><sup>-</sup> has no effect on the structure, since no solvent (MeCN or PhCN) appears in either structure.

### 3.4 Conclusion

Perhaps the most intriguing result of this work is the fact that when we increase the ratio of Cu(I) to phen from 1:1 to 1:10, when MeCN is the solvent, the phen do not replace all of the coordinated solvent molecules, whereas when PhCN is the solvent, phen do replace all of the coordinated solvent molecules. This may be attributed to the different sizes of the MeCN and PhCN, which might affect their competition with phen to coordinate with the Cu(I) center. When PPh<sub>3</sub> is added to the starting material, we don't see any solvent in the structures, so it is not surprising that using MeCN or PhCN results in identical structures. There is quite a difference, however, between the structures formed from changing the counteranion from BF<sub>4</sub><sup>-</sup> to PF<sub>6</sub><sup>-</sup>.

### 3.5 References

1. Keller, S. W., An Acentric, Three-Dimensional Coordination Polymer: Synthesis and Structure of  $[\text{Cu}(\text{pyrimidine})_2]\text{BF}_4$ . *Angew. Chem. Int. Ed. Engl.* **1997**, 36, (3), 247-248.
2. Lopez, S.; Kahraman, M.; Harmata, M.; Keller, S. W., Novel 2-fold Interpenetrating Diamondoid Coordination Polymers:  $[\text{Cu}(3,3'\text{-bipyridine})_2]\text{X}$  ( $\text{X} = \text{BF}_4^-$ ,  $\text{PF}_6^-$ ). *Inorg. Chem.* **1997**, 36, 6138-6140.
3. Keller, S. W.; Lopez, S., A two-dimensional geomimetic coordination polymer containing pentagonal cavities. *J. Am. Chem. Soc.* **1999**, 121, (26), 6306-6307.
4. Lopez, S.; Keller, S. W., New linear coordination polymers based on copper(I) and 4,7-phenanthroline: Structure dependence on solvent and counteranion. *Inorg. Chem.* **1999**, 38, (8), 1883-1888.
5. Knaust, J. M.; Inman, C.; Keller, S. W., A host-guest complex between a metal-organic cyclotrimerateylene analog and a polyoxometalate:  $[\text{Cu}_6(4,7\text{-phenanthroline})_8(\text{MeCN})_4]2\text{PM}_{12}\text{O}_{40}$  ( $\text{M} = \text{Mo or W}$ ). *Chem. Commun.* **2004**, (5), 492-493.
6. Steed, J. W.; Atwood, J. L., *Supramolecular chemistry*. Wiley: Chichester ; New York, 2000; 745 p.
7. Eddaoudi, M.; Kim, J.; Rosi, N.; Vodak, D.; Wachter, J.; O'Keeffe, M.; Yaghi, O. M., Systematic design of pore size and functionality in isoreticular MOFs and their application in methane storage. *Science* **2002**, 295, (5554), 469-472.
8. Eddaoudi, M.; Moler, D. B.; Li, H. L.; Chen, B. L.; Reineke, T. M.; O'Keeffe, M.; Yaghi, O. M., Modular chemistry: Secondary building units as a basis for the design of highly porous and robust metal-organic carboxylate frameworks. *Acc. Chem. Res.* **2001**, 34, (4), 319-330.
9. Yaghi, O. M.; Li, G. M.; Li, H. L., Selective Binding and Removal of Guests in a Microporous Metal-Organic Framework. *Nature* **1995**, 378, (6558), 703-706.

### Chapter 3

10. Zaworotko, M. J., Crystal Engineering of Diamondoid Networks. *Chem. Soc. Rev.* **1994**, 23, (4), 283-288.
11. Moulton, B.; Zaworotko, M. J., From molecules to crystal engineering: Supramolecular isomerism and polymorphism in network solids. *Chem. Rev.* **2001**, 101, (6), 1629-1658.
12. Subramanian, S.; Zaworotko, M. J., Porous Solids by Design - [Zn(4,4'-Bpy)<sub>2</sub>(Sif<sub>6</sub>)](N) · Xdmf, a Single Framework Octahedral Coordination Polymer with Large Square Channels. (1995). *Angew. Chem. Inter. Ed. Engl.* **1995**, 34, (22), 2561-2561.
13. Kubas, G. J., Tetrakis(acetonitrile)copper(I) hexafluorophosphate. *Inorg. Syn.* **1979**, 19, 90-92.
14. Knaust, J. M.; Knight, D. A.; Keller, S. W., Crystal and molecular structures of several tetrakis (nitrile) copper(I) complexes. *J. Chem. Cryst.* **2003**, 33, (11), 813-823.
15. *SADABS*, Bruker Analytical X-ray: 1997.
16. Sheldrick, G. M. *SHELXS-97: Program for Structure Solution*, University of Gottingen, Germany: 1997.
17. Barbour, L. *X-Seed: Graphical Interface for SHELXL*, University of Missouri-Columbia: 2001.
18. Wyckoff, R. W. G., *Crystal structures*. 2d ed.; Interscience Publishers: New York,, 1963; p v.
19. Knaust, J. M.; Lopez, S.; Inman, C.; Keller, S. W., Linking triangles: synthesis and struture of [Cu<sub>3</sub>(phen)<sub>4</sub>(PPh<sub>3</sub>)](BF<sub>4</sub>)<sub>3</sub> · X and [Cu<sub>5</sub>-(phen)<sub>7</sub>](BF<sub>4</sub>)<sub>5</sub> · 4(NO<sub>2</sub>C<sub>6</sub>H<sub>5</sub>) (phen=4,7-phenanthroline and X = Et<sub>2</sub>O or 2 THF). *Polyhedron* **2003**, 22, (22), 3015-3024.

## Chapter 4

# Novel Mixed Valent Copper(I)/Copper(II) and Copper(II) Coordination Polymers

### 4.1 Introduction

Although the Keller group has been studying Cu(I) coordination polymers for more than 10 years, little work has been done in the group to study the oxidation of Cu(I) to Cu(II) in these compounds. In 1997, Novak and Keller observed the air oxidation of a solution containing  $[\text{Cu}(\text{MeCN})_4]\text{BF}_4$  and excess pyrimidine in nitrobenzene due to the formation of blue crystals of  $[\text{Cu}(\text{pyrimidine})_4]2\text{BF}_4^-$ . The structure of this compound contains a Cu(II) with distorted octahedral geometry that is coordinated to  $\text{BF}_4^-$  anions in the axial positions and non-bridging pyrimidines in the equatorial positions.<sup>1</sup> Generally, most of the crystals of Cu(I) coordination polymers that we observe are yellow in color.

A few years later, Doug Knight observed some unexpected green crystals in one of his vials containing a 1:1 ratio of  $[\text{Cu}(\text{MeCN})_4]\text{BF}_4$  to pyrimidine in acetonitrile and nitrobenzene. Upon collection and analysis of X-ray crystallographic data, it was discovered that the structure of these green crystals was a dimer that contained both Cu(I) and Cu(II) centers (Figure 4.1).<sup>2</sup> The only explanation Doug had for the finding of the unique structure was that one of the solvent bottles had been left open and exposed to air,

and although serendipitous results are wonderful, it was imperative to find the exact concentration of O<sub>2</sub> that would allow synthesis of the mixed-valent dimer reproducibly.

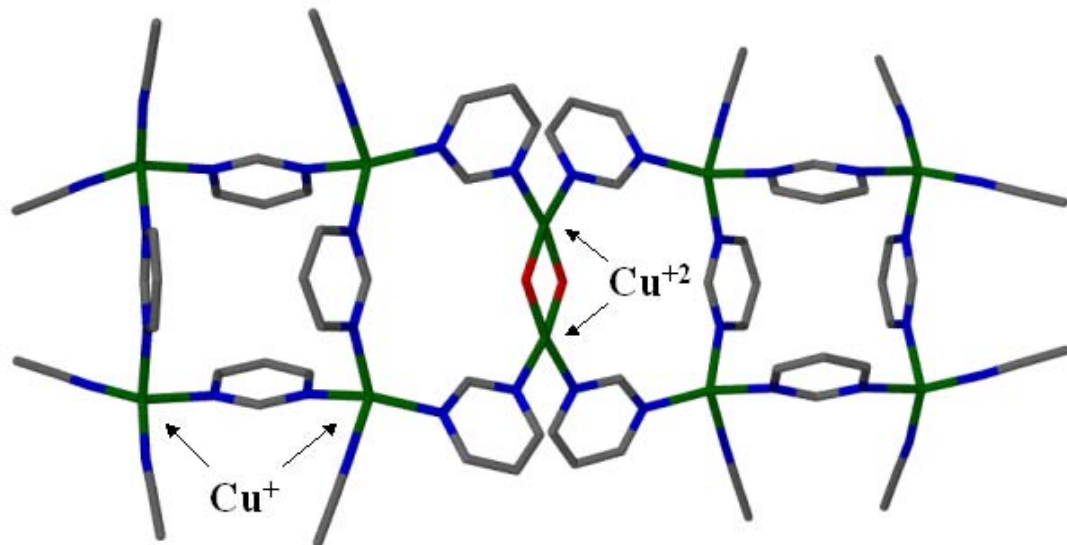


**Figure 4.1.** Doug's mixed valent complex,

[Cu<sub>9</sub>(pyrimidine)<sub>10</sub>(MeCN)<sub>12</sub>(OH)](BF<sub>4</sub>)<sub>9</sub>, **13**. The Cu(I)-

containing squares are connected by two Cu(II) centers.

Copper = green, carbon = gray, nitrogen = blue, oxygen = red.

Hydrogen atoms and BF<sub>4</sub><sup>-</sup> anions omitted for clarity.

The observation of mixed-valent copper complexes is surprisingly not all that uncommon. Mixed-valent Cu(I)/Cu(II) complexes have been reported in the literature as early as 1958,<sup>3,4</sup> and reports of polymeric structures containing mixed-valent copper centers date back to as early as 1980.<sup>5</sup> Mixed-valent coordination polymers have gained more interest in recent years,<sup>6,7</sup> as have Cu(II) coordination polymers.<sup>8-10</sup>

In experimenting with the concentration of O<sub>2</sub> in solution, a new Cu(II) complex was discovered using the same synthesis of the mixed-valent complex. Similar experiments were performed using [Cu(MeCN)<sub>4</sub>]PF<sub>6</sub> as the starting material. Two other compounds were formed, one containing only Cu(I) centers and the other containing only Cu(II) centers. The structural details of these compounds are described here, as well as future directions and applications for this project.

## 4.2 Experimental

### *Materials and Methods*

Pyrimidine, 4,4'-bipyridine (Aldrich), 4,7-phenanthroline (GFS Chemicals and Aldrich), nitrobenzene (Aldrich), acetonitrile (MeCN), and tetrahydrofuran (THF, Fisher) were used without further purification. Starting materials [Cu(MeCN)<sub>4</sub>]BF<sub>4</sub>, **1** and [Cu(MeCN)<sub>4</sub>]PF<sub>6</sub>, **3** were synthesized as previously described in Chapter 3. Thermogravimetric analyses were performed using a TA Instruments Q500 TGA with an N<sub>2</sub> flow rate of 100 mL/min and a heating rate of 10 °C/min.

Ultraviolet-Visible (UV-Vis) spectroscopy was performed using a Hewlett Packard 8453 spectrophotometer equipped with a deuterium lamp (UV) and a tungsten lamp (Vis). Fisherbrand quartz cells having a path length of 1.0 mm and thickened sample walls for small volume samples were used to take measurements. A solution of 0.5 mL MeCN and 0.5 mL nitrobenzene was used as a blank. Samples of solutions treated with Ar, 1 min O<sub>2</sub>, 2 min O<sub>2</sub>, 3 min O<sub>2</sub>, 4 min O<sub>2</sub> and 5 min O<sub>2</sub> (flow rate of O<sub>2</sub> = 100 mL/min) were made and left for five days before running UV-Vis measurements to allow oxidation to occur. Each sample was filtered through a small Pasteur pipet

## Chapter 4

containing a small piece of cotton to remove any solid particles present before measurement.

### *Synthesis*

#### **[Cu<sub>9</sub>(pyrimidine)<sub>10</sub>(MeCN)<sub>12</sub>(OH)](BF<sub>4</sub>)<sub>9</sub>, 13**

In a 1-dram vial, **1** (0.040 g, 0.13 mmol) was dissolved in 0.5 mL MeCN and 0.5 mL nitrobenzene. Pyrimidine (0.10 g, 1.3 mmol) was then added to the solution. The 1-dram vial was placed in a 20-dram vial containing 4 mL THF. The 20-dram vial was capped with a septum, and the solution, THF, and atmosphere were saturated with Ar to remove any oxygen present. Oxygen gas (flow rate = 100 mL/min) was then bubbled into the solution for 1 minute, then into the THF in the outer vial for 1.5 min. Dark green blocky crystals of **13** were observed, along with yellow crystals of the previously determined [Cu<sub>4</sub>(pyrimidine)<sub>4</sub>(MeCN)<sub>8</sub>](BF<sub>4</sub>)<sub>4</sub>, after several days.

#### **[Cu<sub>2.5</sub>(pyrimidine)<sub>4</sub>(OH)<sub>2</sub>(H<sub>2</sub>O)<sub>2</sub>](BF<sub>4</sub>)<sub>3</sub> · H<sub>2</sub>O, 14**

In a 1-dram vial, **1** (0.040 g, 0.13 mmol) was dissolved in 0.5 mL MeCN and 0.5 mL nitrobenzene. Pyrimidine (0.10 g, 1.3 mmol) was added to the solution. The 1-dram vial was placed in a 20-dram vial containing 4 mL THF. The 20-dram vial was capped with a septum, and the solution, THF, and atmosphere were saturated with O<sub>2</sub>. Dark blue blocky crystals of **14** were observed after several days.

## Chapter 4

### [Cu<sub>2.3</sub>(pyrimidine)<sub>3.5</sub>(MeCN)](PF<sub>6</sub>)<sub>2.3</sub>, **15**

In a 1-dram vial, **3** (0.040 g, 0.11 mmol) was dissolved in 0.5 mL MeCN and 0.5 mL nitrobenzene. Pyrimidine (0.10 g, 1.3 mmol) was added to the solution. This vial was capped with a septum, and the solution and atmosphere were flushed with argon. Then O<sub>2</sub> was bubbled directly into the solution at a rate of 10 mL/min for 30 seconds. This solution was allowed to set for five days, after which the septum was removed, and the vial was placed in a 20-dram vial containing 4 mL untreated THF. Yellow blocky crystals of **15** were observed after a couple of days. The crystals of **15** were placed under vacuum for three days to remove excess solvent present in the structure. Crystals of **15** can also be made without adding any oxygen to the solution.

### [Cu(pyrimidine)(OH)(H<sub>2</sub>O)<sub>3</sub>]PF<sub>6</sub> · H<sub>2</sub>O, **16**

In a 1-dram vial, **3** (0.040 g, 0.11 mmol) was dissolved in 0.5 mL O<sub>2</sub>-saturated MeCN and 0.5 mL O<sub>2</sub>-saturated nitrobenzene. Pyrimidine (0.10 g, 1.3 mmol) and deionized water (0.25 g, 14 mmol) were added to the solution. The 1-dram vial was placed in a 20-dram vial containing 4 mL O<sub>2</sub>-saturated THF. The 20-dram vial was capped with a septum, and the entire atmosphere was then saturated with O<sub>2</sub>. Light blue columnar crystals of **16** were observed after several days.

### *Crystal Structure Analysis*

Single crystals, as determined by polarized optical microscopy, were placed in an inert oil and then mounted with silicone grease on a thin glass fiber. Full hemispheres of data were collected using a Siemens SMART system equipped with a CCD area detector

## Chapter 4

( $\text{Mo}(\text{K}_\alpha) = 0.71073 \text{ \AA}$ ), and absorption corrections were applied after integration.<sup>11</sup> All structures were solved using SHELXS Direct Methods,<sup>12</sup> and then refined using a full least squares treatment on  $\text{F}^2$ .<sup>12, 13</sup>

All nonhydrogen atoms were refined with anisotropic thermal parameters unless otherwise noted. All hydrogen atom positions were calculated. Crystallographic details for **14 – 16** are listed in Table 4.1. The crystallographic details of **13** were published previously.<sup>2</sup>

Two of the  $\text{BF}_4^-$  anions in **14** were found to be disordered. Four of the fluorine atoms were split into parts F2, F2A, F4, F4A, F11, F11A, F12, and F12A and assigned site occupancies of 0.7, 0.3, 0.7, 0.3, 0.8, 0.2, 0.7, and 0.3, respectively. Fractional site occupancies were assigned based on the thermal parameter of each atom,  $U_{\text{iso}}$ . Atoms F2A, F4A, F11A, and F12A were refined with isotropic thermal parameters. Atoms H17, H18, H19, H20, H21, H22, H23, and H24 were refined to fixed positions by setting AFIX = 1. Small amounts of residual electron density remain around the Cu(II) centers, pyrimidines, and anions.

Atoms Cu3 and P3 in **15** occupy special positions, and each has a site occupancy of 0.3. This means they both reside on a 3-fold rotation axis. Two of the  $\text{PF}_6^-$  anions in **15** were found to be disordered. Four of the fluorine atoms were split into parts F4, F4A, F6, F6A, F7, F7A, F9, and F9A and assigned site occupancies of 0.7, 0.3, 0.7, 0.3, 0.7, 0.3, 0.5, and 0.5, respectively. Fractional site occupancies were assigned based on the thermal parameter of each atom,  $U_{\text{iso}}$ . Atoms F4A and F6A were refined with isotropic thermal parameters. Small amounts of residual electron density remain around the Cu(I) centers and anions.

## Chapter 4

The two  $\text{PF}_6^-$  anions present in the asymmetric unit of **16** occupy special positions (P1 and P2 both sit on a mirror plane), and therefore P1 and P2 each have site occupancies of 0.5. There are three unique fluorine atoms bonded to each phosphorous atom, all with site occupancies of 1, which add up to a total of six fluorine atoms. Thus, there is really only a total of one  $\text{PF}_6^-$  anion in the asymmetric unit of **16**. To balance the Cu(II) charge in the asymmetric unit, one of the four oxygen atoms coordinated to Cu1 must belong to a hydroxyl group. Atom O1 was modeled as a hydroxyl group, while atoms O2, O3, and O4 were modeled as waters. Two of the fluorine atoms of the  $\text{PF}_6^-$  anion were found to be disordered, split into parts F4, F4A, F5, and F5A, and were each assigned a site occupancy of 0.5. Fractional site occupancies were assigned based on the thermal parameter of each atom,  $U_{\text{iso}}$ . Atoms H5, H6, H7, H8, H9, H10, H11, H12, and H13 were refined to fixed positions by setting AFIX = 1. Small residual electron density remains around the Cu(II) center, pyrimidines, and anion.

## Chapter 4

**Table 4.1:** Selected crystallographic details for **14–16**.

|   | <b>14</b>   | <b>15</b>  | <b>16</b>  |
|---|---|--|--|
| Empirical formula   | $\text{Cu}_{2.5}\text{C}_{16}\text{H}_{24}\text{N}_8\text{O}_5\text{B}_3$<br>$\text{F}_{12}$                                  | $\text{Cu}_{2.33}\text{C}_{18}\text{H}_{18}\text{N}_9$<br>$\text{P}_{2.33}\text{F}_{13}$ | $\text{CuC}_4\text{H}_{13}\text{N}_2\text{O}_5\text{PF}_6$ |
| Formula weight (g/mol)  | 827.71  | 994.72   | 377.67   |
| Crystal system, space group   | Triclinic, P-1  | Trigonal (Rhombohedral), R-3   | Tetragonal, P4 <sub>1</sub> 2 <sub>1</sub> 2               |
| Temperature (K)   | 173(2)  | 173(2)   | 173(2)   |
| Unit cell dimensions (Å, deg)   | $a = 7.3429(5)$<br>$b = 9.8715(7)$<br>$c = 20.440(2)$<br>$\alpha = 103.802(1)$<br>$\beta = 90.562(1)$<br>$\gamma = 91.441(1)$ | $a = 20.328(7)$<br>$\alpha = 115.429(0)$   | $a = 11.1459(3)$<br>$c = 19.303(1)$                        |
| Volume (Å <sup>3</sup> )  | 1438.16(2)  | 4507.3(3)  | 2398.03(2)   |
| Z, ρ calc (g/cm <sup>3</sup> )  | 2, 1.911  | 6, 1.832   | 8, 2.092   |
| Absorption coefficient (mm <sup>-1</sup> )  | 1.962   | 1.878  | 2.053  |
| F(000)  | 823   | 2458   | 1512   |
| Crystal size (mm)   | 0.3 × 0.2 × 0.1   | 0.3 × 0.25 × 0.1   | 0.5 × 0.1 × 0.1  |
| Θ Range for data collection (deg)   | 2.57 to 26.67   | 2.37 to 25.23  | 2.58 to 27.04  |
| Reflections collected/unique  | 10055 / 6186<br>[R <sub>int</sub> =0.0333]  | 20863 / 5227<br>[R <sub>int</sub> =0.1221]   | 16884 / 2618<br>[R <sub>int</sub> =0.0251]                 |
| Max. and min. transmission  | 0.8280 and 0.5309   | 0.8344 and 0.4892  | 0.8210 and 0.5526  |
| Data / restraints / parameters  | 6186 / 0 / 437  | 5227 / 0 / 429   | 2618 / 0 / 191   |
| Final R indices [I>2σ(I)] <sup>a,b</sup>  | R <sub>1</sub> = 0.0502,<br>wR <sub>2</sub> = 0.1256  | R <sub>1</sub> = 0.0846,<br>wR <sub>2</sub> = 0.1576                                     | R <sub>1</sub> = 0.0227,<br>wR <sub>2</sub> = 0.0662       |
| R indices (all data)  | R <sub>1</sub> = 0.0831,<br>wR <sub>2</sub> = 0.1500  | R <sub>1</sub> = 0.2155,<br>wR <sub>2</sub> = 0.2441                                     | R <sub>1</sub> = 0.0243,<br>wR <sub>2</sub> = 0.0672       |
| Largest diff. peak / hole (e.Å <sup>-3</sup> )  | 0.70 / -0.70  | 0.71 / -1.87   | 0.54 / -0.42   |
| GoF on F <sup>2</sup>   | 0.914   | 0.918  | 1.059  |
| Structures were refined on $F_o^2$ using all data. <sup>a</sup> $R = \Sigma( F_o  -  F_c ) / \Sigma F_o $ ; <sup>b</sup> $wR_2 = [\Sigma( F_o  -  F_c )^2 / \Sigma F_o ^2]^{1/2}$ |   |  |  |

### 4.3 Results and Discussion

During the first attempts to synthesize the mixed valent dimer, each of the solvents (acetonitrile, nitrobenzene, and THF) was saturated with O<sub>2</sub> before making the solutions and then saturated the entire environment of the crystallization setup with O<sub>2</sub> as well. Three different colors of crystals were observed over time. Yellow crystals were observed first, followed by green crystals, and then dark blue crystals. Single crystal X-ray diffraction showed that the yellow crystals were that of [Cu<sub>4</sub>(pyrimidine)<sub>4</sub>(MeCN)<sub>8</sub>](BF<sub>4</sub>)<sub>4</sub>, a Cu(I) structure that has already been solved in our group. The structure of [Cu<sub>4</sub>(pyrimidine)<sub>4</sub>(MeCN)<sub>8</sub>](BF<sub>4</sub>)<sub>4</sub> is a discrete square that contains four Cu(I) centers, each bridged by two pyrimidine ligands and each Cu(I) center is also coordinated to two terminal MeCN ligands (Figure 4.2).

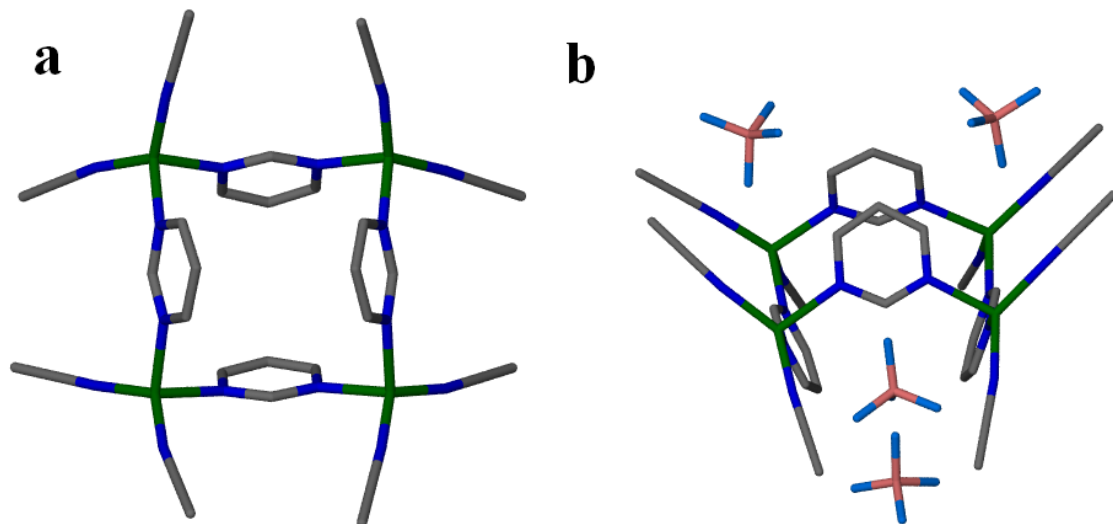


**Figure 4.2.** Structure of [Cu<sub>4</sub>(pyrimidine)<sub>4</sub>(MeCN)<sub>8</sub>](BF<sub>4</sub>)<sub>4</sub>. The BF<sub>4</sub><sup>-</sup> anions and hydrogen atoms have been omitted for clarity in (a), while only the hydrogen atoms have been omitted in (b).

## Chapter 4

The green crystals were the mixed valent dimer, **13**, and the blue crystals were the Cu(II)-containing **14**. Attempts were then made to measure the concentration of O<sub>2</sub> by adding only specific amount of O<sub>2</sub> directly to the [Cu(MeCN)<sub>4</sub>]BF<sub>4</sub>-pyrimidine solution. This was done using a calibrated gas flow meter and a stopwatch. The rate of flow of O<sub>2</sub> was kept at 100 mL/min. Figure 4.3 shows the observed color changes in the solution upon the increased addition of O<sub>2</sub>. From left, the amount of time O<sub>2</sub> was bubbled into each solution at 10 cc/min is as follows: 0 min (Ar atmosphere only), 1 min, 2 min, 3 min, 4 min, and 5 min.

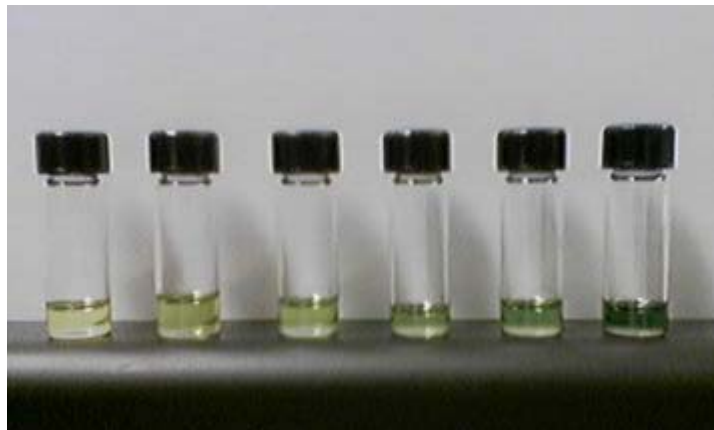


**Figure 4.3.** Observed color changes in the [Cu(MeCN)<sub>4</sub>]BF<sub>4</sub>-pyrimidine solution upon increased addition of O<sub>2</sub>.

UV-Vis Spectroscopy was performed on each of the solutions shown above. Figure 4.4 shows the resulting spectra.

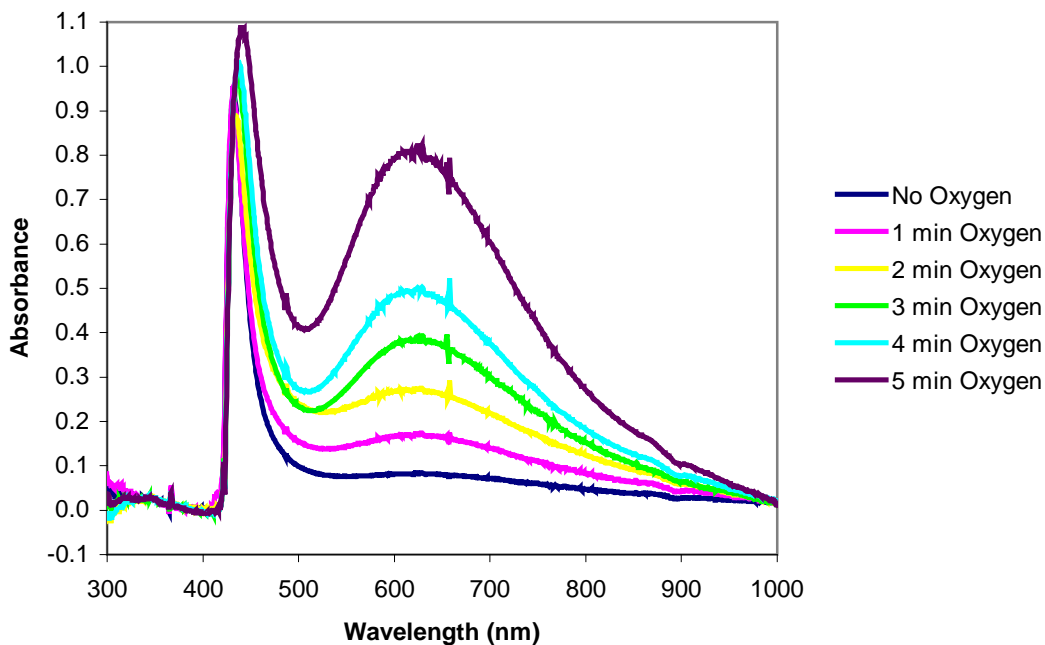


**Figure 4.4.** UV-Vis spectra of solutions of  $[\text{Cu}(\text{MeCN})_4]\text{BF}_4$ -pyrimidine with increasing amounts of oxygen added to different solutions.

A strong peak at  $\sim 450$  nm can be observed in each spectra; this is likely the Cu(I) species  $[\text{Cu}_4(\text{pyrimidine})_4(\text{MeCN})_8](\text{BF}_4)_4$ . As an increased amount of oxygen is added to the solution, a broad peak at  $\sim 650$  nm is observed to increase in size, indicating the increased presence of an oxidized species in solution, likely **13**.

Thermogravimetric analysis of **13** was performed and is shown in Figure 4.5. Powder X-ray diffraction has not been performed on the residue of **13**, but the calculations were performed under the assumption that the Cu(I) and Cu(II) centers are both reduced to Cu. The exact mechanism of reduction is not known at this time. Then charge balance occurs with the anions. The first two weight losses occur at 100 and 150 °C and combined correspond to the loss of 12 MeCN molecules and the hydroxide (19.82 % observed, 19.13 % calculated). The third transition occurs between 150 and

325 °C corresponds to the loss of 10 pyrimidine ligands and 9  $\text{BF}_4^-$  anions (58.18 % observed, 59.40 % calculated). The residue corresponds to 9 Cu atoms (21.90 % observed, 21.47 % calculated).

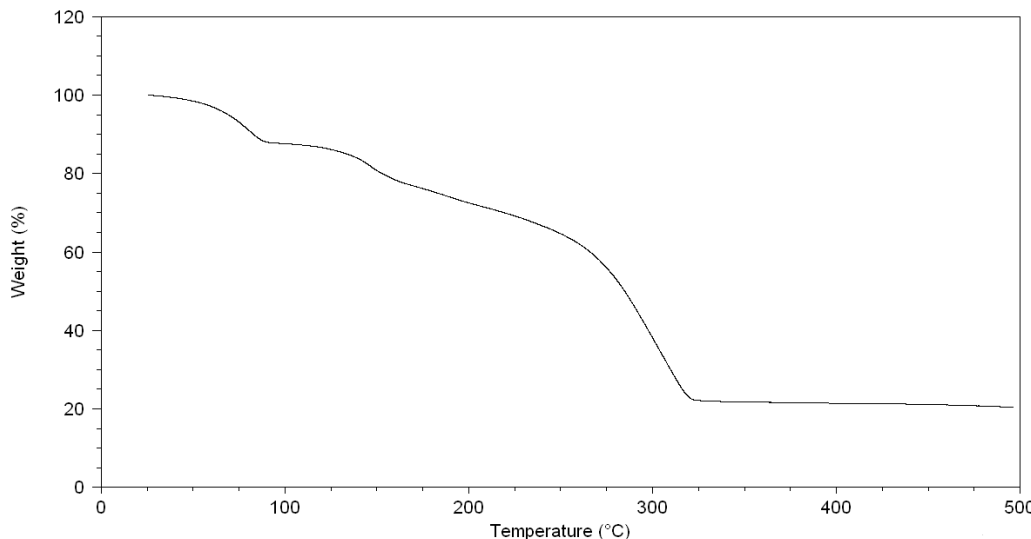


**Figure 4.5.** TGA of **13**.

The synthesis of **13** was also attempted via solvent vapor diffusion with untreated THF and already oxidized solutions (solutions that were allowed to sit for 5 days before crystallization). Crystals of **13** were observed to grow more readily when the THF and atmosphere were bubbled with oxygen and the oxidation and crystallization were allowed to occur at the same time, whereas they were not observed when  $\text{O}_2$  was only bubbled into the solution and the oxidation was allowed to occur first before crystallization.

The asymmetric unit of **14** contains three unique Cu(II) centers, as seen in Figure 4.6. Both Cu2 and Cu3 have similar distorted octahedral coordination geometries; they are each coordinated to two pyrimidines, two bridging hydroxide ligands, one water

## Chapter 4

molecule, and one weakly coordinated  $\text{BF}_4^-$  (weak bonds shown as red dashed lines). The important difference in the two Cu(II) centers, however, is that the pyrimidines on Cu2 bridge to other Cu(II) centers, while the pyrimidines on Cu3 are terminal. It is unusual to see terminal, or non-bridging, pyrimidines in coordination polymers, although we have observed this before (the afore mentioned  $[\text{Cu}(\text{pyrimidine})_4]_2\text{BF}_4$ )<sup>1</sup>, and Yasui and colleagues also reported a Cu(II) coordination polymer containing a terminal pyrimidine.<sup>14</sup> Cu1 also has an octahedral coordination environment, as it is coordinated to two  $\text{BF}_4^-$  anions and four bridging pyrimidine ligands. Selected bond lengths and angles in **14** are given in Table 4.2.

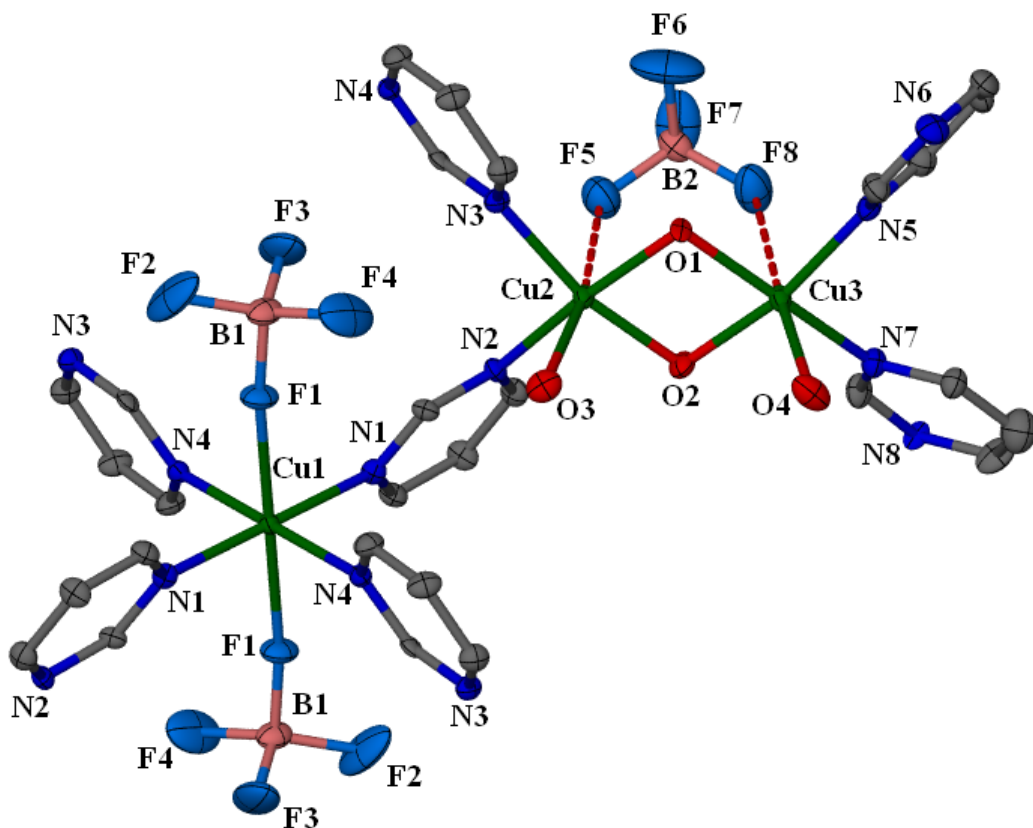


**Figure 4.6.** Coordination environment of the three unique Cu(II) centers in **14**.

All atoms shown as 50% probability thermal ellipsoids. Hydrogen atoms have been omitted for clarity and colors are as listed previously. Boron is shown in pink, fluorine in sky blue. The red dashed lines denote a weak bond between the fluorine and copper atoms.

| Bond Lengths (Å)       | Bond Angles (deg)              |                                |
|------------------------|--------------------------------|--------------------------------|
| Cu(1) – F(1): 2.294(3) | F(1) – Cu(1) – N(1): 88.04(2)  | N(2) – Cu(2) – N(3): 97.26(2)  |
| Cu(1) – N(1): 2.036(4) | F(1) – Cu(1) – N(1): 91.96(2)  | N(3) – Cu(2) – O(3): 90.37(2)  |
| Cu(1) – N(4): 2.067(4) | N(1) – Cu(1) – N(4): 89.38(2)  | N(3) – Cu(2) – F(5): 85.18(2)  |
| Cu(2) – O(1): 1.948(3) | N(1) – Cu(1) – N(4): 90.62(2)  | O(1) – Cu(3) – O(2): 81.7(2)   |
| Cu(2) – O(2): 1.898(3) | F(1) – Cu(1) – N(4): 88.73(2)  | O(1) – Cu(3) – O(4): 98.5(3)   |
| Cu(2) – O(3): 2.349(4) | F(1) – Cu(1) – N(4): 91.27(2)  | O(1) – Cu(3) – N(5): 89.7(2)   |
| Cu(2) – N(2): 2.015(4) | O(1) – Cu(2) – O(2): 82.2(3)   | O(1) – Cu(3) – N(7): 170.8(3)  |
| Cu(2) – N(3): 2.013(4) | O(1) – Cu(2) – O(3): 98.0(3)   | O(1) – Cu(3) – F(8): 82.57(2)  |
| Cu(2) – F(5): 2.674(4) | O(1) – Cu(2) – N(2): 172.3(2)  | O(2) – Cu(3) – O(4): 97.71(2)  |
| Cu(3) – O(1): 1.954(3) | O(1) – Cu(2) – N(3): 88.2(3)   | O(2) – Cu(3) – N(5): 168.80(2) |
| Cu(3) – O(2): 1.912(4) | O(1) – Cu(2) – F(5): 88.64(2)  | O(2) – Cu(3) – N(7): 94.57(2)  |
| Cu(3) – O(4): 2.353(4) | O(2) – Cu(2) – O(3): 99.61(2)  | O(2) – Cu(3) – F(8): 97.73(2)  |
| Cu(3) – N(5): 2.007(5) | O(2) – Cu(2) – N(2): 91.53(2)  | O(4) – Cu(3) – F(8): 177.25(2) |
| Cu(3) – N(7): 2.012(4) | O(2) – Cu(2) – N(3): 167.02(2) | N(5) – Cu(3) – O(4): 90.59(2)  |
| Cu(3) – F(8): 2.729(4) | O(2) – Cu(2) – F(5): 86.01(2)  | N(5) – Cu(3) – F(8): 87.89(2)  |
|                        | O(3) – Cu(2) – F(5): 170.88(2) | N(5) – Cu(3) – N(7): 92.89(2)  |
|                        | N(2) – Cu(2) – O(3): 87.34(2)  | N(7) – Cu(3) – O(4): 90.28(2)  |
|                        | N(2) – Cu(2) – F(5): 85.34(2)  | N(7) – Cu(3) – F(8): 87.61(2)  |

**Table 4.2.** Selected bond lengths and angles in **14**.

Two of the pyrimidine ligands bridge Cu1 to Cu3 in another asymmetric unit, while two of the pyrimidines on Cu2 bridge to another Cu1 to form a ladder-like structure (Figure 4.7). In addition to the two coordinated waters, there is one non-coordinating water in **14**, and together they form a small hydrogen-bonded network (Figure 4.8). The two coordinated waters hydrogen bond to the unbound water, which in turn hydrogen bonds to a non-coordinating  $\text{BF}_4^-$ . Hydrogen bond distances in **14** are listed in Table 4.3.

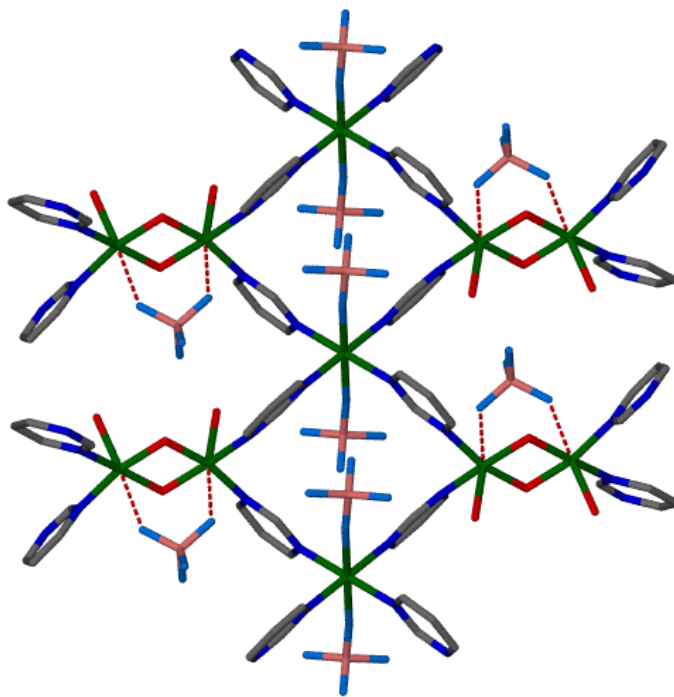


**Figure 4.7.** Ladders formed in **14**.

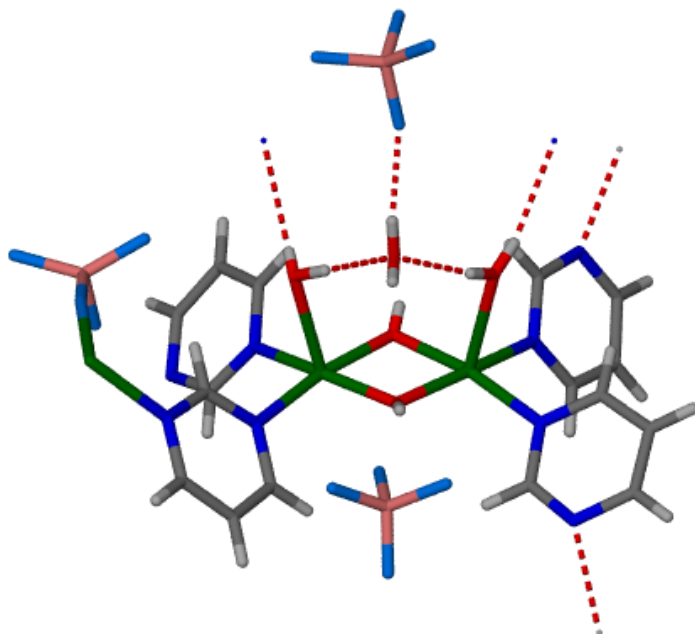


**Figure 4.8.** Unique hydrogen bonds in **14**.

| D – H – A       | D(H – A), Å | d(D – A), Å |
|-----------------|-------------|-------------|
| O5 – H24 – F10  | 1.940       | 2.694       |
| O5 – H24 – F12A | 3.324       | 4.097       |
| O5 – H24 – F9   | 3.739       | 4.484       |
| O4 – H19 – F12  | 3.767       | 4.206       |
| O4 – H19 – N6   | 2.198       | 2.934       |
| O4 – H20 – O5   | 2.061       | 2.785       |
| O4 – H20 – O3   | 3.541       | 3.961       |
| O4 – H20 – F6   | 3.643       | 4.236       |
| O4 – H20 – F10  | 3.811       | 4.324       |
| O3 – H21 – O5   | 1.976       | 2.784       |
| O3 – H21 – O4   | 3.402       | 3.961       |
| O3 – H21 – F6   | 3.214       | 3.706       |
| O3 – H21 – F10  | 3.804       | 4.428       |
| O3 – H22 – F4   | 2.985       | 3.219       |
| O3 – H22 – F12A | 3.661       | 3.952       |
| O3 – H22 – N8   | 2.349       | 2.870       |
| O5 – H23 – F6   | 2.143       | 2.710       |
| O5 – H23 – O1   | 2.389       | 2.938       |
| O5 – H23 – F8   | 3.083       | 3.830       |
| O5 – H23 – F5   | 3.449       | 4.188       |
| O5 – H23 – N3   | 3.552       | 3.940       |
| O2 – H18 – F6   | 2.317       | 2.870       |
| O2 – H18 – F7   | 3.548       | 4.150       |
| O2 – H18 – F4A  | 3.544       | 3.818       |
| O1 – H17 – F12A | 2.503       | 3.089       |
| O1 – H17 – F10  | 2.861       | 3.418       |
| O1 – H17 – F12  | 3.596       | 4.197       |
| O1 – H17 – F9   | 3.755       | 4.281       |

**Table 4.3.** Hydrogen bond distances in **14**. D = donor atom, A = acceptor atom,  
H = hydrogen.

The ladders pack together in offset layers connected by hydrogen bonds, as seen in Figures 4.9 and 4.10. The hydrogen bonds connecting the layers connect the free

nitrogen on the terminal pyrimidine on one layer to a coordinated water in another layer. So although the pyrimidines aren't bridging, they do play an important role in the hydrogen-bonded extended network. Figure 4.11 shows the packing diagram of **14** within the unit cell looking down the *b*-axis. Unlike in the previous chapter, these layers are not close enough together for the pyrimidines to participate in  $\pi - \pi$  stacking.

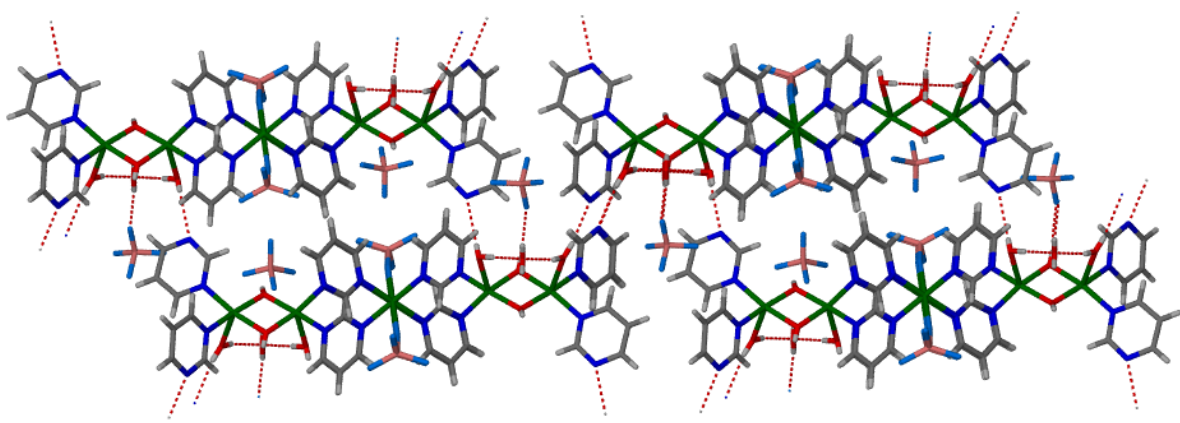


**Figure 4.9.** Hydrogen-bonded network in **14**.

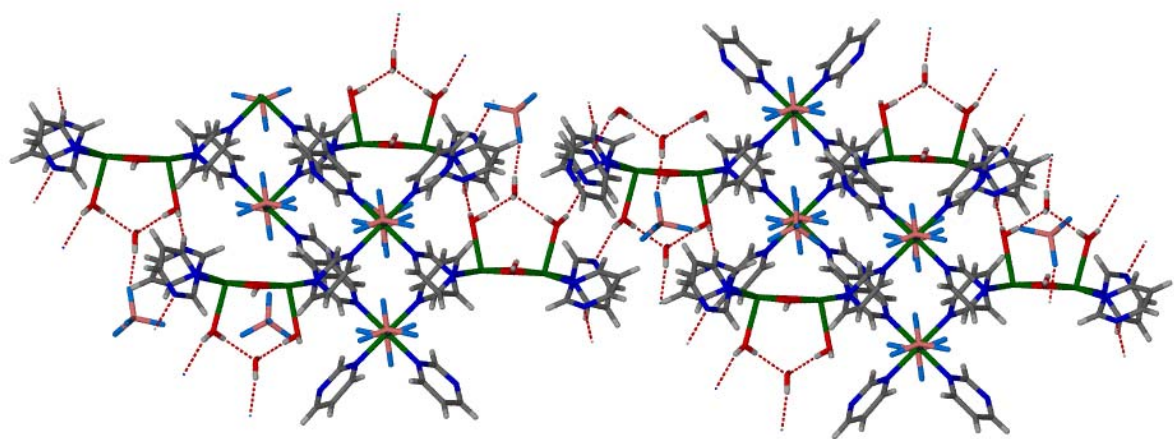


**Figure 4.10.** Alternate view of the hydrogen-bonded network in **14**.

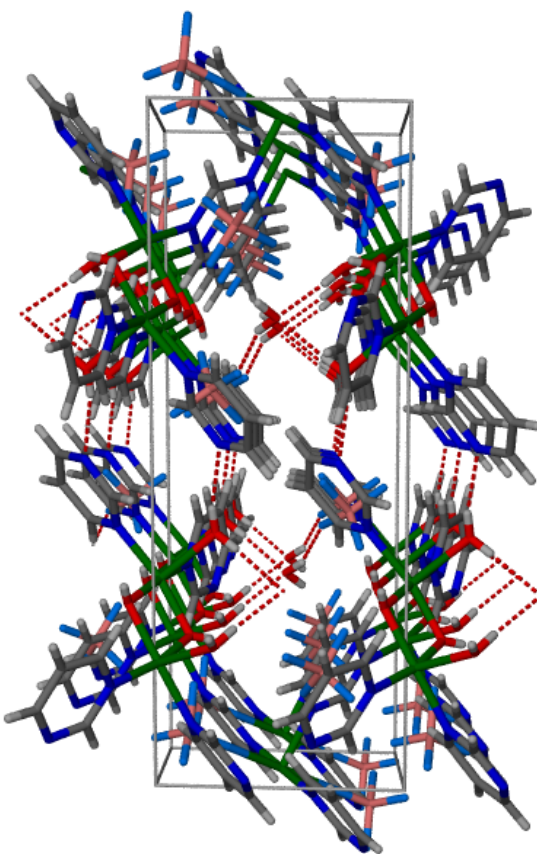


**Figure 4.11.** Packing diagram of the ladders in **14** viewed down the *b*-axis.

Thermogravimetric analysis was performed on **14** and the results are shown in Figure 4.12. Powder X-ray diffraction has not yet been performed on the residue of **14**, but the following calculations were performed under the assumption that the Cu(II) centers were reduced to Cu. Again, the exact mechanism of reduction is not known at this time. The first weight loss occurs at about 150 °C and corresponds to the loss of the 3 water molecules and the 2 hydroxide ions, which are likely lost as waters (11.49 % observed, 10.64 % calculated). The calculations of the second weight loss and residue for the remaining material do not match the observed values. The second weight loss occurs between 150 and 325 °C and should correspond to the loss of 4 pyrimidine ligands.

and the  $3\text{BF}_4^-$  anions, but it does not (60.92% observed, 70.17 % calculated). The residue should correspond to 2.5 Cu atoms, but it also does not (27.70 % observed, 19.19 % calculated). The reason for the large discrepancy is not known at this time. Further experiments (including powder X-ray diffraction and solid-state  $^{19}\text{F}$ -NMR on the residue) will need to be performed.

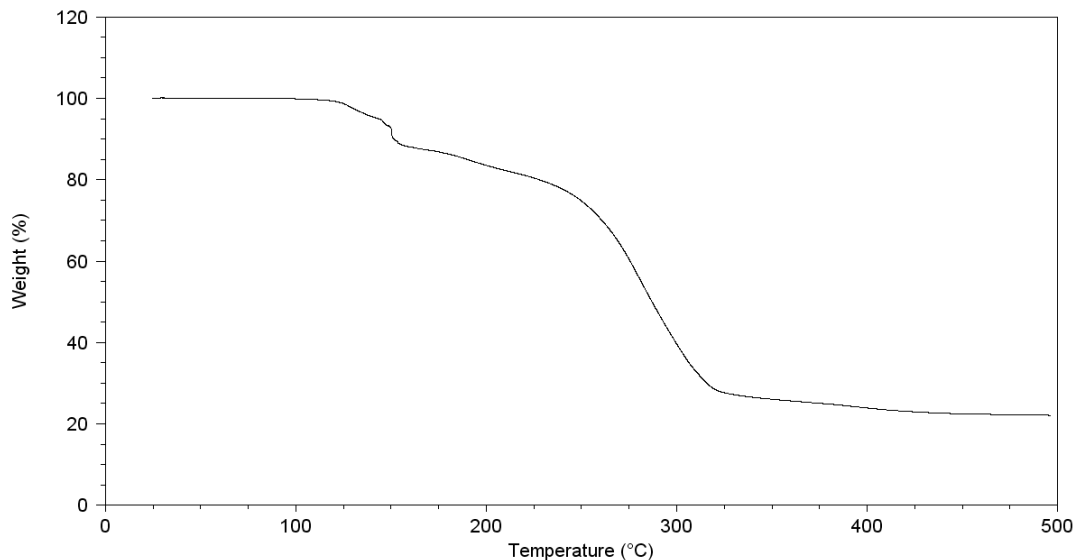


**Figure 4.12.** TGA of **14**.

After our success in forming a mixed valent complex and a completely oxidized structure using  $\text{BF}_4^-$  as the counteranion, similar experiments were done using  $\text{PF}_6^-$  as the counteranion instead of  $\text{BF}_4^-$ . This lead to the discovery of two new compounds, the non-oxidized, Cu(I)-containing **15** and the oxidized Cu(II)-containing **16**.

The asymmetric unit of **15** contains three unique Cu(I) centers, as shown in Figure 4.13. Cu1 is coordinated to three pyrimidine ligands and one acetonitrile ligand and exhibits a distorted tetrahedral geometry. Cu2 is coordinated to four pyrimidine ligands,

also resulting in a slightly distorted tetrahedral geometry. Cu3 is coordinated to three pyrimidine rings, which results in a distorted trigonal planar geometry. Selected bond lengths and angles in **15** are listed in Table 4.4.

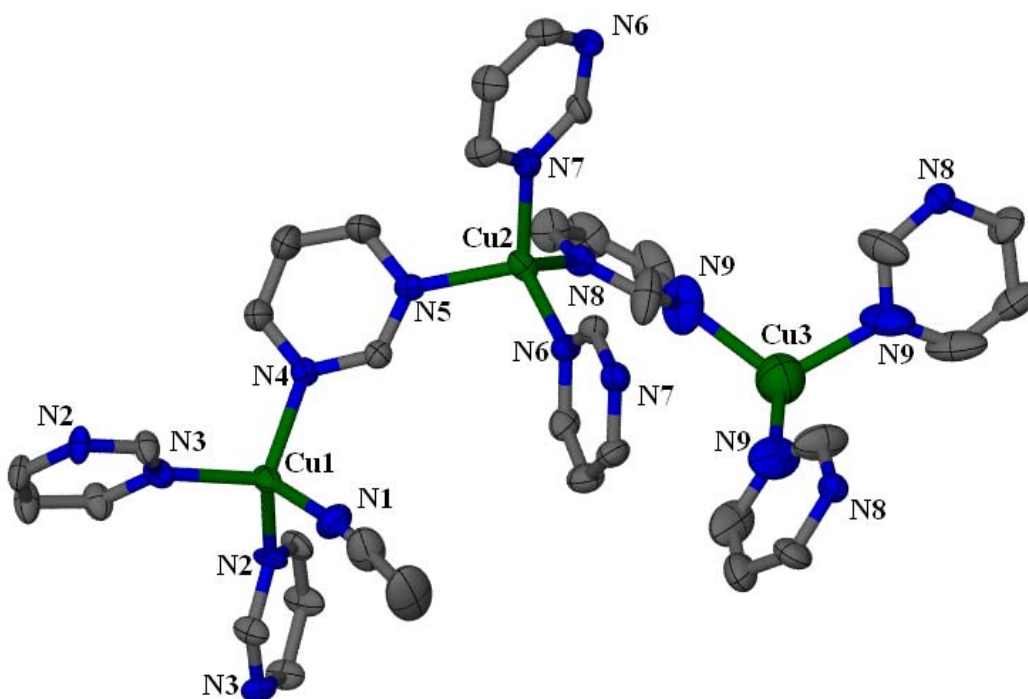


**Figure 4.13.** Coordination environments of the three unique Cu(I) centers in **15**.

All atoms shown as 50% probability thermal ellipsoids. Hydrogen atoms have been omitted for clarity, and colors as listed previously.

| Bond Lengths (Å)        | Bond Angles (deg)             |
|-------------------------|-------------------------------|
| Cu(1) – N(1): 1.993(9)  | N(1) – Cu(1) – N(2): 104.6(3) |
| Cu(1) – N(2): 2.042(7)  | N(1) – Cu(1) – N(3): 107.2(3) |
| Cu(1) – N(3): 2.041(7)  | N(1) – Cu(1) – N(4): 108.0(3) |
| Cu(1) – N(4): 2.035(7)  | N(2) – Cu(1) – N(3): 109.9(3) |
| Cu(2) – N(5): 2.047(7)  | N(2) – Cu(1) – N(4): 116.8(3) |
| Cu(2) – N(6): 2.052(6)  | N(3) – Cu(1) – N(4): 109.8(3) |
| Cu(2) – N(7): 2.061(7)  | N(5) – Cu(2) – N(6): 109.8(3) |
| Cu(2) – N(8): 2.047(7)  | N(5) – Cu(2) – N(7): 106.9(3) |
| Cu(3) – N(9): 2.154(13) | N(5) – Cu(2) – N(8): 108.7(3) |
|                         | N(6) – Cu(2) – N(7): 106.7(3) |
|                         | N(6) – Cu(2) – N(8): 112.5(3) |
|                         | N(7) – Cu(2) – N(8): 112.1(3) |
|                         | N(9) – Cu(3) – N(9): 113.3(3) |

**Table 4.4.** Selected bond lengths and angles in **15**.

Each pyrimidine in the structure bridges to another Cu(I) and the result is a cage-like structure within which a  $\text{PF}_6^-$  anion resides (Figures 4.14 and 4.15). The inner volume of the cage is approximately 190 Å. Similar compounds with  $\text{PF}_6^-$  and  $\text{ClO}_4^-$  as the counteranions have previously been reported (Figure 4.16).<sup>2</sup>

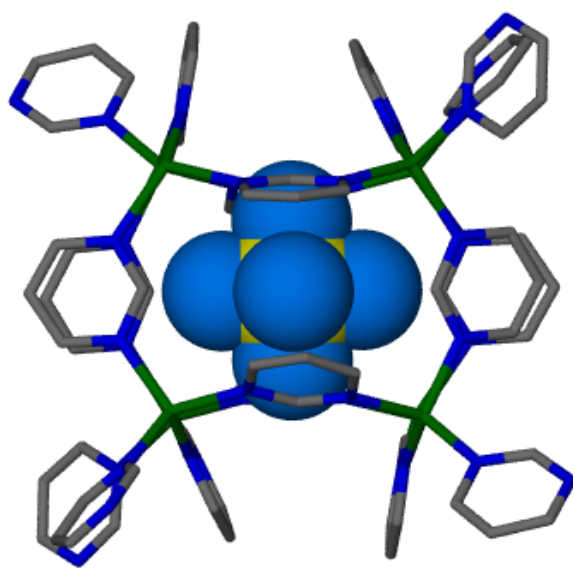


**Figure 4.14.** Rectangular cage formed by the bridging pyrimidines in **15**. A  $\text{PF}_6^-$  anion (in spacefill) resides in the middle of the cage.

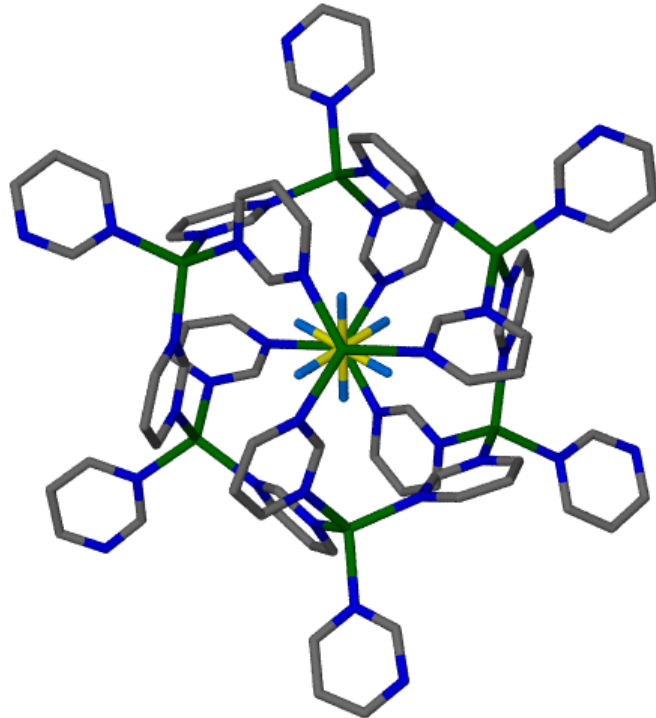


**Figure 4.15.** Alternate view of **15** down the body diagonal of the cube.

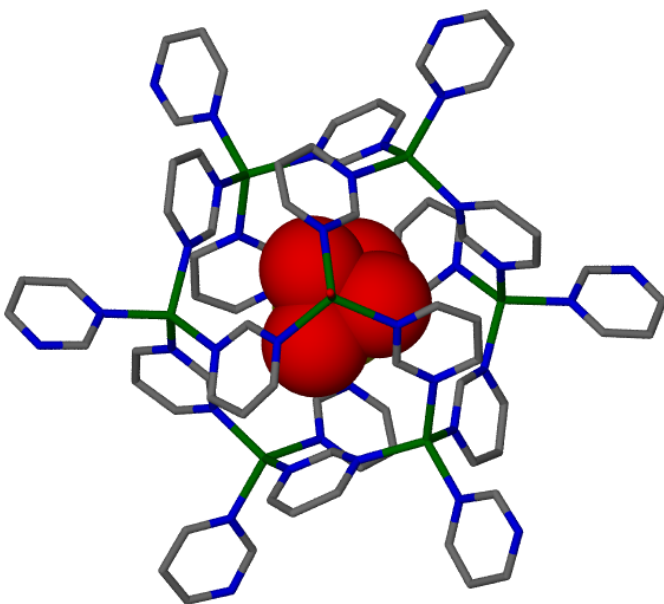


**Figure 4.16.** The previously reported

$[\text{Cu}_{1.3}(\text{pyrimidine})_{2.5}(\text{OH})_{0.167}(\text{H}_2\text{O})_{0.167}](\text{ClO}_4)_{1.167}$  cage containing an enclosed disordered perchlorate anion (spacefill).

The previously reported compounds contained many disordered solvent molecules, and therefore the crystal structures of the compounds were difficult to solve. The difference between those structures and **15** is that **15** was put under vacuum for 3 days to remove excess solvent from the structure so that the crystal structure would be cleaner and easier to solve. Figure 4.17 shows the structure of **15** viewed down the (111) plane, while Figure 4.18 shows the previously reported  $[\text{Cu}_{1.3}(\text{pyrimidine})_{2.5}(\text{OH})_{0.167}(\text{H}_2\text{O})_{0.167}](\text{PF}_6)_{1.167}$  with the disordered solvent included to illustrate the difficulty in the structure determination as compared to **15**.

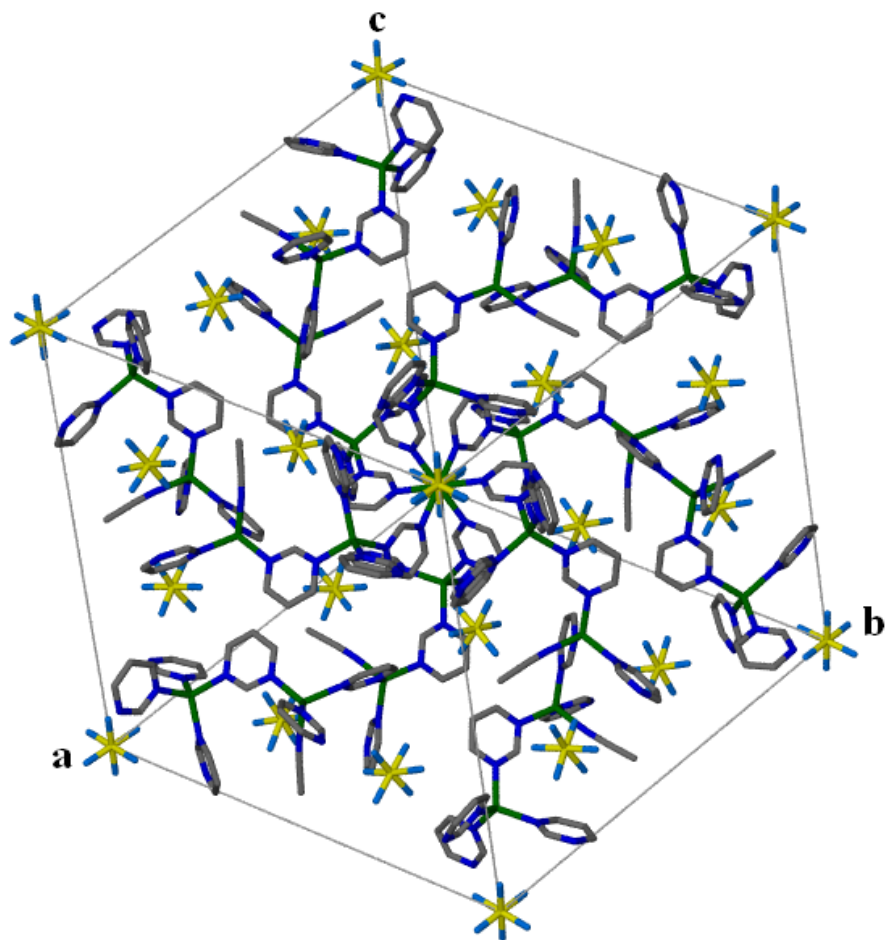


**Figure 4.17.** Unit cell diagram of **15** viewed down the (111) plane.

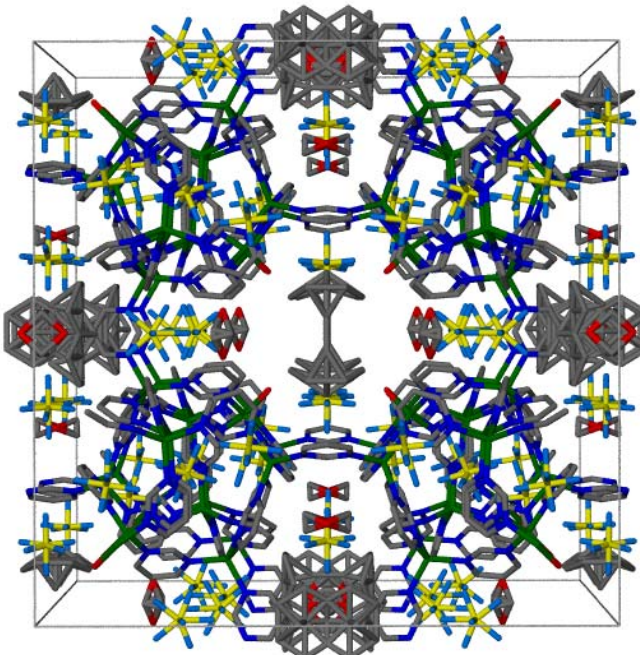


**Figure 4.18.** Packing diagram of previously reported  $[\text{Cu}_{1.3}(\text{pyrimidine})_{2.5}(\text{OH})_{0.167}(\text{H}_2\text{O})_{0.167}](\text{PF}_6)_{1.167}$  within the unit cell viewed down the *c*-axis. Anions and disordered solvent molecules are included.

The previously reported structures have shown promise in anion exchange.<sup>2</sup> Ion exchange experiments have not been performed with **15**. The structure of **15** does not appear to have the large channels that the previously reported structures have, but it does still have the cages, and a  $\text{PF}_6^-$  anion resides in each cage. It would be interesting to see if **15** has the same anion exchange properties as the previously reported structure.

Thermogravimetric analysis of **15** was performed, the results of which are shown in Figure 4.19. Since **15** is comprised of only Cu(I) centers, it is assumed that the compound is reduced to Cu from the powder X-ray diffraction results presented in Chapter 3 for the Cu(I)-containing **9**. Again, the exact mechanism of reduction is

currently unknown and will require further experimentation. The first weight loss of **15** occurs at  $\sim 200$  °C and corresponds to the loss of the MeCN molecule and one pyrimidine ligand (13.54 % observed, 15.12 % calculated). The second weight loss occurs between 200 and 350 °C and corresponds to the loss of 2.5 pyrimidine ligands and 2.3  $\text{PF}_6^-$  anions (66.93 % observed, 66.63 % calculated). The residue corresponds to 2.3 Cu atoms (19.53 % observed, 18.25 % calculated).

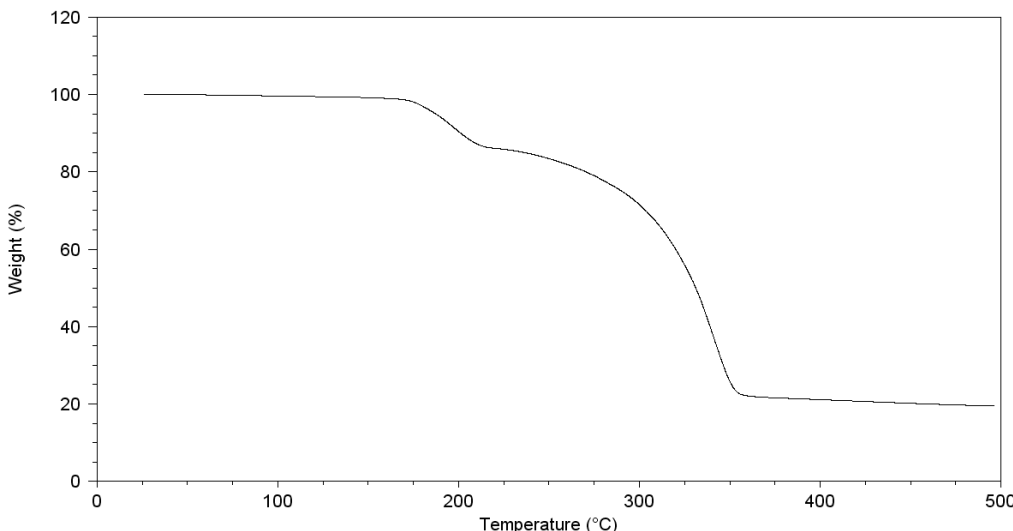


**Figure 4.19.** TGA of **15**.

Experiments in which water was introduced into the synthesis were also performed. A solution containing a 1:1:2 ratio of Cu(I) to pyrimidine to water was saturated with  $\text{O}_2$ , and crystals of **16** grew within a few days.

The asymmetric unit of **16** contains one unique Cu(II) center that has a slightly distorted octahedral coordination geometry (Figure 4.20). Atom Cu1 is bonded to two bridging pyrimidines, three water molecules, and one hydroxide group (atom O1

represents the hydroxide group). Selected bond lengths and angles in **16** are listed in Table 4.5.

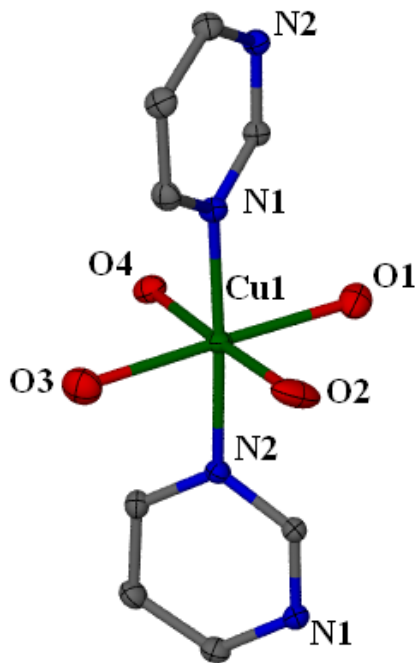


**Figure 4.20.** Coordination environment around the unique Cu(II) center in **16**.

All atoms shown as 50% probability thermal ellipsoids. Hydrogen atoms omitted for clarity. Colors as listed previously.

| Bond Lengths (Å)       | Bond Angles (deg)              |                                |  |
|------------------------|--------------------------------|--------------------------------|--|
| Cu(1) – N(1): 2.016(2) | N(1) – Cu(1) – N(2): 177.06(9) | N(2) – Cu(1) – O(3): 91.43(8)  |  |
| Cu(1) – N(2): 2.018(2) | N(1) – Cu(1) – O(1): 90.94(8)  | N(2) – Cu(1) – O(4): 86.26(7)  |  |
| Cu(1) – O(1): 2.206(2) | N(1) – Cu(1) – O(2): 88.27(8)  | O(1) – Cu(1) – O(2): 89.69(8)  |  |
| Cu(1) – O(2): 2.054(2) | N(1) – Cu(1) – O(3): 90.89(8)  | O(1) – Cu(1) – O(3): 178.15(7) |  |
| Cu(1) – O(3): 2.226(2) | N(1) – Cu(1) – O(4): 92.11(7)  | O(1) – Cu(1) – O(4): 93.55(7)  |  |
| Cu(1) – O(4): 2.097(2) | N(2) – Cu(1) – O(1): 86.72(8)  | O(2) – Cu(1) – O(3): 90.63(8)  |  |
|                        | N(2) – Cu(1) – O(2): 93.49(8)  | O(2) – Cu(1) – O(4): 176.72(8) |  |
|                        |                                | O(3) – Cu(1) – O(4): 86.11(7)  |  |

**Table 4.5.** Selected bond lengths and angles in **16**.

The bond lengths in **16** suggest that the complex exhibits typical Jahn-Teller distortion. The Jahn-Teller effect occurs in octahedral  $d^9$  complexes, especially Cu(II) complexes, and occurs because the d orbitals (the  $e_g$  orbital in particular) split and are no longer degenerate like they would be in an octahedral complex. In this case, the  $d_{z^2}$ ,  $d_{xz}$ , and  $d_{yz}$  orbitals increase in energy while the  $d_{x^2-y^2}$  and  $d_{xy}$  orbitals decrease in energy (Figure 4.21). This results in compression along the z-axis and elongation along the x- and y-axes, as demonstrated in the bond lengths given above (the Cu–N distances are smaller than the Cu–O distances). This type of distortion is actually fairly rare. The distortion usually observed results in the elongation of the z-axis and the compression of the x- and y-axes. Distortion is energetically favorable if there are one, two, or three electrons in the  $e_g$  orbitals as at least two of them can occupy an orbital at a lower energy.<sup>15</sup>

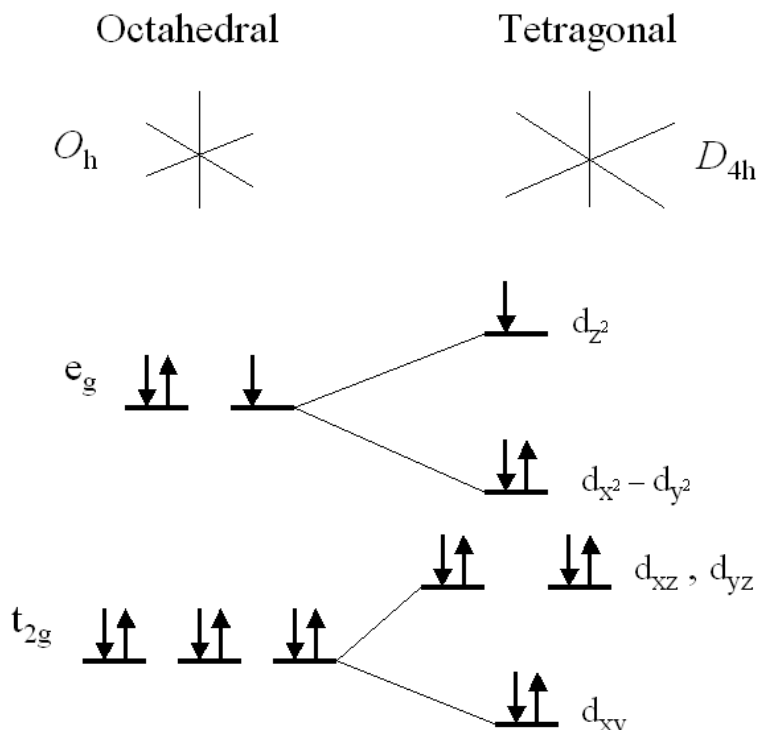


**Figure 4.21.** Diagram of the Jahn-Teller distortion that occurs in **16**.

The pyrimidines bridge to other Cu(II) centers to form ribbons, as shown in Figure 4.22.

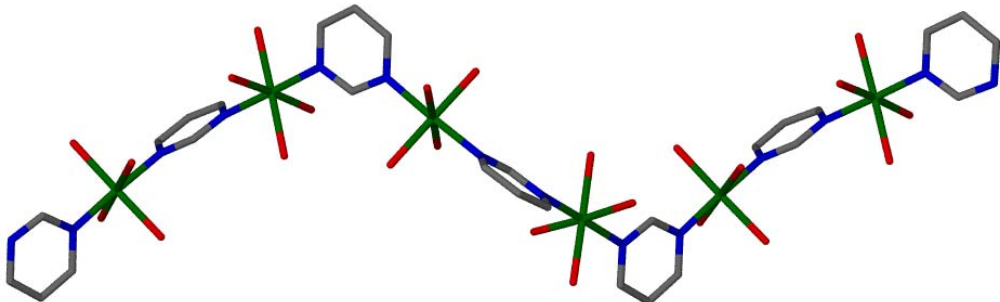


**Figure 4.22.** Ribbons formed by bridging pyrimidines in **16**.

One ribbon is connected to other neighboring ribbons through an intricate hydrogen-bonded network. Each water (the three coordinated and one free water), hydroxyl group, and  $\text{PF}_6^-$  anion in the structure participates in hydrogen bonding. In fact, each  $\text{PF}_6^-$  serves as a sort of bridge between the ribbons, as the coordinated waters on one ribbon form hydrogen bonds to one of the fluorine atoms on the anion, and the same anion forms a hydrogen bond via one of its other fluorine atoms to a coordinated water on a neighboring ribbon (Figures 4.23 and 4.24). Hydrogen bond distances in **16** are given in Table 4.6. The packing diagram of **16** within the unit cell viewed down the  $a$ -axis is shown in Figure 4.25. The hydrogen atoms and bonds have been omitted from Figure 4.25 in order to clearly see the packing of the ribbons.

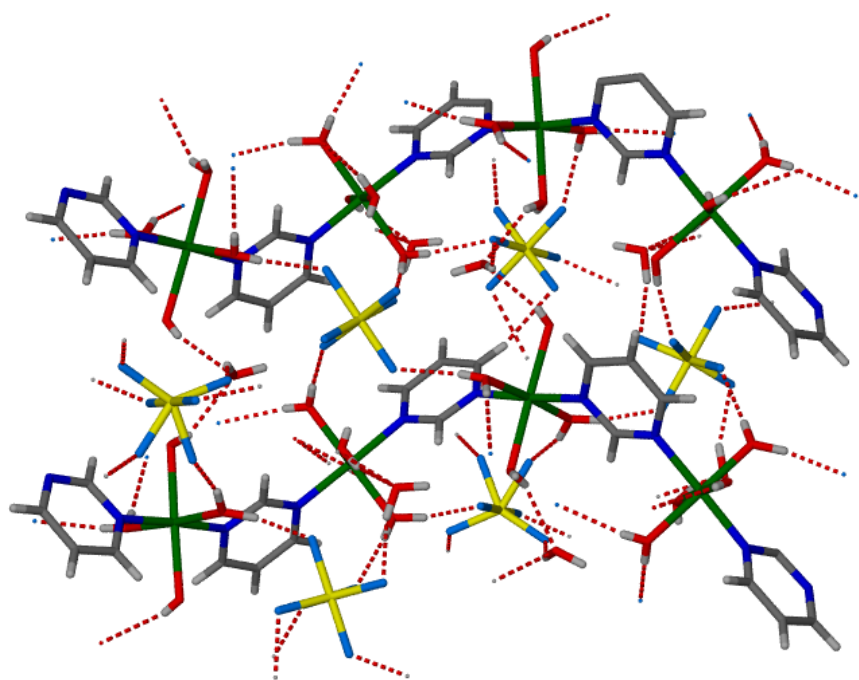


**Figure 4.23.** Hydrogen-bonded network connecting the ribbons in **16**.

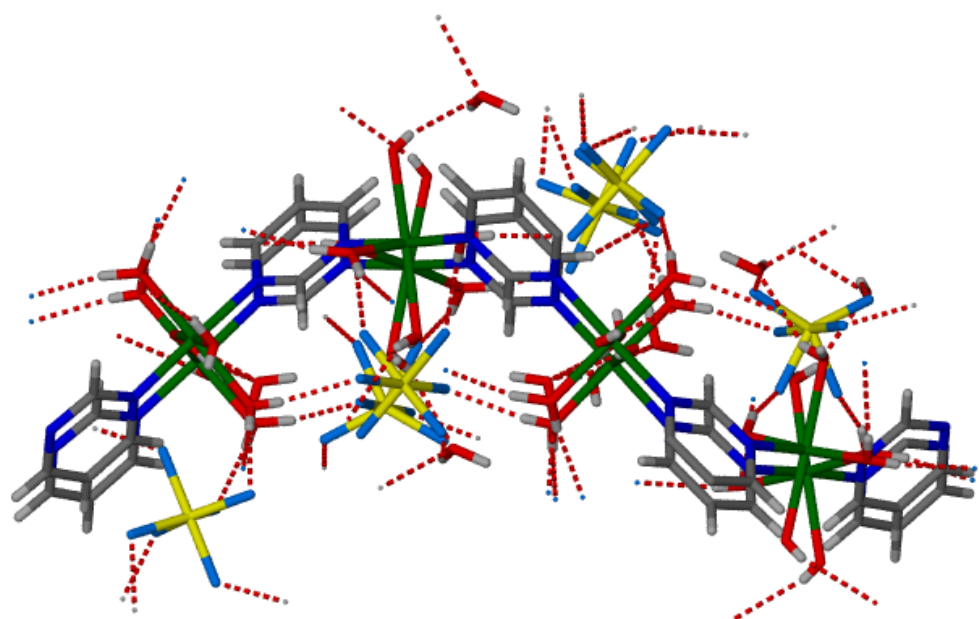


**Figure 4.24.** Alternate view of the hydrogen-bonded network in **16**.

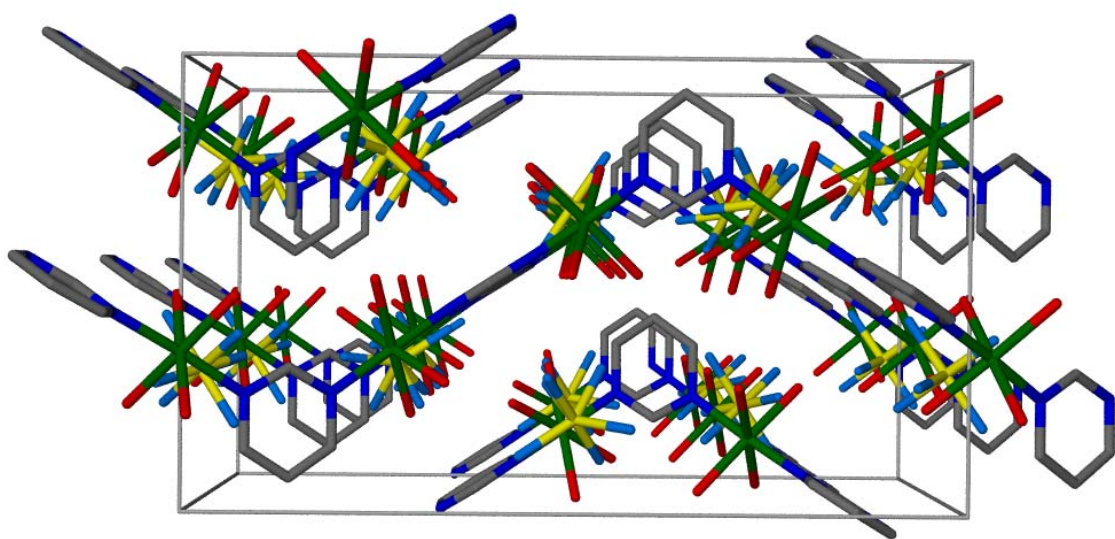


**Figure 4.25.** Packing diagram of **16** within the unit cell viewed down the *a*-axis. Hydrogen atoms and bonds omitted for clarity.

| <b>D – H – A</b> | <b>d(H – A), Å</b> | <b>d(D – A), Å</b> | <b>D – H – A</b> | <b>d(H – A), Å</b> | <b>d(D – A), Å</b> |
|------------------|--------------------|--------------------|------------------|--------------------|--------------------|
| O4 – H11 – F1    | 3.446              | 3.978              | O3 – H9 – F3     | 2.264              | 2.783              |
| O4 – H11 – F2    | 2.990              | 3.514              | O1 – H5 – F3     | 3.690              | 3.967              |
| O4 – H11 – F3    | 2.018              | 2.693              | O1 – H5 – F5A    | 3.716              | 4.094              |
| O4 – H10 – F1    | 2.051              | 2.732              | O1 – H5 – F6     | 3.277              | 3.661              |
| O4 – H10 – F1    | 3.735              | 4.358              | O1 – H5 – O3     | 3.158              | 3.579              |
| O4 – H10 – F3    | 3.690              | 4.186              | O1 – H5 – O5     | 2.173              | 2.737              |
| O4 – H10 – O5    | 3.623              | 3.990              | O3 – H8 – F4     | 3.562              | 4.051              |
| O2 – H6 – F4     | 1.877              | 2.663              | O3 – H8 – F4A    | 3.261              | 3.883              |
| O2 – H6 – F4     | 3.122              | 3.815              | O3 – H8 – F5     | 3.674              | 4.365              |
| O2 – H6 – F4A    | 1.894              | 2.685              | O3 – H8 – F6     | 2.527              | 2.911              |
| O2 – H6 – F5     | 3.301              | 4.035              | O3 – H8 – O5     | 2.175              | 2.828              |
| O2 – H6 – F6     | 3.083              | 3.697              | O5 – H12 – F4    | 3.533              | 3.973              |
| O2 – H6 – O1     | 3.489              | 3.878              | O5 – H12 – F4A   | 2.723              | 3.187              |
| O2 – H7 – F4     | 3.447              | 4.034              | O5 – H12 – F5    | 1.914              | 2.690              |
| O2 – H7 – F4A    | 3.093              | 3.561              | O5 – H12 – F5A   | 2.015              | 2.887              |
| O2 – H7 – F5     | 2.689              | 3.157              | O5 – H12 – F5A   | 3.43               | 4.247              |
| O2 – H7 – F5A    | 3.072              | 3.644              | O5 – H12 – F6    | 2.509              | 2.942              |
| O2 – H7 – F5A    | 3.527              | 4.320              | O5 – H13 – F1    | 2.121              | 2.932              |
| O2 – H7 – F6     | 1.784              | 2.666              | O5 – H12 – F2    | 2.287              | 2.969              |
| O2 – H7 – O1     | 3.441              | 3.878              | O5 – H12 – F3    | 3.299              | 3.975              |
| O2 – H7 – O3     | 3.490              | 4.122              | O5 – H12 – F3    | 3.652              | 4.47               |
| O3 – H9 – F1     | 2.599              | 3.016              | O5 – H12 – O3    | 3.246              | 3.740              |
| O3 – H9 – F2     | 3.197              | 3.642              | O5 – H12 – O4    | 3.573              | 3.990              |

**Table 4.6.** Hydrogen bond distances in **16**. D = donor atom, A = acceptor atom, H = hydrogen.

Thermogravimetric analysis of **16** was performed and is shown in Figure 4.26.

Powder X-ray diffraction has not yet been performed on the residue of **16**, but the calculations that follow were done under the assumption that the Cu(II) centers were reduced to Cu. Again, the mechanism of reduction is not fully known at this point and further experimentation will need to be performed. The first weight loss occurs at ~75 °C

and corresponds to the loss of four water molecules (20.93 % observed, 19.08 % calculated). The calculated weights of the remaining material and residue do not agree with the observed values. The observed value of the residue in particular, if it is in fact Cu, is two times larger than the calculated value (38.46 % observed, 16.83 % calculated). It is not known at this time why the difference is so large. Further experimentation will need to be performed to explain this phenomenon.

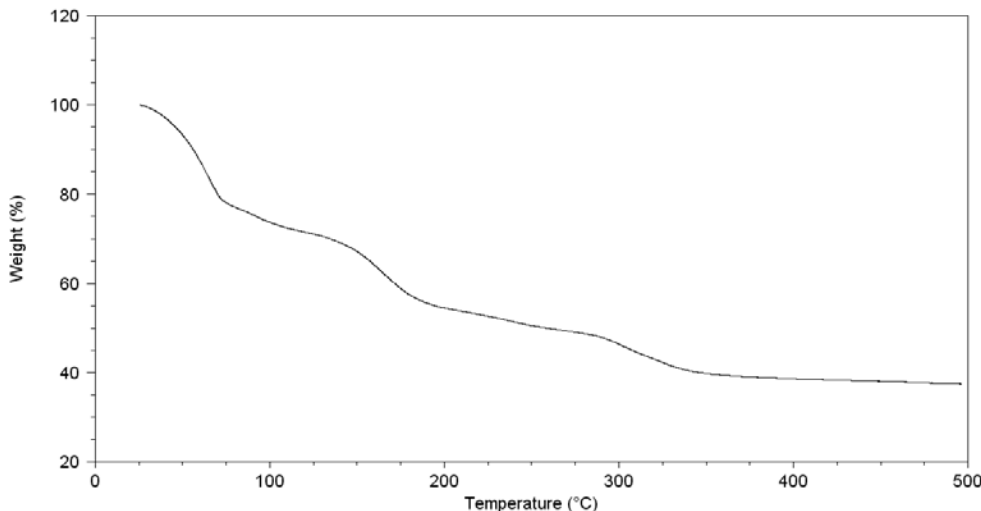


**Figure 4.26.** TGA of 16.

This project is still in its infancy, as there are still numerous experiments to attempt. Preliminary studies using 4,4'-bipyridine (bipy) and 4,7-phenanthroline (phen) as ligands instead of pyrimidine have also yielded some interesting results. Using a 1:1 ratio of Cu(I) to bipy in acetonitrile and nitrobenzene under either an argon or O<sub>2</sub> atmosphere results in the formation of an orange precipitate and crystals. However, when 2 equivalents of water are added to the same mixture under O<sub>2</sub>, periwinkle blue powder and crystals formed. The crystals obtained thus far have been too small for single crystal

## Chapter 4

X-ray diffraction. Using a 1:1 ratio of Cu(I) to phen in acetonitrile and nitrobenzene under either argon or oxygen results in a pale yellow solution, and the addition of 2 equivalents of water added to the mixture under O<sub>2</sub> still results in a pale yellow solution. Table 4.7 summarizes the experimental results obtained to date for the conditions required for oxidation of Cu(I) in the presence of the three different ligands. The observations so far may be due to the different strengths of the ligands. Phenanthroline is the strongest ligand of the three, and most likely stabilizes the Cu(I) centers of the complexes it forms.

| Ligand             | Oxidation in the presence of O <sub>2</sub> ? | Oxidation in the presence of O <sub>2</sub> + H <sub>2</sub> O? |
|--------------------|---|---|
| Pyrimidine         | Yes   | Yes   |
| 4,4'-Bipyridine    | No  | Yes   |
| 4,7-Phenanthroline | No  | No  |

**Table 4.7.** Summary of the conditions required for the oxidation of Cu(I) in the presence of pyrimidine, bipy, and phen.

## 4.4 Conclusions

What started out as one experiment to pinpoint specific synthesis conditions has branched into a larger project designed to study the coordination polymers that result from the oxidation of Cu(I) in solution. Two new oxidized compounds have been discovered along the way thus far. To date, only X-ray crystallographic and TGA data has been collected and analyzed, and the structures studied may have interesting magnetic properties or may be useful in ion exchange reactions or catalysis. Preliminary results in changing the ligand from pyrimidine to bipy have demonstrated that different environmental conditions are necessary for the oxidation of Cu(I), while the use of phen has not resulted in the oxidation of Cu(I) under any of the experimental conditions tested. The details as to why these different conditions are necessary for oxidation are not immediately known, as further studies need to be performed.

## 4.5 References

1. Novak, B.; Keller, S. W., Crystal and molecular structure of  $[\text{Cu}(\text{pyrimidine})_4]2\text{BF}_4$ . *J. Chem. Cryst.* **1997**, 27, (5), 279-282.
2. Knight, D. A. Anion and Solvent Influences on the Self Assembly of Copper(I) Coordination Solids. Dissertation, University of Missouri-Columbia, Columbia, 2005.
3. Klotz, I. M.; Czerlinski, G. H.; Fiess, H. A., A Mixed-Valence Copper Complex with Thiol Compounds. *J. Am. Chem. Soc.* **1958**, 80, (12), 2920-2923.
4. Sigwart, C.; Hemmerich, P.; Spence, J. T., A Binuclear Mixed-Valence Copper Acetate Complex as a Model for Copper-Copper Interaction in Enzymes. *Inorg. Chem.* **1968**, 7, (12), 2545-2548.
5. Kappenstein, C., X-ray Crystal Structure of Two New Mixed-valence Copper Cyanide Complexes: Unusual Bi-co-ordinated Copper(I) Atoms in Polymeric Networks. *J. C. S. Chem. Comm.* **1980**, 1116-1118.
6. Sherwood, P.; Hoffmann, R., Deformation in Mixed-Valent Cu(I)-Cu(II) Polymers. *Inorg. Chem.* **1989**, 28, 509-518.
7. Lu, J. Y.; Runnels, K. A., An unprecedented mixed-valent-copper mutual-face-insertion layered metal-organic polymer displaying graphite-like properties. *Inorg. Chem. Commun.* **2001**, 4, (11), 678-681.
8. Kumar, D. K.; Das, A.; Dastidar, P., Exploring conformationally flexible hydrogen-bond-functionalized ligand and counter anions in metal-organic frameworks of Cu(II). *New J. Chem.* **2006**, 30, (9), 1267-1274.
9. Hu, H. L.; Suen, M. C.; Yeh, C. W.; Chen, J. D., Synthesis and structures of two new copper(II) coordination polymers with pyridyl ligands. *Polyhedron* **2005**, 24, (12), 1497-1502.
10. Shin, Y. W.; Kim, T. H.; Seo, J.; Lee, S. S.; Kim, J., Anion-Controlled Copper(II) Coordination Polymers Based on Angular Dipyridyl Ligand. *Bull. Korean Chem. Soc.* **2006**, 27, (11), 1915-1918.

## Chapter 4

11. *SADABS*, Bruker Analytical X-ray: 1997.
12. Sheldrick, G. M. *SHELXS-97: Program for Structure Solution*, University of Gottingen, Germany: 1997.
13. Barbour, L. *X-Seed: Graphical Interface for SHELXL*, University of Missouri-Columbia: 2001.
14. Yasui, M.; Ishikawa, Y.; Akiyama, N.; Ishida, T.; Nogami, T.; Iwasaki, F., Dipyrimidine-copper(II) dinitrate complexes showing magnetic interactions. *Acta Cryst. B-Struct. Sci.* **2001**, 57, 288-295.
15. Shriver, D. F.; Atkins, P. W., *Inorganic chemistry*. 3rd ed.; Oxford University Press: New York, 1999.

## **Chapter 5**

### **Conclusion**

The synthesis, characterization, and potential applications of single-walled carbon nanotube gels and foam and copper-based coordination polymers were studied. A wide range of techniques were employed, including electron microscopy, IR spectroscopy, viscometry, thermal analysis, and X-ray diffraction. The studied materials have potential applications ranging from gas sorption and composite materials to ion exchange and catalysis.

## VITA

Karen A. Kirby was born on June 21, 1979, in Maryville, Missouri. After graduating from Maryville High School in 1997, she received a B.S. in Chemistry from the University of Minnesota (2001) and a Ph.D. in Chemistry from the University of Missouri-Columbia (2007) with emphasis in inorganic chemistry and materials. She has accepted a postdoctoral position in the Department of Molecular Microbiology and Immunology at the University of Missouri-Columbia with Dr. Stefan Sarafianos and Dr. Donald Burke using protein crystallography to study the structures of potential HIV inhibitors. She plans to pursue a career in X-ray crystallography.